UNIVERSIDAD COMPLUTENSE DE MADRID

FACULTAD DE CIENCIAS FÍSICAS

Departamento de Física de la Tierra, Astronomía y Astrofísica II
(Astrofísica y Ciencias de la Atmósfera)

TESIS DOCTORAL

Discrimination of ultra high energy cosmic rays with the Extreme Universe Space Observatory (EUSO)

Discriminación de rayos cósmicos de ultra alta energía con el Observatorio Espacial de Universo Extremo (EUSO)

MEMORIA PARA OPTAR AL GRADO DE DOCTOR

PRESENTADA POR

Guadalupe Sáez Cano

Directores

M.D. Rodríguez Frías
L. del Peral Cochicoa

Madrid, 2015

Universidad Complutense de Madrid
Facultad de CC. Físicas
Dpto. de Física de la Tierra, Astronomía y Astrofísica II
(Astrofísica y cc. de la Atmósfera)

Tesis Doctoral

Discrimination of Ultra High Energy Cosmic Rays with the Extreme Universe Space Observatory (EUSO)

Discriminación de Rayos Cósmicos de Ultra Alta Energía con el Observatorio Espacial de Universo Extremo (EUSO)

Dirigida por los doctores:

M. D. Rodríguez Frías y L. del Peral Gochicoa

Guadalupe Sáez Cano

Madrid, febrero de 2015

A mi madre

"So close, no matter how far"

Agradecimientos

En primer lugar quiero agradecer a mi familia el apoyo recibido durante mis no muy fáciles años de tesis. A mi madre, que siempre ha estado a mi lado en cada paso del camino. Aún nos queda mucho por caminar juntas, aunque sea en la distancia. Esta tesis ha sido posible gracias a ti. A mi padre, que me inculcó la curiosidad desde pequeña por la ciencia con su ya famosa frase: "La Física Cuántica explica por qué, si ahora mismo te das un trillón de cabezazos contra la pared, tienes una posibilidad de atravesarla". A mi hermana, por creer que mi vida profesional es muy útil en nuestro día a día (aunque sea para ver juntas "Big Bang Theory"). A mis abuelos, que piensan que lo que hago es importantísimo, aunque no sepan a qué me dedico. Y al resto de mi familia por estar siempre ahí.

A mis directores de tesis María Dolores Rodríguez Frías y Luis del Peral, por haberme dado la oportunidad de trabajar en un proyecto tan innovador y de ámbito tan internacional, en el que he conocido a gente estupenda. Gracias por haberme guiado durante la tesis, siempre buscando lo mejor para mi. A mis compañeros de fatigas diarias: a Germán por sus clases de ROOT, a Jose por ser mi profe de C++, a Héctor por alegrarnos a todos con sus carcajadas infinitas, a Jorge, por leerse mi tesis con tanto interés, y a mi estilista particular, Álvaro. To Kenji, for being such a good teacher and friend from the very beginning. To "my German team": Thomas, Alejandro, Francesco and company. To Professor Santangelo for his hospitality, hosting me in Tüebingen for so long. To the "Alternative Executive Commitee" (Simona et al.) for making the meetings so funny and lovely. And to all the JEM-EUSO members for being such a warm and nice Collaboration. Al Ministerio de Economía y Competitividad y al Ministerio de Ciencia e Innovación por

financiar este trabajo.

A mis amigos de siempre: a Luis por confiar en que todo lo que hago saldrá bien, a Gonchi por saber animarme en los malos momentos, a Inés por estar siempre dispuesta a venir a casa a echar una mano, a Chus por interesarse por mi trabajo, a "José Antonio" por ser mi médico particular, a Pepe por estar cada fin de semana donde siempre, a Berme por animarnos con sus historias de viajes y aventuras, a Jaime por tener siempre una sonrisa para todos, y al resto de "los de toda la vida".

A mis físicos: a María por las horas en la biblioteca y nuestros locos descansos, a Sara por nuestro año Erasmus y todas nuestras vivencias, a Andrea por hacer de los laboratorios una experiencia única, a Meri porque desde el primer día de facultad sigue a mi lado, a Eva por nuestras horas de spinning para relajarnos, a Rocío por las memorables fiestas en su casa, a Mariajo porque sus despistes hacen que los de los demás no parezcan tan importantes, a Andrés por presentarme al niño de mis ojos, y a los demás de la panda por hacer de la universidad una época para recordar siempre.

A mis amigas de Pradoluengo: Cris, Sara, María, Lidi, Lauri, Danae, Gloria y Marta, por demostrarme que hay dos tipos de familia; la que se hereda y la que se hace a lo largo del camino.

A los de Alcalá, por enseñarme que durante los años de tesis se aprende mucho además de física: a Cris, Noe, Sara, Uge, Belén, Judit, Antoñito y demás EcoGeoFísicos (sois demasiados para nombraros a todos). ¡Qué hubiera sido de mi sin las graciosísimas horas de la comida!

Y finalmente, a Álex, por su cariño y paciencia infinitos. Gracias por estar a mi lado.

Contents

List of Figures

List of Tables

Chapter 1

Introduction

Cosmic rays were discovered in 1912 by Victor Hess. He detected ionizing radiation hitting the atmosphere. During balloon flights, this radiation was discovered to increase with the altitude, indicating that it must come from outside the Earth [1]. During the 1930's it was found out that cosmic rays were charged particles. The Earth's magnetic field acts on energetic particles according to their charge. Observing this fact, it is how it was proved that they are charged particles. These particles cover a wide range of energies. Even though most energetic events are more difficult to observe, from 1960 to nowadays about two dozens of events with energies of 10^{20} eV have been discovered.

However, although one century has gone by, it is still unknown where these particles come from. Also their acceleration mechanisms are a mystery. Cosmic ray direct observation is a very hard task. But cosmic rays produce Extensive Air Showers (EAS). These are cascades of particles created by primary particles when they reach the Earth's atmosphere and interact with its particles. Therefore, properties of cosmic rays can be studied by observing properties of the EAS produced in our atmosphere [2]. EAS observation can be done considering two main components: fluorescence light and Cherenkov light. Most of secondary particles produced in EAS are electrons. These electrons excite nitrogen molecules in the atmosphere that results in fluorescence light through the de-excitation of the molecules. On the other hand, a Cherenkov component is produced, due to the relativistic speed of the particles. These components can be measured by ultraviolet (UV)

telescopes.

Some experiments meant to detect Ultra High Energy Cosmic Rays (UHECRs) are HiRes, AGASA, Pierre Auger Observatory and JEM-EUSO. High Resolution Fly's Eye or HiRes detector operated in Utah desert from 1997 until 2006. HiRes utilized the atmospheric fluorescence technique. AGASA experiment collected data from 1990 to 2004 at the Akeno Observatory. The Pierre Auger Observatory, on the other hand, is the first hybrid experiment. It takes advantage of the two methods, consisting of fluorescence telescopes and an array of water Cherenkov tanks. Also, the area covered by Auger is the largest one ever covered by any of these experiments. This allow to have enough statistics to study UHECRs above 10^{18} eV.

Since cosmic rays energy spectrum decreases as $E^{-2.7}$, UHECRs flux at the highest energies (above $\sim 5 \times 10^{19}$ eV) is such small that, to measure them, a larger collected area is needed. To study EECRs (Extreme Energy Cosmic Rays), whose energies are even higher than those detected by Auger, the collected area of the experiment must be so large that they cannot be investigated by ground-based experiments. JEM-EUSO (Extreme Universe Space Observatory on Japanese Experiment Module) is a new type, space-based experiment that will be launched in 2019 [3]. It will observe EAS produced by UHECRs and EECRs within a range of energies from $10^{19.5}$ eV to 10^{21} eV.

JEM-EUSO will use the atmosphere as a detector. Thus, information about properties of the Earth's atmosphere and presence of different type of clouds is highly needed. JEM-EUSO includes an Atmospheric Monitoring System (AMS) to provide information on the distribution and optical properties of the cloud and aerosol layers within the telescope Field of View (FoV) [4]. The AMS will consist of an Infrared camera, responsability of the Spanish Consortium in JEM-EUSO, and a LIght Detection And Ranging device (LIDAR) [5].

In this work it has been studied how different clouds might affect the signal produced by UHECRs and detected by JEM-EUSO. This effect depends not only on the optical depth and on the altitude of the cloud, but also on some properties of the EAS (such as the arrival direction or the primary energy). We have investigated how the EAS signal

looks like depending on the part of the Field of View where it is detected, the trigger efficiency under cloudy conditions ("cloud efficiency"), the shower geometry in presence of clouds, as well as the primary particle energy and shower maximum reconstruction [6]. Also, a three dimensional photon propagation module has been developed to include a more complete model of the atmosphere for the EAS study.

Chapter 2

The most energetic cosmic rays

Ultra High Energy Cosmic Rays (UHECRs) and Extremely High Energy Cosmic Rays (EHECRs) are the most energetic particles all over the Universe. They cover from 10^{17}eV to more than 10^{20}eV [2]. Due to these extremely high energies, they are not significantly affected by galactic or extragalactic magnetic fields. Therefore, tracing back their trajectories, possible sources of UHECRs and EHECRs might be identified. For simplicity, in this thesis we will use UHECRs for refering to both of them.

Properties of primary particles with energies higher than 10^{14} eV cannot be measured directly. However, they can be measured by the observation of the cascades of secondary particles produced when cosmic rays (CRs) come through the atmosphere. These cascades are named Extensive Air Showers (EAS). The energy of the cosmic ray is shared among EAS particles, that are mostly electrons and positrons ($\sim$ 90%). When these electrons and positrons interact with nitrogen molecules of the atmosphere, fluorescence light is produced (by nitrogen excitation and de-excitation processes). Also, a Cherenkov component results due to the relativistic speed of the particles [1].

Due to the fact that the flux of cosmic rays at the highest energies is extremely small, a very large collected area is needed. There is no ground-based telescope capable to achieve this huge area. Therefore, we need a space-based experiment to investigate their origin. JEM-EUSO is an experiment that will be launched in 2019 and located onboard the Japanese Module of the International Space Station (ISS), which is at an altitude of

400 km. With a field of view of 60°, it will correspond to a huge collected area. Its aim is to identify origin sources by detecting UHECRs at large statistics. It will use the Earth's atmosphere as a detector (see Chapter 3).

Cosmic rays were discovered in 1912 by Victor Hess. By doing some experiments during balloon flights, he realized that ionizing radiation hitting the atmosphere increased with altitude. Thus, he concluded that the radiation came from outside the Earth. This radiation was named *Cosmic Rays*. In 1926 and 1927, J. Clay measured cosmic rays intensity as a function of latitude during his sea voyages between Europe and Indonesia [7]. It found out that Earth's magnetic field affected cosmic rays, and therefore the latter were charged particles. Skobeltsyn made cloud-chamber photographs that showed cosmic rays as charged particles, confirming Clay's evidence. In 1938, Pierre Auger and his colleagues noticed that two detectors located many meters apart signaled the arrival of particles at exactly the same time. They correctly interpreted this result proving the existence of EAS generated by a single particle, the cosmic ray, entering in the atmosphere [8]. They were able to estimate the energy of the primary particle: 10^{15} eV. Thus, it was known that the cosmic rays energy spectrum extended beyond GeV. In 1941 Marcel Schein and others conducted balloon flights and demonstrated that cosmic rays spectrum was proton-dominated [9]. However, at energies near 10^{18} eV, there is observational evidence that a small fraction of the particles are neutrons; these events correlate on the sky with the regions of highest expected cosmic ray interactions, the Cygnus region and the Galactic center region [10]. In 1949 Fermi postulated the Fermi's cosmic ray "shock" accelerator, where protons speed up by magnetic clouds. It was believed that supernovae act as such cosmic accelerators, but they alone cannot account for the highest energy cosmic rays. In 1966, Greisen, Kuzmin and Zatsepin theorized that high energy cosmic rays would interact with the Cosmic Microwave Background (CMB), and this interaction would reduce their energy, so that particles traveling long intergalactic distances could not have energies greater than 5×10^{19} eV [11]. In 1991 Fly's eye researchers observed an event of 3×10^{20} eV. In 1994 the AGASA group detected an event of 2×10^{20} eV. From around 1960 about two dozens of events at energies of 10^{20} eV have been detected [12].

However, although one century has gone by since the cosmic rays discovery, there are some questions that still remain unsolved. JEM-EUSO will investigate some of them, such as which the origin of Ultra High Energy Cosmic Rays is and which mechanism can accelerate them to such high energies.

2.1 Origin and composition

At low energies, the chemical composition for cosmic rays is rather close to that of the interstellar medium. This leads to the assumption that, at this energies, cosmic rays consists of stellar matter [13]. However, there are a few pecularities (as shown in Figure 2.1):

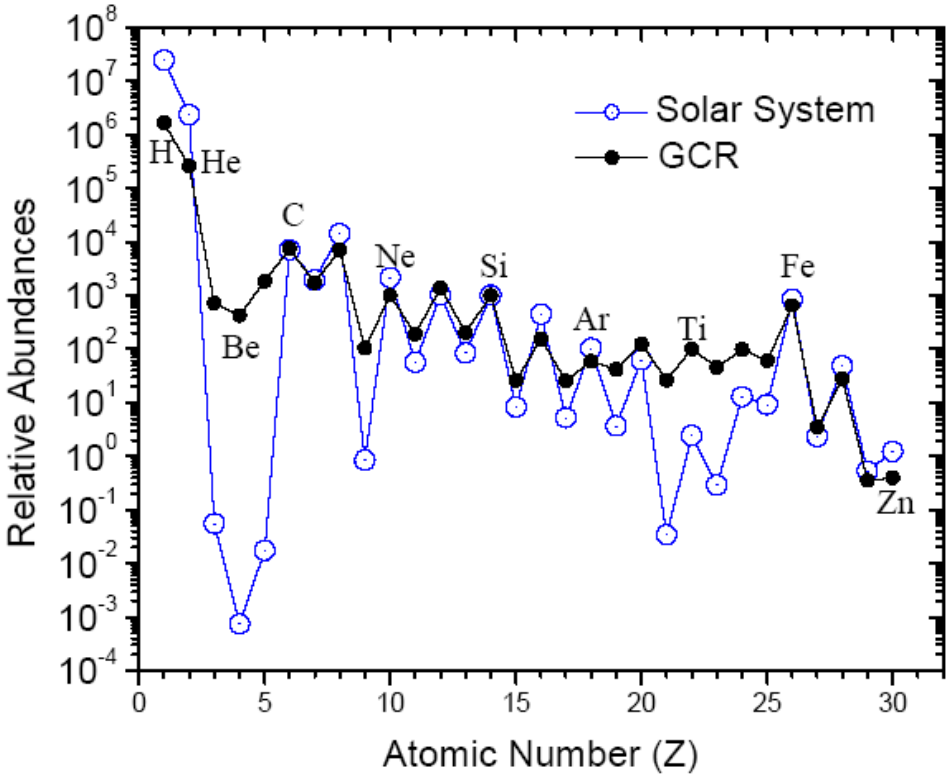

Figure 2.1: Chemical composition of low energy (E <2 Gev/nucleon) cosmic radiation compared to the composition of the solar system normalized to 100 at Si [14].

- the elements hydrogen and helium seem to be less abundant in the cosmic radiation.
- Litium, berilium and boron are more abundant in the cosmic radiation by orders of magnitude.
- Scandium and vanadium are more abundant in the cosmic radiation.

The latter two features can be explained because these elements are not produced by the stellar nucleo-synthesis, but they emerge from collisions of carbon, oxygen and iron nuclei with the interstellar matter. In overall, 90% are protons, 9% are alpha particles and the rest are heavier nuclei [1]. Concerning the energy dependence, the fraction of heavy elements increases, with moderately to heavy elements dominating beyond the knee, all the way to the ankle, where the composition seems to become light again.

The mass composition of the highest energy cosmic rays remains uncertain. HiRes data favor the proton composition at energies from 10^{18} eV to 5 $\times 10^{19}$ eV , whereas the Auger data indicate that the cosmic ray composition is becoming heavier with energy, changing from predominantly proton at 10^{18} eV to heavier composition at about 5×10^{19} eV. However, the mass composition interpretation depends on the assumed hadronic model, which is extrapolated from lower energy physics [15].

At energies above 10^{18} eV the Larmor radius of a proton in a magnetic field of 1 μG (the average magnetic field in our Galaxy) is around 1 kpc, comparable to the size of the Galaxy. Therefore, the bulk of the cosmic rays of energies lower than 10^{18} eV are considered of galactic origin.

Models to explain the acceleration of UHECRs to such high energies can be divided in two groups: bottom-up models (which consider the UHECRs to be accelerated by astrophysical objects), and top-down models (which propose more exotic models).

2.1.1 Bottom-up models

First and second-order Fermi processes (see Section 2.2) occur in astrophysical objects such as Supernova Remnants, Active Galactic Nuclei, Neutron stars or Gamma Ray

Bursts, and would force a power-law spectrum. The list of potential sources which could give the observed flux of the highest energy cosmic rays includes AGNs, Gamma Ray Bursts, Supernova Remnants, pulsars, interacting galaxies, or other objects [15], as can be seen in Figure 2.2.

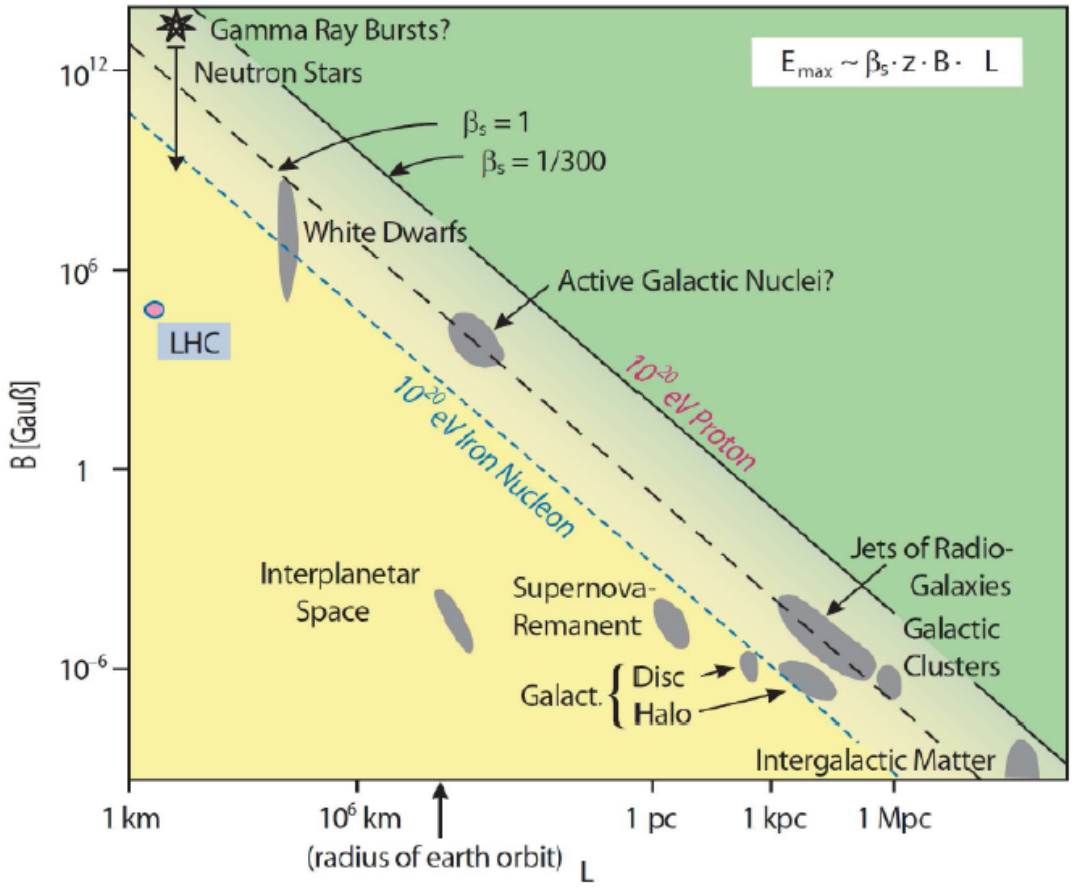

Figure 2.2: Hillas Diagram: theoretical upper limits of the energy of the particle are determined by the size and strength of celestial objects [16].

Supernova Remnants

Supernova Remnants (SNRs) are believed to accelerate galactic cosmic rays up to at least the energy of the knee ($E \lesssim 3 \times 10^{15}$ eV) via diffusive shock acceleration. Numerous SNRs have been detected in GeV and TeV gamma rays. There are some possible explanations:

- these processes may be explained by leptonic processes.

- Gamma rays can also be produced by CRs after they escape from SNRs due to hadronic interactions in the ambient gas.

Thus, the detection of gamma ray emission from the vicinities of SNRs might provide an indirect evidence for the fact that the nearby SNR is accelerating CRs. Unfortunately, the way in which CRs escape SNRs is little understood. Qualitatively, CRs with the highest energies are expected to escape first, while CRs of lower energy are expected to escape progressively later in time, as the shock slows down [17].

The origin is still unclear, since there are possible evidences for the two explanations. For instance, the emission from the SNR RX J1713.7-3946 seems to be leptonic, though the one from Tycho seems hadronic.

Active Galactic Nuclei

Active Galactic Nuclei (AGN) are one of the most popular objects for CRs origin, since a strong correlation was claimed by Pierre Auger Observatory. AGN are assumed to have a gaussian flux distribution with a certain angular width [18]. However, its updated analysis results and other studies exclude the hypothesis that the whole set of AGN is responsible for the UHECRs [19].

Pulsars

Pulsars have a strong rotating magnetic field which results in a large electromotive force. This can trap a particle while accelerating it to high energies. However, there are some problems with this model. For example, the power law spectrum observed in cosmic rays is not immediately obvious in this scenario and the acceleration occurs in a dense region of space where chances for energy loss are high due to meson photo-production, photo-nuclear fission and pair creation. These affect the energy spectrum and the composition of the resulting cosmic rays which are not in agreement with experimental data [20].

Gamma Ray Burst

The origin of the detected Gamma Ray Bursts (GRBs) can be explained by the collapse of massive stars or mergers of black holes or neutron stars. A relativistic shock is caused by a relativistic fireball in a pre-existing gas, such as a stellar wind, producing or accelerating electrons/positrons to very high energies. The observed gamma-rays are emitted by relativistic electrons via synchrotron radiation and inverse Compton scattering. The detected GRBs release energy up to 10^{51} erg/s which would account for the luminosity required for cosmic rays above 10^{19} eV if the GRBs are uniformly distributed (independently of redshift). However, recent studies indicate that their redshift distribution seems to follow the average star formation rate of the Universe and that GRBs are more numerous at high redshifts. In addition, no correlation between Auger data and GRBs has been reported recently [21].

2.1.2 Top-down models

Although several astrophysical systems can be UHECR sources, the acceleration to energies up to $\sim 10^{20}$eV is an unlikely process that requires very efficient acceleration scenarios. The top-down models do not involve any acceleration mechanism by astrophysical sources. They state that cosmic particles are the decay products of very massive particles with rest mass of $\sim 10^{25}$ eV. Two scenarios are mainly proposed [22]:

- UHECRs come from the decay and annihilation of Super-Heavy Dark Matter particles, which are remnants of the early Universe.

- The called topological Defect models, suggest that unknown X particles are emitted by topological defects formed in the early stages of the Universe, such as magnetic monopoles, cosmic strings and necklaces.

2.2 Propagation and acceleration mechanisms

To perform UHECRs astronomy, the original particle direction during its travel from the source to the Earth should be conserved. Unfortunately, charged cosmic rays are deflected by the galactic and extragalactic magnetic fields. However, for higher energies of the cosmic ray, we have lower deflections. For protons at $\sim 10^{20}$ eV, their deviation is less than 1° [23].

Three mechanisms contribute to the energy losses of ultra high energy protons: the photo-pion production (responsible for the GZK effect), the Pair Production by Proton (PPP) and the expanding universe redshift [24]. The photo-pion production affects protons with energies above 50 EeV. If UHECRs are extragalactic in origin, the interactions of UHECRs with the CMB photons (pair creation and pion production) give significant modifications in the energy spectrum observed on the Earth. In this case, a cutoff appears in the spectrum as an upper bound of cosmic ray energies. As UHECR propagate through intergalactic space, neutrinos and gamma rays are produced as secondary particles by photo-pion production [25] (see section 2.3).

Particle acceleration can occur basically in two ways: though direct acceleration by an electric field, or by stochastic acceleration in a magnetized plasma such as interstellar clouds [26].

Second-order acceleration proposed by Enrico Fermi explains the acceleration of relativistic particles by means of their collision with interstellar clouds. During these encounters, particles can either gain or lose energy. The average gain process is positive, although it is produced in a slow way. Moreover, energy losses are significant and mainly caused by ionization. It can be shown that the average energy gain per collision is:

$$\left\langle \frac{\Delta E}{E} \right\rangle = \frac{8}{3} \cdot \left(\frac{v}{c}\right)^2 \tag{2.1}$$

where v is the speed of the cloud, and c is the speed of light. Even though second-order acceleration succeeds in generating a power-law spectrum, it is not a completely satisfactory mechanism. First, on account of the observed low cloud density, the energy

gain is very slow. Second, the mechanism fails to explain the observed value of 2.7 for the exponent in the power-law spectrum [27].

The first-order acceleration mechanism obtains an energy gain that is linear in (v/c), a condition that would make the acceleration process more effective, especially at high v. This energy gain is described by:

$$\left\langle \frac{\Delta E}{E} \right\rangle = \frac{4}{3} \cdot \left(\frac{v}{c}\right) \tag{2.2}$$

This mechanism would occur when the relativistic particles collide with strong shock waves (such as those produced in supernova explosions, active galactic nuclei, etc). The particle Larmor radius, ($r_L \simeq E/QB$, where E is the particle energy, Q is its charge, and B is the magnetic field in the acceleration zone) must be smaller than the size scale of the acceleration region [12].

Although for the energy spectrum with this mechanisms the observed exponent of 2.7 is not obtained, the first-order mechanism is up to now the most effective, since shock waves are expected to be present in different astrophysical enviroments [27].

2.3 Energy spectrum: GZK suppression and trans-GZK events

The cosmic ray energy spectrum is the representation of the number of particles at a certain energy E within a certain small energy interval dE. Over 12 orders of magnitud in energy (from 1 GeV to more than 10^{20} eV) and 30 in flux (from 1 particle $\mathrm{m^{-2}s^{-1}sr^{-1}}$ to less than 1 particle $\mathrm{km^{-2}century^{-1}sr^{-1}}$), the spectrum can be well described by an almost constant power-law $\frac{dN(E)}{dE} \propto E^{-\alpha}$, with few features: one at about $4{\times}10^{15}$ eV (knee), another at $5{\times}10^{17}$ eV (second knee) and the other at about $\times 10^{18}$ eV (ankle) [28, 29]. The knee could reflect the fact that most cosmic accelerators in the galaxy have reached their maximum energy. For instance, it is estimated that some types of expanding supernova remnants, are not able to accelerate protons above energies in the range of 10^{15} eV. In the knee, the coefficient α rises from 2.7 to about 3.1. With KASKADE detector it

was found out that the knee occurred earlier for protons and helium and later for heavier nuclei [30]. In the region of the second knee it is assumed a transition to heavy primaries [10]. The ankle is traditionally explained in terms of transition from galactic to extra galactic cosmic rays, coupled with $e^+ - e^-$ energy losses of extragalactic protons on the 2.7 K CMB.

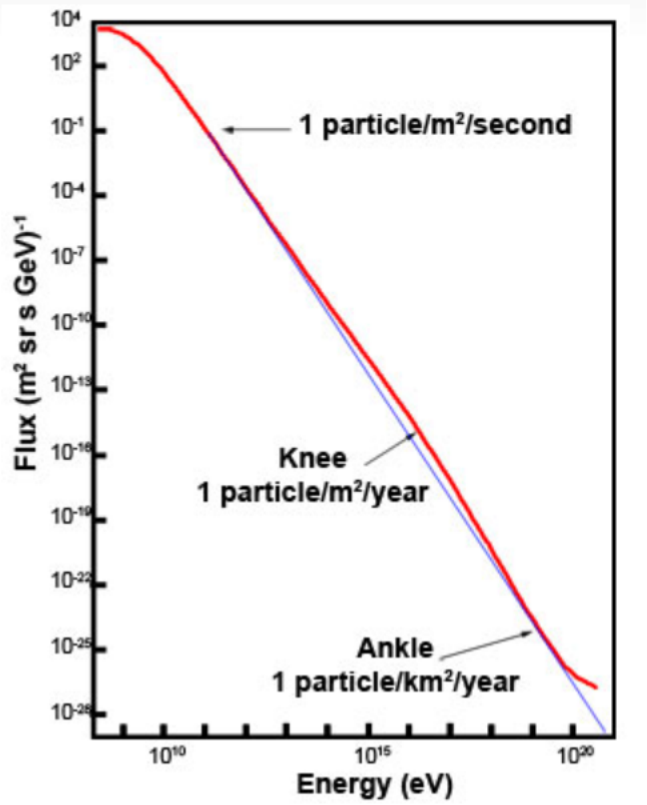

Figure 2.3: The cosmic ray spectrum clearly shows that the number of cosmic rays (the cosmic ray flux) detected drops off dramatically as we go to higher energies. The spectrum exhibits a knee and an ankle, both of which deviate from the standard exponential decline (blue line) [31].

The GZK suppression describes the sharp steepening of the spectrum at highest energies. In 1966, Greisen, and Zatsepin and Kuzmin, proposed an upper limit to the cosmic-ray energy spectrum at about 5 $\times 10^{19}$ eV [32]. They predicted that a proton dominated extra-galactic cosmic-ray flux would interact with the photons in the cosmic

microwave background (CMB), losing energy by pion photo-production [33]:

$$p + \gamma_{CMB} \rightarrow p + \Pi^0$$
$$p + \gamma_{CMB} \rightarrow n + \Pi^+$$

Nevertheless, this suppression does not mean that no cosmic rays above 5 $\times 10^{19}$ eV exist. In fact, some events above GZK suppression have been already detected by experiments such as AGASA and HiRes.

2.4 Extensive Air Showers

In 1938, Pierre Auger discovered the EAS, which are cascades of secondary particles initiated by the interaction of very high energy cosmic rays with the Earth's atmosphere. The measurement of EAS turned out to be the only method for the detection of cosmic rays with energies higher than 10^{14} eV [13].

The shower induced has three components that will be explained below: electromagnetic cascade, muonic cascade and hadronic cascade. If the primary particle is a nucleon or a nucleus, the shower begins with a hadronic interaction. The number of hadrons increases through subsequent generations of particle interactions. However, in each generation about 30% of the energy is transferred to an electromagnetic cascade by the prompt decay of neutral pions. Ultimately, the electromagnetic cascade dissipates around 90% of the primary particles energy, and hence the total number of electromagnetic particles is very nearly proportional to the shower energy. The remaining energy is carried by muons and neutrinos from $\pi^{\pm}$ decays [1].

A detailed understanding of how an air shower develops is crucial to obtain an estimate of the primary energy and to learn anything about the mass spectrum of the primary particles. Also, from the earliest years of discovery of cosmic rays there have been searches for directional anisotropies to have a hint of their origin [34]. As the cascade develops in the atmosphere, the number of particles in the shower increases until the energy of the secondary particles is degraded to the level where ionization losses become dominant.

This energy is named critical energy (E_c). At this point the density of particles starts to decline. The number of particles as a function of the amount of atmosphere penetrated by the cascade (in g/cm^2) is known as the longitudinal profile. The atmospheric depth at which the number of particles in the shower reaches its maximum, X_{max}, is one of the most useful observables of the shower, due to its dependence on the primary energy and composition. How the average of the shower maximum $\langle X_{max} \rangle$ changes with energy depends on the primary particle. Each EAS produces mainly two light components that are fluorescence and Cherenkov light:

- Fluorescence light is produced when secondary particles (mainly electrons) interact with molecules of the atmosphere (mainly nitrogen) and excite them. When these molecules de-excite, they produce what is called fluorescence light. The fluorescence detection method that has been developed does not suffer from the drawback of model dependence. Shower particles excite the 1+ and 2+ bands of nitrogen as they traverse the atmosphere. The major component of the resulting fluorescence is in the 300 - 400 nm range [35]. The resulting cascade profile gives the particle number as a function of depth and the energy of the primary can be obtained rather directly from the area under the curve. The energy of the particle that initiates each cascade is obtained by integrating under the cascade curve and multiplying the result by the ratio of the critical energy for an electron in air, about 84 MeV, to the radiation length, about 38 g/cm^2. A good understanding of attenuation effects of the intervening atmosphere is very important. The fluorescence yield of photons, as a function of wavelength in the studied wavelength range, must be known accurately so that corrections can be made for Rayleigh scattering [36].

- Due to their relativistic speeds, charged particles produce highly polarized optical Cherenkov light as they propagate through the atmosphere (or through any transparent medium such as water). This light propagates in a forward cone, very colimatelly to the shower development direction. The aperture of this cone depends on the refraction index of the medium and on the speed of the particle. This light is

produced because when the particle moves through the medium at a velocity higher than the speed of light in this medium, an electromagnetic shock wave is created. That shock wave radiates out from the particle, carrying off energy in many different wavelengths of electromagnetic radiation [37].

2.4.1 Longitudinal development: elongation rate

The longitudinal profile is the number of charged particles of a shower as a function of the atmospheric slant depth, and it is observed with fluorescence telescopes. This atmospheric slant depth at a given height z measured from the ground level, depends on the shower geometry and on the atmosphere density $\rho(z)$.

The general shape of the longitudinal profile grows up while the energy of the particles is high enough to produce more particles, it reaches a maximum and later decreases because the energy is low and the particles are absorbed mainly by ionization. The longitudinal profile may be adequately parametrized by the Gaisser-Hillas function, which has only four free parameters:

$$N_e(X) = N_{e,max} \left(\frac{X - X_0}{X_{max} - X_0} \right)^{\frac{(X_{max}-X_0)}{\lambda}} e^{\frac{(X_{max}-X)}{\lambda}} \tag{2.3}$$

where N_e is the number of particles, $N_{e,max}$ is the number of particles at the maximum, X_0 is the first interaction point, and λ the shower decay length. All the parameters except $N_{e,max}$ have dimensions of atmospheric depth (mass/surface).

Due to the fact that the relevant parameters of particle physics for cosmic rays are largely unknown, it has been dificult to deduce the mass composition from available experimental data. Nowadays, this problem is trying to be solved with the study of the variation of the shower maximum atmospheric depth with energy, named the "elongation rate", which relates the depth of maximum of an average shower to the shower's energy [38]. It is expressed as the derivative:

$$D_e = \frac{d(X_m)}{d(lnE)} \tag{2.4}$$

where X_m is averaged over fluctuations in shower development, and in the case of mixed primary composition, over the equal-energy mass spectrum. $\langle X_{max} \rangle$ and D_e can be determined directly from the longitudinal shower profile and E_0 (primary energy) and thus the composition can be extracted after estimating the energy from the total fluorescence yield. After the longitudinal development is fitted using the Gaisser-Hillas function, the energy of the electromagnetic cascade can be calculated by integrating the shower profile:

$$E_{em} = A_0 \int_0^{+\infty} N(X) dX \tag{2.5}$$

where A_0=2.2 Mev·cm^2/g is the mean energy deposited by one charged particle in the atmosphere per slant depth [39].

2.4.2 Lateral development: shower age

As the shower develops, it also spreads laterally (perpendicular to the shower axis), due to the Coulomb scattering. The lateral extension of the core depends on the mean free path, so that it is proportional to the inverse of the atmospheric density. The numerical results obtained by Kamata and Nishimura for the three dimensional cascade problem, including multiple scattering, has been approximated by the function Nishimura-Kamata-Greisen (NKG) [40]:

$$\rho(r) = \frac{N_e}{r_M^2} \times f\left(s, \frac{r}{r_M}\right) \tag{2.6}$$

where ρ(r) is the density of particles per unit surface at a distance r in a plane perpendicular to the shower axis, N_e is the total number of particles, r_M is the Molière radius and s is the shower age parameter given by:

$$s = \frac{3X}{(X + 2X_{max})} \tag{2.7}$$

For shower age between 0.5 and 1.5 we can assume:

$$f\left(s, \frac{r}{r_M}\right) = \left(\frac{r}{r_M}\right)^{s-2} \left(1 + \frac{r}{r_M}\right)^{s-4.5} \left(\frac{\Gamma(4.5 - s)}{2\pi\Gamma(4.5 - 2s)}\right) \tag{2.8}$$

where Γ is the gamma function. The Molière radius can be written as:

$$r_M = 0.0265\chi_0(1.2 + Z) \tag{2.9}$$

where is χ_0 the radiation length and Z is the atomic number.

Approximatelly 90% of the energy is contained within a distance from the shower axis $d < r_M$. However, low energy photons and electrons, as well as muons, extend far away from core, constituting the halo which has a detectable density up to a few kilometers from the axis depending on the primary energy. The electromagnetic part of the halo increases with the depth, reaching its maximum at around $X_{max} + 100$ g/cm^2, decreasing abruptly and being completely extinguished at $X_{max} + 1000$ g/cm^2. Most muons travel beyond the electromagnetic cascade, giving a muonic tail [23].

Air shower development fluctuates in atmospheric depth due to fluctuations in the hadronic multiparticle production (which depends on the nature of the primary particle) and electromagnetic processes. As a consequence, the position of the shower maximum varies from event to event. One can express the shower longitudinal development as a function of the *shower age*, that is defined as (2.7), instead of as a function of the depth, X [35].

The shape of the spectrum at a given age s is the same independently of the nature of the primary particle (proton or iron) and its primary energy [41, 42].

2.4.3 Hadronic Component

The hadronic component is the backbone of the EAS. This part feeds the other shower components through the decay of secondary hadrons. The highest energetic hadron of the first interaction is called the leading hadron. The hadronic processes can be schematically summarized as [1]:

$$N_{CR} + N_{air} \rightarrow N_{CR'} + N_{air'} + \pi^{\pm} + \pi^0 + K^{\pm} + K^0 + \eta + p + n + \Lambda \tag{2.10}$$

where N_{CR} denotes the primary or the secondary particles of the cosmic radiation and N_{air} stands for a nucleus of the atmosphere. In a typical collision, more than 2/3 of the particles produced are pions, followed by about 10% kaons. Other hadrons, including neutrons and protons, are also produced. The hadronic component of extensive air showers

reveals important information about the mass and energy of the shower inducing primary particle [38].

The pions produced in the hadronic collisions are 2/3 charged and 1/3 neutral. A π^0 immediately decays to photons, initiating electromagnetic showers. Charged pions, on the other hand, produce more $\pi^{\pm}$. When the energy of the $\pi^{\pm}$ is lower than the E_c, this process ends, yielding muons. The high energy hadronic models are one of the most important source of unertainties in EAS analysis.

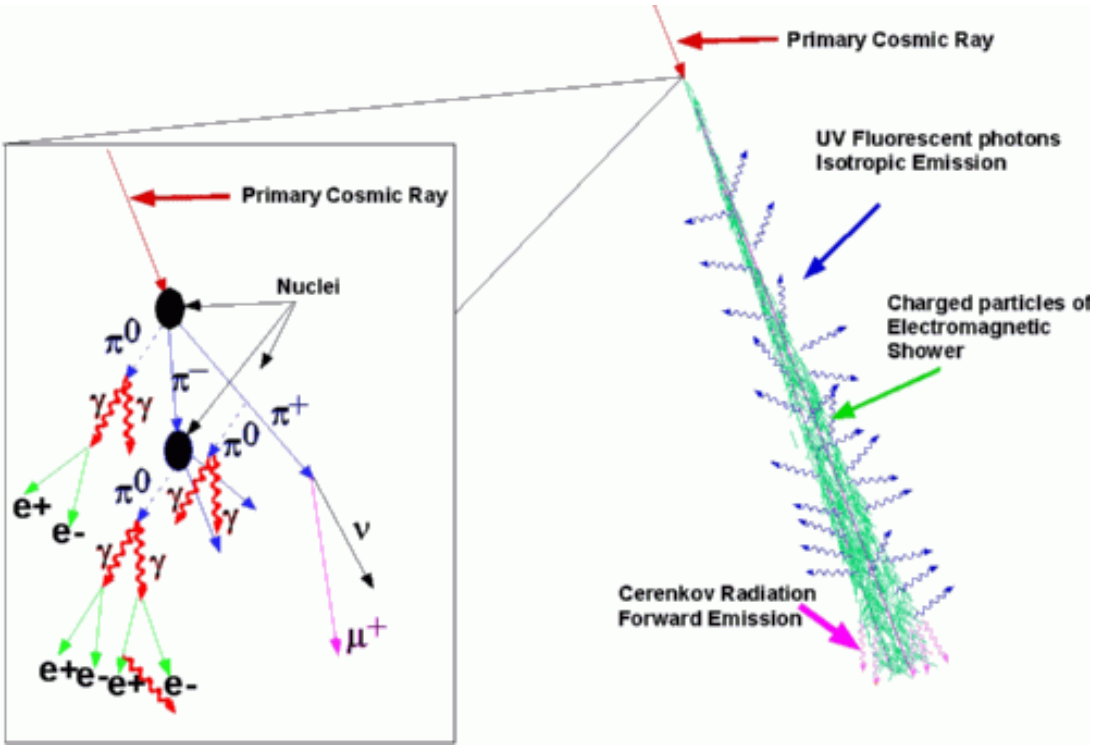

Figure 2.4: Representation of the different components in an extensive air shower [43].

Another small fraction which contributes to this component of the shower comes from the decay of two photons via two pion photo-production processes:

$$\gamma + \gamma \longrightarrow \pi^+ + \pi^- \tag{2.11}$$

2.4.4 Electromagnetic Cascade

A third of the pions produced in the hadronic collisions are π^0. These decay electromagnetically into two photons, giving 1/3 of the energy of the hadronic cascade to the electromagnetic component [13]:

$$\Pi^0 \rightarrow \gamma + \gamma \qquad (98.8\%)$$
$$\Pi^0 \rightarrow e^+ + e^- + \gamma \quad (1.2\%)$$

Neutral pions have a much shorter lifetime (10^{-16}s) than the $\pi^{\pm}$, and their decay is essentially instantaneous even with time dilation effect. Each photon produced by the π^0 decay initiates an electromagnetic cascade. The high energy processes that make up an electromagnetic cascade shower are pair production (2.12) and bremsstrahlung (2.13). The shower energy is dissipated by ionization of the medium by all the electrons and positrons in the cascade [1]. Because of the rapid multiplication of electromagnetic cascades, electrons and positrons are the most numerous particles in cosmic rays air showers. Thus, most of the shower energy is dissipated by ionization losses of the electrons and positrons.

$$\gamma \longrightarrow e^- + e^+ \tag{2.12}$$

$$e^{\pm} \longrightarrow e^{\pm} + \gamma \tag{2.13}$$

Heitler postulated a simple model for the electromagnetic component of the EAS. Every particle undergoes two-body splitting after it travels a "splitting distance", d, related to the radiation length, λ_r by the expression: $d = \lambda_r \ln 2$. After n splittings there are 2^n total particles in the shower. This process continues until the individual energies of $e^{\pm}$ become lower than the critic energy E_c [44]. This model accounts two important features: that the final total number of electrons, positrons, and photons N_{max} is proportional to the primary cosmic ray energy, and that the depth of maximum shower development is logarithmically proportional to this same energy. Thus, if we consider a shower initiated by a single photon with energy E_0, the cascade reaches its maximum size $N = N_{max}$ when all particles have energy E_c. Then, $E_0 \backsimeq N_{max} E_c$. It should be

considered that this model does not include attenuation of particle numbers, and thus, N_{max} measured by experiments can differ from the former one.

The atmospheric depth X_{max} at which the shower reaches its maximum size is obtained from the number n_c of splitting lengths required for the energy per particle to be reduced to E_c.

2.4.5 Muonic Component

Muons are mainly produced via the decay of charged pions, as expressed in (2.14), although charged kaons decay can also produce muons directly or by producing charged pions that decay into muons (such as (2.15)).

$$\pi^{\pm} \longrightarrow \mu^{\pm} + \upsilon_{\mu}(\overline{\upsilon}_{\mu}) \tag{2.14}$$

$$\begin{aligned} K^{\pm} &\longrightarrow K^{\pm} + \upsilon_{\mu}(\overline{\upsilon}_{\mu}) \\ K^{\pm} &\longrightarrow \mu^{\pm} + \pi^{0} \end{aligned} \tag{2.15}$$

The number of low energy muons increases as the shower develops, and then reaches a plateau because muons only lose energy relatively slowly by ionization of the medium [45]. Since muons decay times are long, they survive to reach the ground with a non-negligible energy loss (2 MeV $\cdot$ cm^2/g). However, they may decay in flight when their energy drops below 10 GeV, producing a second source of atmospheric neutrinos and e^+/e^-. Although the number of electrons in the shower is much greater than the number of muons, the fact that muons are much more penetrating than electrons means that they can be selectively detected by underground detectors. Therefore, the number of muons in extensive air showers is used as an estimator of the primary composition of UHECRs [46]. Moreover, muons are charged particles, so they are relativelly easy to detect [1]. Most of the muons are produced in a narrow depth interval corresponding to the shower maximum for their parents (mostly pions) [47].

Muons are produced with typical energies of few GeV, increasing with the altitude of production. Few of them can also be produced via the electromagnetic interactions of

photons:

$$\mu^{\pm} \longrightarrow e^{\pm} + \upsilon_{\mu}(\overline{\upsilon}_{\mu}) + \upsilon_{e}(\overline{\upsilon}_{e}) \tag{2.16}$$

Although muons are unstable particles, they decay after a lifetime of $2.2 \times 10^{-6} s$ into electrons or positrons, contributing to the electromagnetic component.

2.4.6 Atmospheric neutrinos

Atmospheric neutrinos are produced as decay products when a cosmic charged particle traverses the atmosphere and produce a hadronic shower. Electron-neutrinos (e-neutrinos) and muon-neutrinos (μ-neutrinos) results from the decay chain of charged pions to muons to electrons as shown in:

$$\begin{aligned} \pi^{+} &\longrightarrow \mu^{+} + \upsilon_{\mu} \\ &\downarrow \\ &e^{+} + \upsilon_{e} + \overline{\upsilon}_{\mu} \end{aligned} \tag{2.17}$$

$$\begin{aligned} \pi^{-} &\longrightarrow \mu^{-} + \overline{\upsilon}_{\mu} \\ &\downarrow \\ &e^{+} + \upsilon_{e} + \overline{\upsilon}_{\mu} \end{aligned} \tag{2.18}$$

Both reactions indicate that the flux of μ-neutrinos and e-neutrinos are related [48]. Moreover, one of the most sensitive methods to observe small neutrino masses is to study neutrino flavour oscillations. The flavour ratio is given by:

$$r = \frac{N_{\upsilon_{\mu}} + N_{\overline{\upsilon}_{\mu}}}{N_{\upsilon_{e}} + N_{\overline{\upsilon}_{e}}} \tag{2.19}$$

where N_i is the number of each neutrino type. This ratio increases with energy above a GeV because muons begin to reach the ground before they decay. If all the muons decay, the relation between the μ-neutrino flux with the e-neutrino flux is:

$$\Phi(\upsilon_{\mu} + \overline{\upsilon}_{\mu}) \backsimeq 2\Phi(\upsilon_{e} + \overline{\upsilon}_{e}) \tag{2.20}$$

Since in every π^+ and π^- decay chains produce a υ_μ and a $\overline{\upsilon}_\mu$, it can also be deduced that:

$$\Phi(\upsilon_\mu) \backsimeq \Phi(\overline{\upsilon}_\mu) \tag{2.21}$$

Since the primary cosmic ray flux decreases with the energy (approximately as $E^{-2.7}$), the calculated neutrino flux rapidly decreases with the increasing energy.

Atmospheric neutrinos are unique, because they travel very long distances of up to 12800 km, that is, the diameter of the Earth. Interactions of atmospheric neutrinos are most numerous in the GeV range. Therefore, they constitute the main background for nucleon decay. The experiments to detect them started in the 1960s. In all of them, neutrino events occurring in the rock surrounding a neutrino detector were measured. Since the experiments were carried out in extremely deep underground, the charged particles traversing the detectors almost horizontally were essentially of atmospheric neutrino origin [49].

The energy spectrum of high energy atmospheric μ-neutrinos has been measured in three experiments: Frejus (at energies up to 1 TeV), AMANDA-II (in energies from 1 to 100 TeV), and IceCube40 (in the range between 100 GeV and 400 TeV). Recently, the IceCube experiment presented results for the e-neutrino spectrum measured in the energy range of $\sim$ 80 GeV - 6 TeV. Thus, there will be a possibility to obtain the neutrino flavour ratio from IceCube experiment and to compare this one with predictions [50].

Chapter 3

The JEM-EUSO Space Mission

JEM-EUSO (the Extreme Universe Space Observatory on-board the Japanese Experiment Module) is an innovative space mission that will be launched in a few years. Looking down to the Earth from space, it utilizes the atmosphere as a detector of UHECR air showers with the aim of significantly increasing the exposure to UHECRs compared to the largest ground-based air shower arrays presently in operation [2]. The arrival direction map with some hundreds of events above $\sim 5 \times 10^{19}$ eV will provide us information on the origin of the UHECRs, probably allowing us to identify the nearest UHECR sources with known astrophysical objects. This will likely lead to an understanding of the acceleration mechanisms. It will also help to clarify the emission mechanisms, and also finally confirm the Greisen-Zatsepin-Kuzmin suppression [51].

3.1 State-of-the-art on UHECRs detection

3.1.1 Ground arrays: surface detectors

Detection of shower particles using arrays of detectors located on ground covering many square kilometers is the most common technique to detect UHECRs. The separation of the detectors is related to the scale of the shower footprint at the observation level. This is usually some hundred meters for UHECRs. Their average shower maximum is 750

g/cm^2, so commonly the detectors are located between the sea level and the corresponding altitude to 800 g/cm^2 [24]. The typical detectors used are plastic scintillators and water Cherenkov counters. At the ground level, one of the main indicators of the primary mass is the EAS muon content. Thus, surface arrays use muon separation capabilities, both direct (placing underground muon counters) or indirect (separating the detector signal due to muons) to achieve mass composition sensibility. It is also possible to study the primary mass using the timing of the EAS front: since muons suffer less scattering, they tend to arrive earlier than the electromagnetic component [29]. Some experiments using particle detectors are:

- AGASA: the AGASA experiment was an expansion of the Akeno ground array, located at the Akeno observatory in Japan. It consisted of 111 plastic scintillators, each one with an area of 2.2 m^2. The experiment had a resolution of 3° for 10^{19} eV EAS and 1.5° for 10^{20} eV showers [52]. Each surface detector was placed with a nearest-neighbour separation of about 1 km, covering a total area of $\sim$ 100 km^2. The detectors were sequentially connected with a pair of optical fibers. They were controlled and operated by a set of commands transmitted from a central computer. Also, AGASA had 27 detectors under absorbers to measure the muon component of the cascade [53].

- SUGAR: The SUGAR (Sydney University Giant Air-shower Recorder) array was located in the Pilliga State Forest, Australia, and was operating between 1968 and 1979. It had an extension of 70 km^2 and consisted of 47 independent stations with two buried liquid scintillator counters separated 50 m. Each station operated in an autonomous manner with solar power units and receiving their timing information via radio receivers [54].

3.1.2 Fluorescence telescopes

The fluorescence detector (FD) technique was first successfully used at the University of Utah in 1976 [55]. It consists of an array of ultraviolet telescopes. The common optics

are based on a primary mirror on a fixed mount.

The FDs measure the longitudinal development and the primary energy of air showers in the atmosphere analyzing the amount of light emitted by atmospheric molecules excited by charged particles in the showers. Some example of fluorescence telescopes are:

- the Fly's Eye experiment: Fly's Eye detector operated in the western Utah desert from 1997 until 2006. There were two detectors. Flys Eye I, consisting of 67 spherical mirrors of 1.5 m diameter, and Flys Eye II, consisting of 36 similar mirrors located 3.3 km away. Events were observed in monocular mode when a detector satisfied a minimum trigger requirement, and in stereo mode when two or more detectors triggered on the same event [56].

Figure 3.1: Two mirrors within the High Resolution Fly's Eye cosmic ray observatory [57].

- HiRes: High Resolution Fly's eye operated in Utah desert from 1997 until 2006,

although a prototype was operating between 1993 and 1996. It used larger mirrors and smaller pixels compared with the original Fly's Eye. It was composed of two observation sites separated by 12.6 km. Both together provided an azimuthal coverage of 360°. HiRes duty cycle was close to 10%.

3.1.3 Hybrid experiments

Hybrid experiments detect both Cherenkov and fluorescence components. Usually, fluorescence telescopes measure the longitudinal development of the EAS generated by a primary cosmic ray particle while scintillator detectors measure the lateral distribution of secondary particles that hit the ground [58]. Some hybrid experiments are:

- Auger: Auger is the first hybrid detector. It was built in Argentina. The construction was completed in 2008 although it is taking data since 2004. The Auger surface detector has a duty cycle of 100%. The Auger surface detector is an array of 1600 water Cherenkov tanks on a 3000 km^2 hexagonal grid. Tanks are separated 1.5 km. Each one has a total surface of $\sim$ 10 m^2, and it is filled with 12 tones of pure water. Cherenkov light produced by the passage of particles through the water is collected by three nine inch-diameter photomultiplier tubes (PMTs) that are symmetrically distributed at a distance of 1.20 m from the center of the tank and look downwards through windows of clear polyethylene into the water [59].

  The fluorescence detector (FD) comprises four observation sites (Los Leones, Los Morados, Loma Amarilla, and Coihueco), located on top of small elevations on the perimeter of the surface detector (SD) array. Six independent telescopes, each with field of view of 30°$\times$ 30° in azimuth and elevation, are located in each FD site. The telescopes face towards the interior of the array so that the combination of the six telescopes provides 180° coverage in azimuth [60].

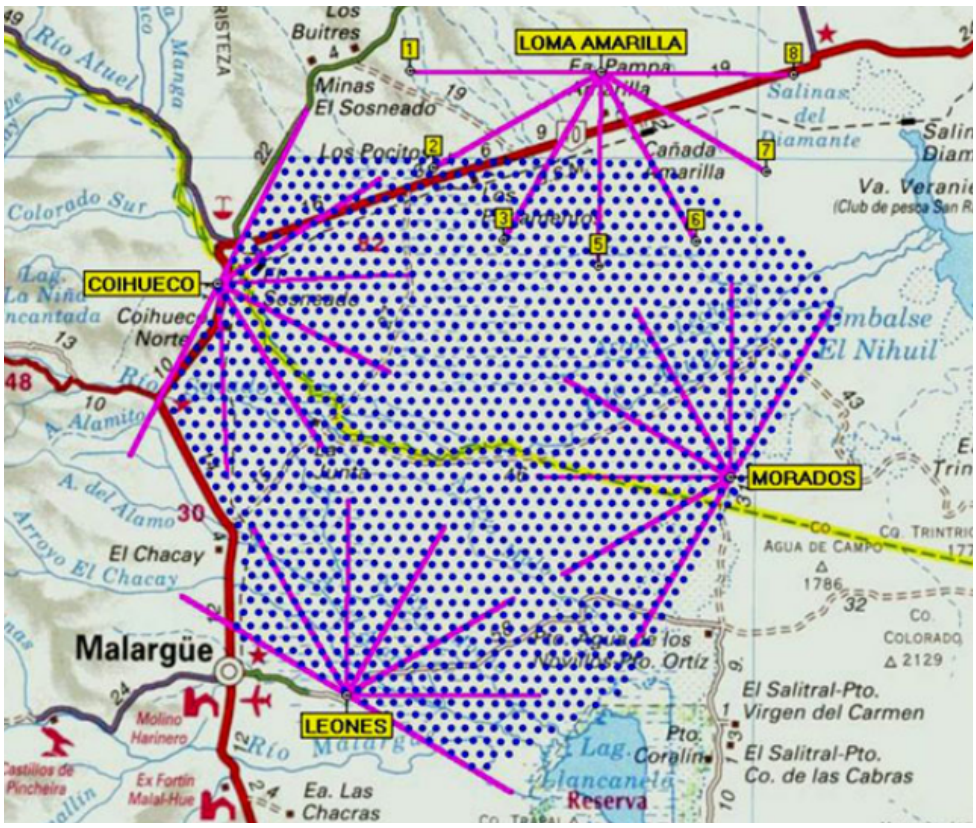

Figure 3.2: scheme of Auger telescope with the four fluorescence detectors and the surface detectors [61].

- Telescope Array (TA): TA is also an hybrid UHECRs detector and the largest one in the northern hemisphere. It is located in Utah, USA. It contains 507 surface detectors. The SD measure arrival timings and local densities of the shower particles at the ground. The arrival direction and primary energy of an air shower is determined from the relative timing differences of particle arrivals between SDs, and from the lateral distribution of local particle densities around the shower core. The SD array covers an area of about 700 km^2. Each detector has 3 m^2 of area. TA contains 38 fluorescence detectors. The TA FDs are installed in three stations (Black Rock Mesa, Long Ridge, and Middle Drum), which overlook the surface array. Each station contains 12 or 14 telescopes [62].

There is a rather large uncertainty in arrival directions of cosmic rays determined with FD in monocular mode, in which time differences between signals of the photo-tube pixels with small angular separations are used.

3.2 The Mission

As stated before, JEM-EUSO is a space-based mission meant to study UHECRs. JEM-EUSO focuses its science case on the most energetic events ($E \gtrsim 5 \times 10^{19}$eV), specially at energies around 10^{20}eV. JEM-EUSO will monitor the Earth's atmosphere to detect the UV (290-430 nm) tracks generated by EAS propagating through the atmosphere. By detecting the fluorescence and Cherenkov photons of the EAS, the energy, the arrival direction and the nature of the primary UHECR particle will be reconstructed [63].

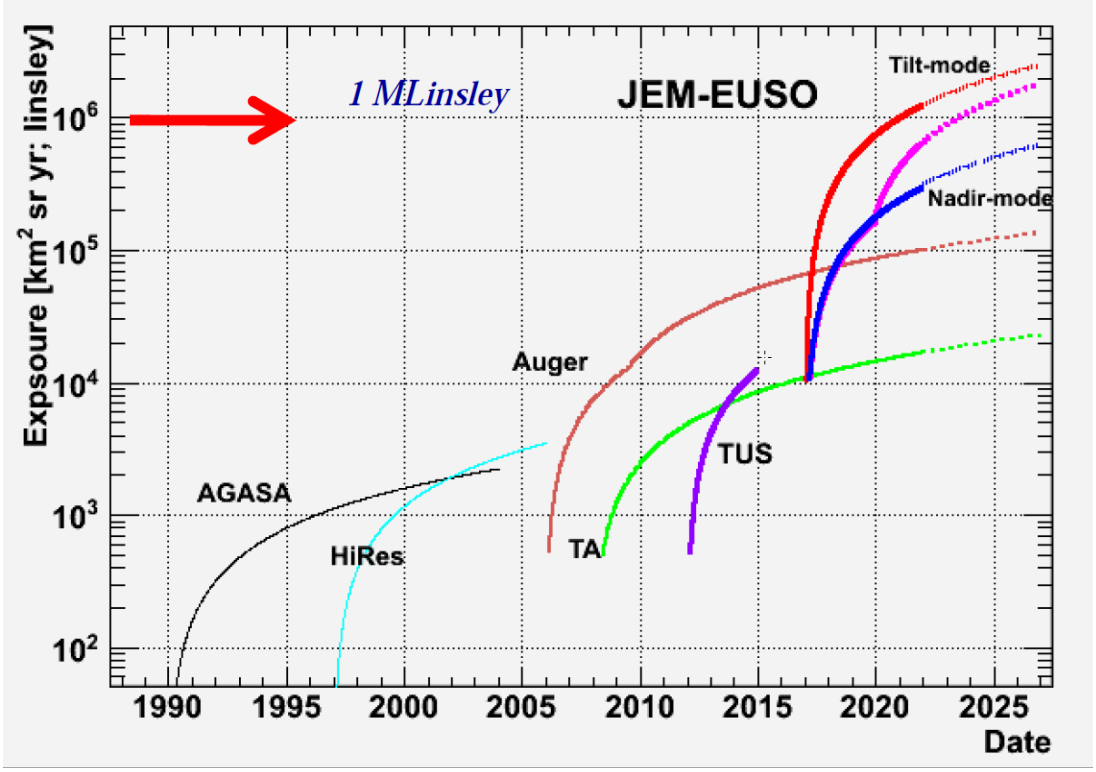

Figure 3.3: JEM-EUSO exposure in comparison with that of other experiments [63].

JEM-EUSO is the first space mission devoted to the exploration of the Universe through the detection of UHECRs and neutrinos [63]. In Figure 3.2, the expected exposure of JEM-EUSO is shown. The thick blue curve corresponds to the nadir mode of operation and the thick red curve, to the tilted mode [2]. For comparison, the evolution of exposure of other UHECR observatories is shown. It is noticeable that, observing from space (and therefore, with a larger observation area), a larger exposure is achievable.

The main scientific objective of the JEM-EUSO mission is to open the window for astronomy through the particle channel with such extreme energies. Its main goals are the identification of UHECR sources by a high statistics arrival direction analysis and the measurement of the sources energy spectra to narrow down possible acceleration and emission mechanisms [3]. Also, the detection of UHE gamma photons and neutrinos as well as the estimation of their fluxes are major exploratory objectives.

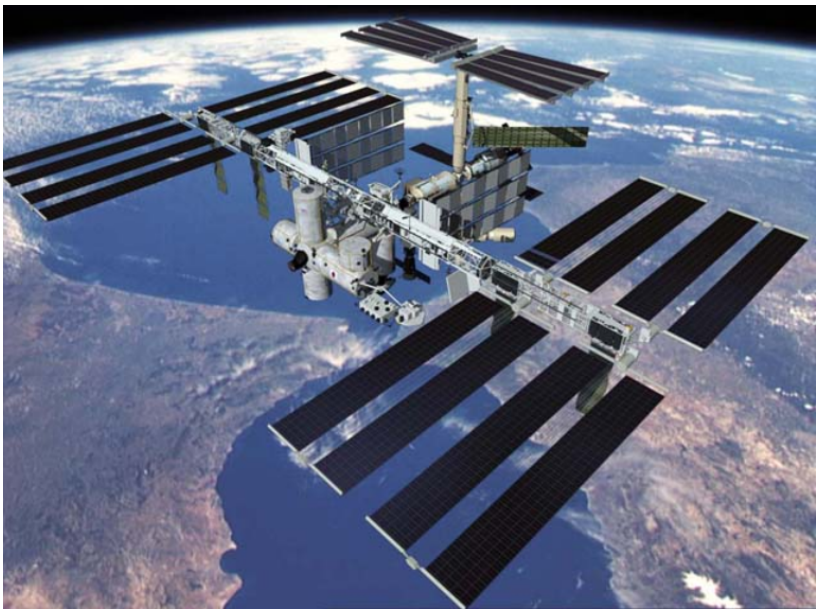

Figure 3.4: Image of the International Space Station, were JEM-EUSO will be located [64].

The International Space Station, where JEM-EUSO will be located, is a versatile

research institute and a large observation platform in outer space for scientific research and applications. It also serves as a test centre to facilitate introduction of new technologies [65]. The station has been in orbit since 1998 and is expected to remain in operation until at least 2020.

3.2.1 JEM-EUSO pathfinders

There are three JEM-EUSO pathfinders at different stages (either functioning or under construction): EUSO-Balloon, EUSO-TA and Mini-EUSO. The objectives of these pathfinder missions are: to perform a full scale end-to-end test of the JEM-EUSO concept and key technologies, to test the electronic components in stratospheric conditions, and to measure the UV background at high altitudes.

JEM-EUSO Telescope Array

EUSO Telescope Array (EUSO-TA) is a prototype of the JEM-EUSO telescope that has recently been installed in the Telescope Array site in Black Rock Mesa, Utah, USA. Its aim is to calibrate the response function of the EUSO telescope with the TA fluorescence detector in presence of a shower of known intensity and distribution, as well as to perform observations of ultraviolet light generated by cosmic ray showers and artificial sources [3]. In order to calibrate the response and to reduce the systematic errors of the measurement, EUSO-TA will make use of the LIght Detection And Ranging (LIDAR) device and the Electron Light Source (ELF) of TA for an absolute calibration, considering that the telescope is located in a shed in front of one of the fluorescence detectors of the Telescope Array collaboration, pointing in the direction of the ELF and CLF (Central Laser Facility).

EUSO-TA is a ground-based telescope that consists of one PDM and two Fresnel lenses. The Photo Detector Module (PDM) is identical to each one of the 137 that will be part of the JEM-EUSO focal surface. Each PDM is composed of 36 Hamamatsu multi-anode photomultipliers with 64 channels per tube. Thus, in overall, there will be 2304 channels in each PDM. The two square Fresnel lenses are one meter side and provide a

field of view of 8°× 8°. The upper pannel of Figure 3.5 shows the shed in front of the fluorescence tank where the EUSO-TA is located. In the lower pannel of Figure 3.5 we observe an image of the EUSO-TA structure with the two Fresnel lenses.

Figure 3.5: The shed where the EUSO-TA is located is presented in the top of the figure. In the bottom, an image of the EUSO-TA structure with the two lenses [66].

EUSO-Balloon

EUSO-Balloon is a balloon-borne experiment developed by the JEM-EUSO consortium. Its aim is to test the technologies and methods used in the forthcoming main experiment, through a series of stratospheric balloon flights that have already started in August, 2014. EUSO-Balloon, as the main mission, is an imaging UV telescope which points towards the nadir from an altitude of about 40 km. It is equipped with one PDM identical to one of the JEM-EUSO instrument, and three Fresnel lenses which are prototypes of those which will be installed in JEM-EUSO. The instrument will cover a field of view of $12^\circ \times 12^\circ$ in a wavelength range between 290 and 430 nm. In Figure 3.6 it is presented an scheme of the EUSO-Balloon structure, with the three Fresnel lenses (the crossed squares) and the PDM (grilled blue square) embebbed in a box with more components of the electronics. EUSO-Balloon also has an IR-camera, that is a stand-alone payload of the EUSO-Balloon, to retrieve the cloud coverage in the EUSO-Balloon FoV at 40 km height. EUSO-Balloon will follow the following objectives during the set of flights:

- technology demonstrator: such as High Voltage (HV) power supplies, HV switches, the Front-End Electronics, the on-board hardware and software algorithms involved in the triggering of EAS events.

- Data acquisition and background study: the observation of EAS from space through UV light has never been performed and, since JEM-EUSO observations will be sensitive to the variation of the UV background, EUSO-Balloon background measurements will be very useful for the main mission.

In Figure 3.7 it is shown the take off of the first balloon flight, held in Canada. Next EUSO-Balloon will most likely be launched in summer 2016. This flight is thought to last a couple of days.

In Table 3.1 the JEM-EUSO parameters are represented in comparison with those of the EUSO-Balloon. The pixel size and the field of view have been scaled to measure an equivalent amount of background level than the expected for the main mission.

Table 3.1: Main EUSO-Balloon parameters compared with those for the JEM-EUSO mission.

parameters	JEM-EUSO	EUSO Balloon
Height (km)	400	20
Diameter (m)	2.5	1
FoV/pix (deg)	0.08	0.25
Pixel on ground (km)	0.580	0.175
FoV/PDM (deg)	3.8	12
PDM on ground (km)	28.02	8.4

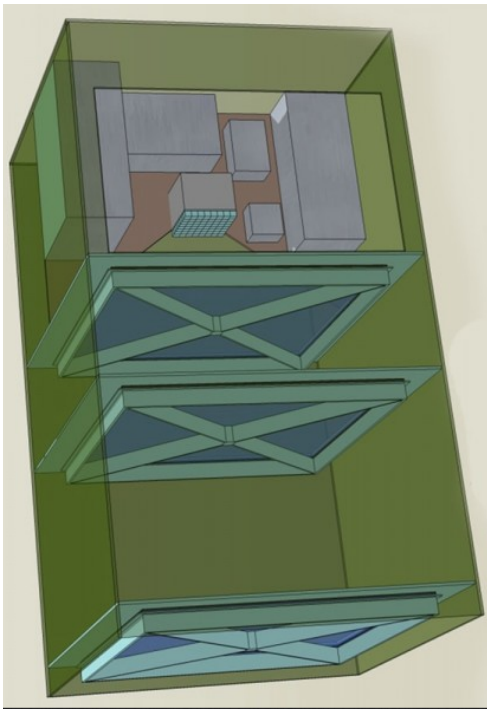

Figure 3.6: Scketch of the EUSO-Balloon with the three Fresnel lenses (the crossed squares) and the PDM (grilled blue square), embebbed in a box with more electronic components [67].

Figure 3.7: Photo of the first EUSO-Balloon take-off [68].

Mini-EUSO

The Mini-EUSO project is a small replica of the UV telescope JEM-EUSO inside the pressurized ISS. It will be located next to a UV transparent window in the Zvezda module, looking at the Earth in nadir position. It will be equipped with one full original JEM-EUSO PDM, an optical system made of two Fresnel lenses (25 cm of diameter) and a data acquisition system. Currently, Mini-EUSO is in phase A, waiting for the evaluation and final approval by the Roscosmos Scientific Committee. The Mini-EUSO mission has objectives such as [67]:

- to perform an absolute calibration of the PDMs during flight.
- To observe from the same altitude as JEM-EUSO, studying the UV background coming from the Earth in all the different reflective conditions (water, earth, vegetation, snow, etc).

- To study atmospheric phenomena, like lightnings and meteors.

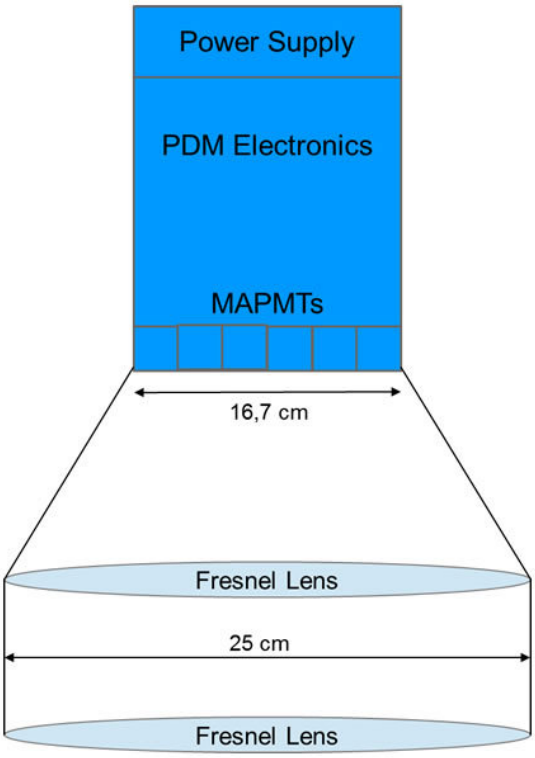

Figure 3.8: The Mini-EUSO project is a small replica of the JEM-EUSO telescope [67].

3.2.2 JEM-EUSO telescope

JEM-EUSO consists of a main telescope, sensitive to near UV, and of an Atmosphere Monitoring System (AMS). The main telescope is a fast (of the order of μs) digital camera with a wide FoV of 60°. It consists of four principal parts: the photon collecting optics, the focal surface (FS) detector, the electronics, and the mechanical structure [2].

The FS of JEM-EUSO is a curved surface of about 2.3 m diameter. It is composed of 137 PDMs. Each PDM consists of 9 Elementary Cells (EC), and each EC consists of 4 Multi-Anode PhotoMultiplier Tubes (MAPMT), with a quantum efficiency of about 40%. Therefore, the focal surface is integrated by more than 5000 MAPMTs. The MAPMTs developed for the JEM-EUSO mission are going to be tested in the TUS detector on a

Russian space mission.

The output pulse signals of the MAPMT are sent to Application Specific Integrated Circuits (ASICs) which are included in the front-end electronic circuits. The electronic counts on 64 channels of anodes from each MAPMTs. Therefore, this system consists of about 2 $\times 10^5$ channels meant to record the signals generated by the UV photons of the EAS in the FS, providing a kinematic reproduction of each track. Also, radiation tolerance of the electronic circuits in space environment is an important requirement. Then, the FS electronics is configured in three levels corresponding to the hierarchy of the FS detector system: front-end electronics at an EC level, PDM electronics common to 9 EC units, and FS electronics to control 137 units of PDM electronics.

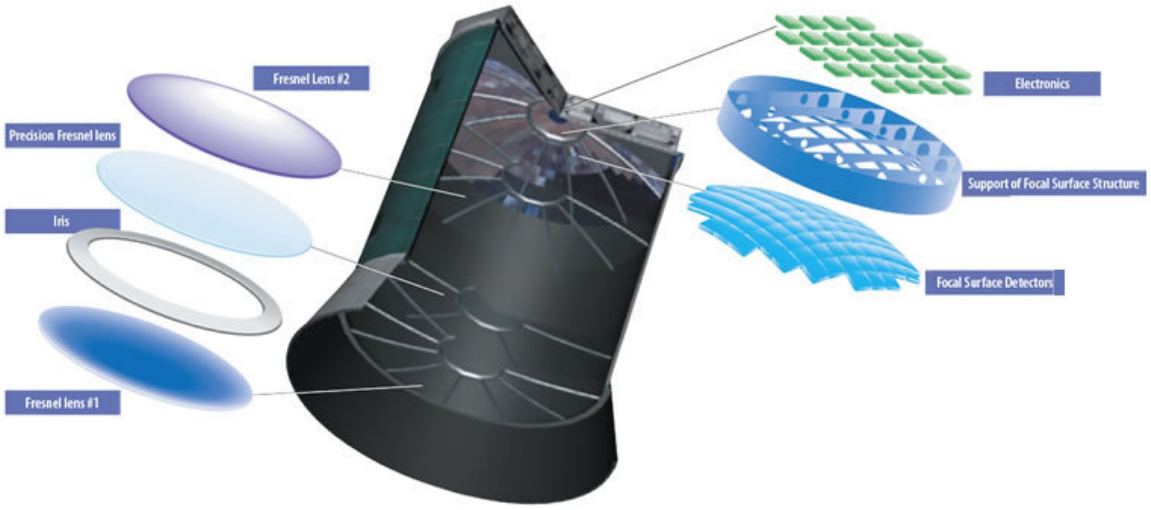

Figure 3.9: JEM-EUSO telescope [3].

The optics focuses the incident UV light onto the focal surface with an angular resolution of 0.1°. The latter converts the incident photons to electric pulses, which are counted by the electronics in a period lower than 2.5 μs. When a signal pattern of an EAS is found, the trigger is activated. The EUSO's optical design is required to be compact, constrained by the allocated mass and diameter for use in space. Only refractive systems

could satisfy the full set of the logistic constraints imposed by the EUSO requirements and the ISS transport vehicles. Two curved double sided Fresnel lenses with 2.65 m external diameter, a precision middle Fresnel lens and a pupil constitute the optics of the JEM-EUSO telescope. The Fresnel lenses can provide a large-aperture, wide FoV optics with low mass and high UV light transmittance. The combination of 3 Fresnel lenses achieves an angular resolution of 0.07° over the 30° FoV. These lenses will be made by the diamond turning manufacturing method (a process of mechanical machining of precision elements). The material of the lens is CYTOP and UV transmitting PMMA which has high UV transparency in the wavelength from 330 nm to 400 nm. Precision Fresnel optics adopting a diffractive optic technology are used to suppress the color aberration.

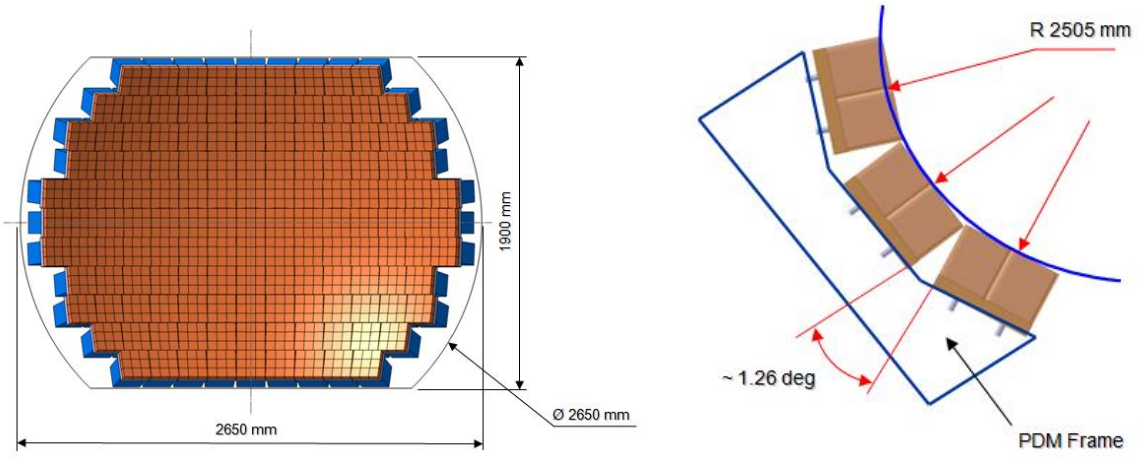

Figure 3.10: Focal Surface front view in the left pannel. PDM Spherical Shape in the right one [69].

The FS main mechanical structure is composed by two head master frames, connected by two side frames and ten supporting "ribs" lying along the parallels of the focal surface sphere. The mechanical structure for each PDM (containing 3 × 3 Elementary Cells, with 2 × 2 MAMPTs each one) is designed to place the 9 ECs on a spherical surface (with a radius 2.505 m). The frame containing the ECs is built by machining a single aluminum alloy piece, with a mass reduction, at the end of machining, larger than 87% (from 2.7 kg

to 0.330 kg). This structure is connected to the main FS structure, contributing to the overall rigidity and strength. The PDM layout is formed by 5 aluminum alloy frames that support 6 electronic boards: one for PDM electronics, another for High Voltage, three boards for Power Distribution and a last optional board. The total mass of each PDM mechanics is 0.624 kg [63].

3.3 Atmospheric Monitoring System

Since JEM-EUSO covers a wide observation area, different atmospheric conditions will take place at the same time inside its FoV [70]. Therefore, an atmospheric system is needed to monitor the properties of the atmosphere where the EAS occurs. The goal of the JEM-EUSO AMS is to provide information on the distribution and properties of the atmosphere features (such as cloud or aerosol layers) within the telescope FoV [5, 71].

The main requirements on the precision of measurements of these layer characteristics are determined by the requirements on the precision of measurement of EAS parameters [63]:

- measurement of EECR energy with precision 30%,
- measurement of the depth of the shower maximum with precision 120 g/cm^2.

The energy of an UHECR is proportional to the intensity of the emitted UV fluorescence light from the EAS. Thus, the uncertainty on the energy will depend on the uncertainty of the measured extinction atmospheric properties. In order to have an energy uncertainty inside the requirements, it is needed to measure the optical depth (τ) profile of the atmosphere with an accuracy of $\Delta\tau \leq 0.15$. The precision of the measurement of the depth of shower maximum, on the other hand, is affected by the uncertainties of the clouds and aerosols location. Then, the altitude of the atmospheric features is needed to be measured with a precision in altitude of $\Delta H \leq$ 500 m.

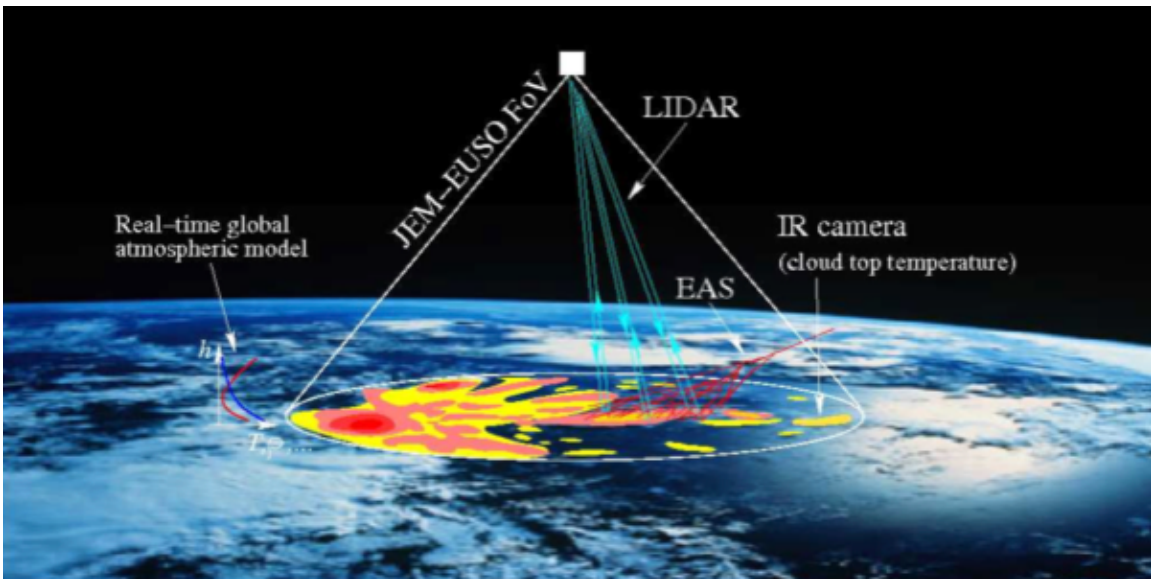

Figure 3.11: An scheme of the JEM-EUSO Atmospheric Monitoring System and its different parts [72].

The AMS will consist of [72]:

1. Infrared (IR) camera,

2. LIght Detection And Ranging (LIDAR) device,

3. Global Light System (GLS),

4. Global atmospheric models from the post-analysis of all available meteorological data by global weather prediction services like European Centre for Medium-Range Weather Forecasts (ECMWF) and Global Modeling and Assimilation Office (GMAO).

An scheme of the JEM-EUSO AMS with its different parts is shown in Figure 3.11. It is shown how the IR camera takes an image of the FoV meanwhile the LIDAR is shooted in different positions along the EAS.

3.3.1 Infrared Camera

The AMS IR Camera is an infrared bi-spectral system meant to detect the presence of clouds in the JEM-EUSO FoV, as well as to obtain the cloud coverage and cloud top altitude during the observation period of the main instrument. The FoV of the IR-Camera will totally match the FoV of the JEM-EUSO telescope, having an angular resolution, which corresponds to one pixel, of about 0.1°. Since the measurements will be performed at night, the IR camera will be based on cloud IR emission. The observed radiation is related to the atmospheric (or cloud) temperature and emissivity. The IR camera retrieval of the cloud top altitude is also planned to be performed on-ground by using stereo vision techniques or radiometric algorithms. Therefore, the IR camera preliminary design is thought to be compliant with both types of data processing [3].

3.3.2 LIDAR

The most relevant information we need to consider about the absorption and scattering properties of clouds is at the height at which the EAS events develop. To get this information, the LIDAR will have a re-pointing capability. The laser beam will be shot in several directions around the location at which the EAS event has triggered, measuring the optical depth profiles of the atmosphere in these selected direction. This measurement will be done thanks to the laser backscattering signal (which will be received by the main JEM-EUSO telescope) in several directions around the supposed EAS maximum. The accuracy will depend on the angle between the direction of the laser beam and the nadir θ_z as following: $375/\cos(\theta_z)$. During the time interval between subsequent triggers, the LIDAR will re-point to the direction in which the EAS trigger occurred. The re-pointing of the laser beam will be done with the help of a steering mirror with two angular degrees of freedom and tilting angle of maximum ±15°. Therefore, the LIDAR can retrieve the optical depth of the atmosphere only for a certain direction. The laser pulse energy will be 20 mJ, and the return signal from laser will allow to detect cloud/aerosol layers with $\tau \geqslant 0.15$ at 355 nm wavelength. Also, the LIDAR measurements can provide a

complementary measurement of the cloud height determined by the IR camera [3]. The beam will have 2 mrad divergence, matching the angular size of JEM-EUSO pixels. The footprint size of the laser beam on ground will be ∼800 m. Thus, the laser beam energy density there will be orders of magnitude below the limits imposed by the standard laser safety requirements [73].

3.3.3 Global Light System

The Global Light System (GLS) is a worldwide network, that combines ground-based xenon flash lamps and lasers to provide a method of validating the UHECRs intrinsic luminosity, its arrival direction and the trigger efficiency. The GLS will generate benchmark optical features in the atmosphere with characteristics similar to the optical signals of EAS. But unlike EAS, the number, rate, intrinsic luminosity, precise time and direction (in the case of the lasers) are known. There will be twelve ground-based units around the world. Six will have both xenon flashers and a steerable laser. The remaining six will have only xenon flashers. There will also be one airborne GLS-XL unit [74].

During its flight, JEM-EUSO will reconstruct the pointing directions of the lasers and the intrinsic luminosities of the lasers and flash lamps. The laser shots will be used to monitor JEM-EUSO's trigger efficiency. They will also point to known astronomical sources. Their reconstructed pointing direction will be compared to their known directions. With this comparison, the accuracy in the measurement of the UHECRs arrival directions can be estimated. The xenon flash lamps provide UV light flashes of known intrinsic luminosity. These flashes will be recorded by the instrument to be reconstructed. By comparing the reconstructed ones with the calibrated luminosities of these flashes, the accuracy of the energy measurements of UHECRs can be determined [75].

3.3.4 Global Atmospheric Model Data

Precision of the analysis of IR camera and LIDAR data is improved when the basic atmospheric parameters (such as temperature, pressure profiles, humidity...) in the observed

region are known. Such parameters are daily collected by atmospheric weather forecasting such as ECWMF in Europe or GMAO and NCEP in USA, and also provide information on the presence and altitude distribution of cloud and aerosol layers. These models are used as input for the Global Atmospheric Models (GAM), which are models that generate the atmospheric conditions for the entire Earth. Thus, real time global atmospheric models are very useful for the JEM-EUSO Atmospheric Monitoring System.

3.4 JEM-EUSO Infrared Camera Design

The IR Camera is the instrument devoted to detect clouds and determine their top height in the FoV of the JEM-EUSO main instrument, by providing a 2D image of the cloud top temperature [4]. It is being designed, developed and tested by the JEM-EUSO Spanish Consortium. Also, a dedicated End to End (E2E) simulation for the IR Camera is under development, which will give us answers in key points of the design, such as the compression algorithms evaluation or the estimation of the expected accuracy of the calibration options foreseen. The IR Camera preliminary design can be divided into three main blocks: the Telescope Assembly, the Electronic Assembly and the Calibration Unit [76].

Telescope assembly

The IR Camera Telescope assembly is comprised of the Infrared detector (μbolometer), the Front End Electronics (FEE), and the Optical lens assembly:

The infrared detector (UL04171, from the ULIS Company) measures the power of incident electromagnetic radiation via the heating of a material with a temperature-dependent electrical resistance. The working operative temperature is around 30°C. A dedicated Thermo-Electric Cooler (TEC) is implemented to guarantee a user-defined temperature within $\pm$10 mK. The FEE communicates the μbolometer and digitalize the signal. The optical system design has a refractive objective, based in a triplet, with one more lens close to the stop and a window for the filters close to the focal plane.

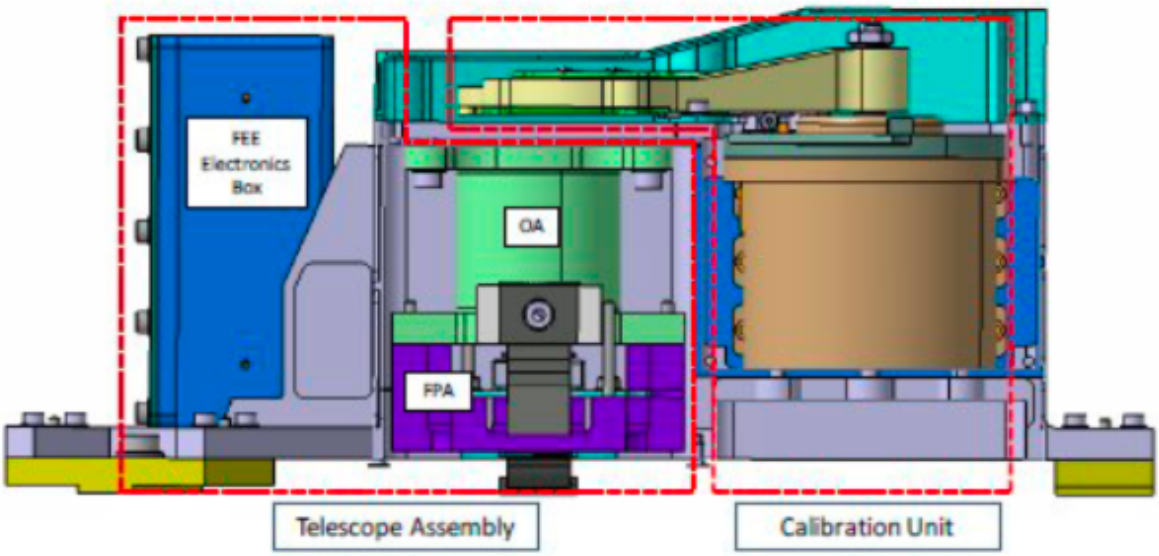

Figure 3.12: JEM-EUSO IR camera [72].

Electronic assembly

The Electronic Assembly provides mechanisms to process and transmit the obtained images. It consists of two main sections: the Instrument Control Unit (ICU) and the Power Supply Unit (PSU). The ICU processes the data generated by the FEE. It also controls several aspects of the system management, such as the electrical system or the thermal control. The PSU receives the main power from the main telescope and regulates the power to the system and the subsystems [77].

The calibration subsystem

The calibration unit is dedicated to control the IR calibration operation. This unit guarantees a internal temperature reference to ensure the calibration of the data coming out of the FEE. The calibration unit is mainly composed of two black bodies and a temperature-controlled shutter, a moving mechanism and motor, a positioning system, and a calibration thermal control.

Chapter 4

Simulation and reconstruction bases: ESAF

The EUSO Simulation and Analysis Framework (ESAF) is one of the official JEM-EUSO softwares, meant to provide a full set of tools for EAS simulation, reconstruction and analysis for space-based cosmic observations. It includes shower generation, a complete description of the atmosphere, emission and transport of photons, ray trace of optics, photodetector response and telemetry, as well as reconstruction. Key parts of ESAF were developed in EUSO project and nowadays the software is adapted and optimized for JEM-EUSO instrument [78].

In ESAF, EAS events are generated along with the emission of fluorescence and Cherenkov photons and their propagation in the atmosphere. UV photon propagation through atmosphere severely involves Rayleigh scattering and absorption by ozone in short wavelengths ($\sim$ 320 nm). The transmittance of these processes is modeled by LOWTRAN package. ESAF is written in C++ language with some small parts in FORTRAN.

ESAF uses as default EAS generators UNISIM and Shower initiated Light Attenuated to the Space Telescope (SLAST). UNISIM is a stand-alone package based on a hybrid simulation approach. SLAST follows an EAS parametrization and it is able to generate EAS initiated by different primary particles. It also simulates the light transmission

in atmosphere either using analytical descriptions of Rayleigh and Mie scattering either through the LOWTRAN algorithm. Apart from their own EAS generators, ESAF can also read the air showers generated with programs such as CORSIKA.

The output of the ESAF simulation and reconstruction is a ROOT file with a structure that contains the information we would expect from real data. The level of detail is user-configurable [24].

4.1 Fluorescence radiation

The primary energy of a cosmic ray is shared among the EAS secondary particles. Most of them are electrons and positrons which carry about the 90% of the primary energy. These electrons and positrons deposit their energy in the atmosphere by exciting or ionizing the air molecules, that are later on de-excited by emitting fluorescence photons. Most of these photons in the wavelength range between 300 nm and 400 nm are originated from transitions of the second positive (2P) system of molecular nitrogen and the first negative (1N) system of molecular nitrogen ions [79]. The air fluorescence emission depends on pressure, on the temperature and on the steam content in air. This dependence of the number of fluorescence photons (per unit wavelength and per unit slant depth) is given by [80]:

$$\frac{d^2 N_\gamma^0}{dX d\lambda} = Y(\lambda, P, T, p_s) \frac{dE_{dep}^{tot}}{dX} \tag{4.1}$$

where $Y(\lambda, P, T, e)$ is the fluorescence yield, which depends on wavelength λ, air pressure P, air temperature T, and steam pressure p_s. The deposited energy of the secondary particles is denoted as $\frac{dE_{dep}^{tot}}{dX}$. In Figure 4.1 it is shown the simulation with ESAF of the fluorescence propagation in the atmosphere for the zenith angles 30°, 45°, 60° and 75°. It can be observed that not only the total number of produced photons but also their production in time strongly depends on the arrival direction.

The main contributing transition lines are the 2P at 337.1 nm, 357.7 nm and 315.9 nm and the 1N at 391.4 nm and 427.8 nm, as can be observed in Figure 4.2(a). Note that emission lines around 400nm or higher look weaker. This is due to the transmission

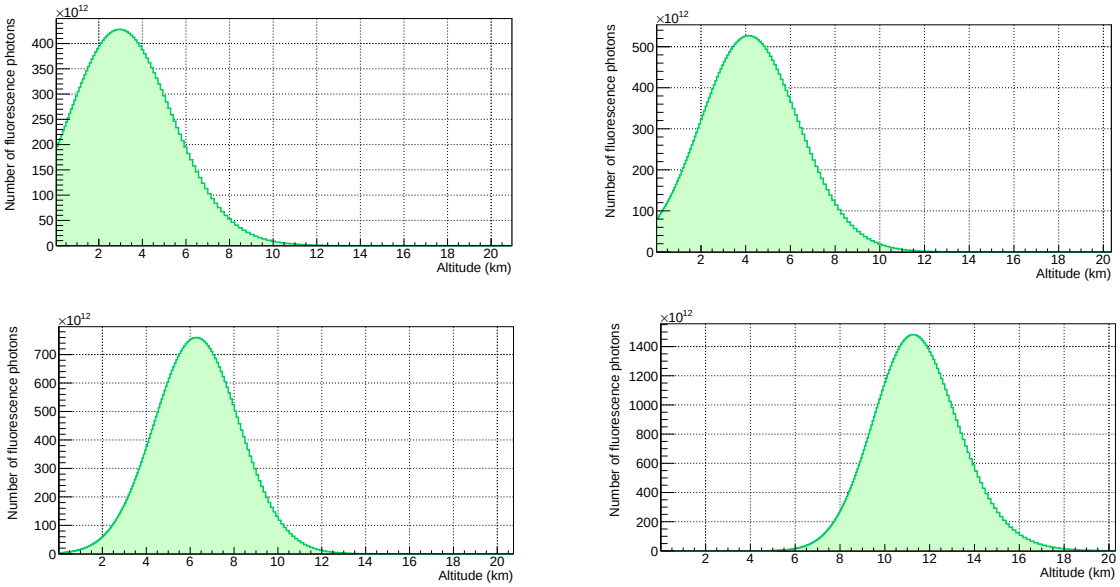

Figure 4.1: Number of fluorescence photons produced in the atmosphere by a proton of energy 10^{20}eV and four different zenith angles (30°, 45°, 60° and 75°). We can observe that the altitude of the emission strongly depends on the zenith angle of the primary particle.

efficiency of the JEM-EUSO optics (see Figure 4.2(b) [81]). It is important to consider that Figure 4.2(b) represents the transmission efficiency per mm, while the width of the JEM-EUSO filters is 2mm.

The dependence of the fluorescence yield on atmospheric conditions results in an atmospheric dependence of the reconstructed cosmic ray energy and the depth of shower maximum (which is an indicator for the mass of the primary cosmic ray particle). For instance, the shower development produced by a proton at high temperatures is very similar to that produced by an iron particle in lower temperatures at the same energy and the same inclination [82]. Therefore, it is extremely important to monitor atmospheric conditions inside the JEM-EUSO FoV.

The observation of the fluorescence EAS signal from space (such as JEM-EUSO experiment) avoids the scattering produced by aerosols, which are limited to low altitudes. Moreover, since the EAS maximum takes place at altitudes higher than 3 km from ground,

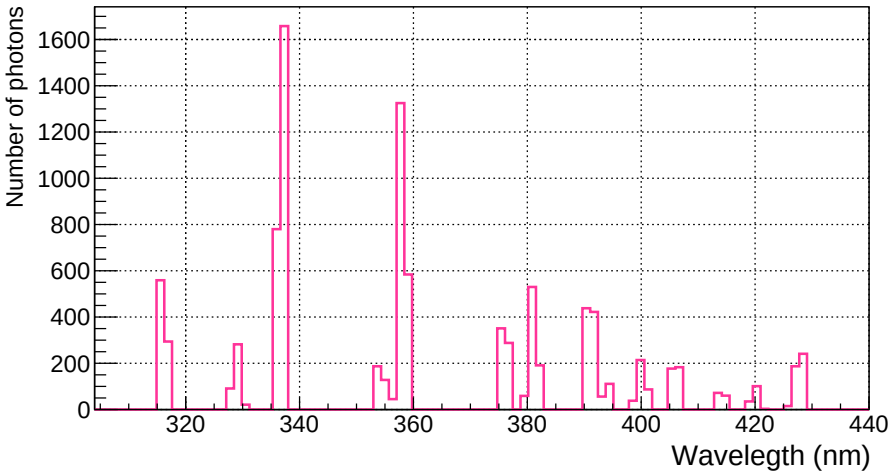

(a) The fluorescence emission lines of N_2 from 300nm to 430 nm.

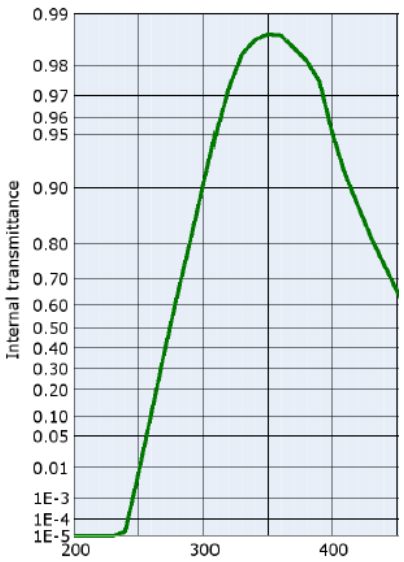

(b) BG3 filter transmitance between 200 and 450 nm.

Figure 4.2: Fluorescence emission lines of N_2 and the transmitance of the JEM-EUSO filter per mm in the UV wavelength.

the measurements will be possible even in some cloudy sky conditions. Then, atmospheric properties, probability of presence of clouds and their influence need to be considered.

4.2 Cherenkov radiation

The EAS secondary particles travel faster than the speed of light in the atmosphere, which has a refractive index higher than one. As a result, they induce the emission of Cherenkov light in a narrow, forward-beamed cone. The opening angle of the cone along the secondary particle track direction is [83]:

$$\cos\theta = \frac{1}{\beta n} \tag{4.2}$$

where n is the refractive index of the medium and $\beta = v/c$, being v the speed of the particles in the medium and c, the speed of light in vacuum. Thus, in EAS the Cherenkov yield depends on the refractive index of the atmosphere, which itself depends on the wavelength of the emitted light as well as on the temperature, pressure and humidity. In Figure 4.3 it is represented the EAS Cherenkov propagation through the atmosphere.

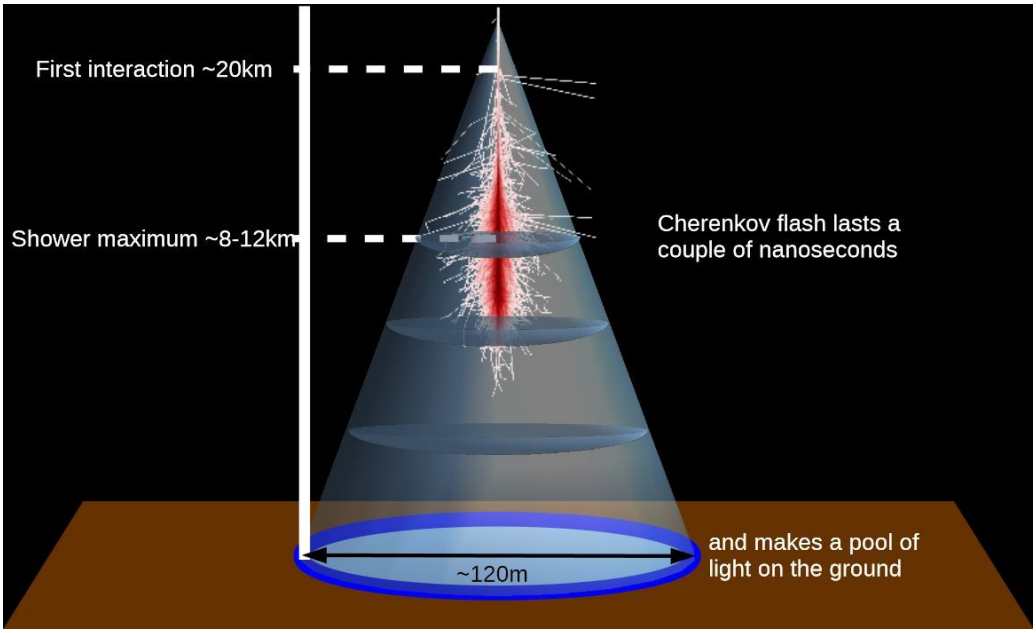

Figure 4.3: Cherenkov propagation diagram [84].

Contrary to fluorescence, Cherenkov yield decreases rapidly with altitude. Nevertheless, the number of Cherenkov photons produced all along the shower track ($\simeq 3 \times 10^{15}$ at

10^{20} eV) is of the same order as the fluorescence one. However, due to both components propagation method, their features in the detected signal by JEM-EUSO will be different. Figure 4.4 represents an ESAF simulation of the EAS Cherenkov propagation that shows how the number of propagated Cherenkov photons also vary with the shower zenith angle of the EAS arrival direction. Cherenkov intensity reaches a maximum for shower zenith angle around 50°. In case of larger zenith angle, development of showers occurs at higher altitudes, where the Cherenkov yield is weaker. Quasi-vertical showers may reach the Earth ground before their development ends, and Cherenkov photon production is not complete [85].

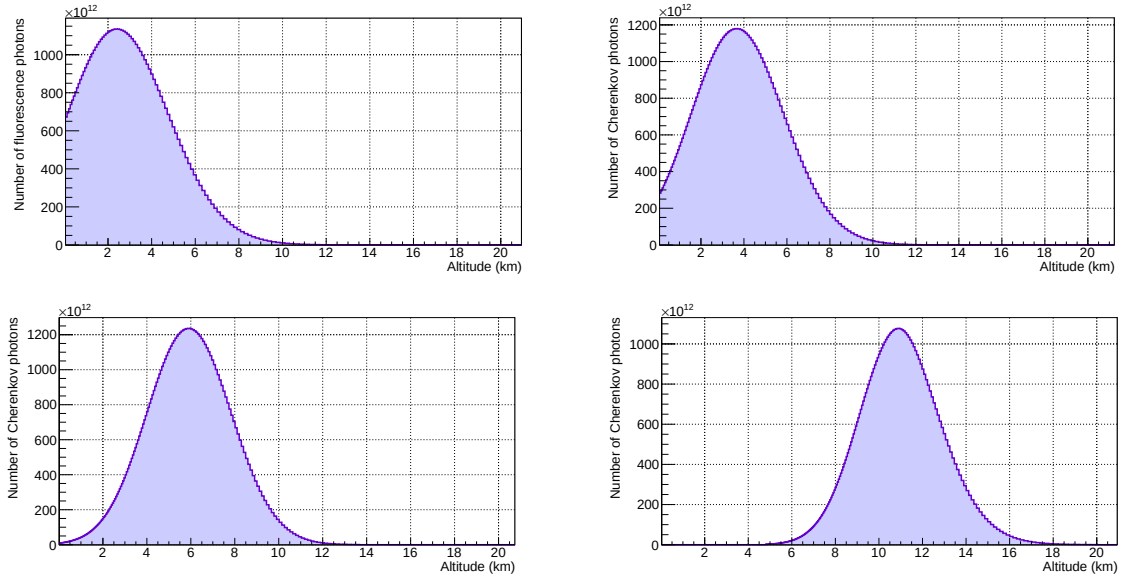

Figure 4.4: Number of Cherenkov photons produced in the atmosphere for a proton of energy 10^{20}eV and four different zenith angles (30°, 45°, 60° and 75°).

4.3 Photons simulation

The ESAF simulation code is structured in different steps that are shown in Figure 4.5. The steps would comprehend: the photon emission in the atmosphere, the photons propagation through the atmosphere (until the detector pupil), the simulation of the telescope

optics (lenses and FS), the simulation of the FEE (with the simulation of photoelectrons as outcoming light) and the simulation of the trigger (and the final event as the result). To provide the user an easy access to the data, a set of detector event viewers is provided with ESAF [85]. However, any user who wants to analyze a specific feature of the event, can create its own viewers in ROOT.

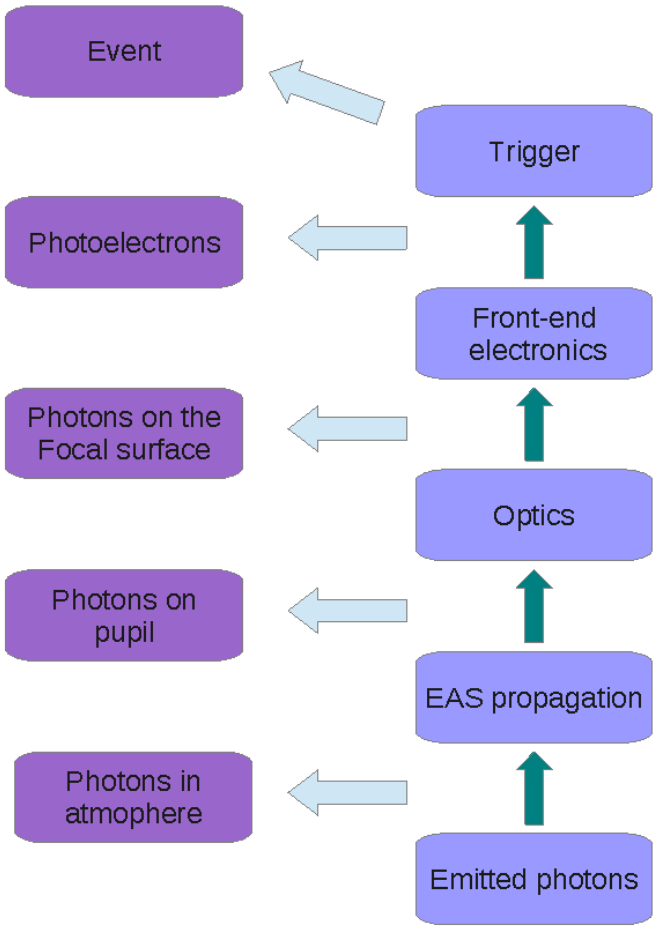

Figure 4.5: An scheme of the ESAF structure since the photons are emitted in the atmosphere until their arrival to the telescope.

Then, there are three main signal stages for the incident light (since its arrival to the telescope to the counting in the electronics) that are taken into account in ESAF. This software allows us to analyse the *photons* (i.e., when the signal arrives to the optics),

as well as the *photoelectrons* (created in the electronics) and the *photoelectron counts* (the signal at the FEE stage). When the EAS photons come from the optics to the electronics, photomultipliers convert the radiation into electrical signals by the use of the phenomenon of photoemission within the photomultipliers. Afterwards, the photoelectrons are converted to electric pulses in the ASIC of the elementary cell. During the conversion from photons to photoelectron counts in the electronics, the signal suffers from three types of losses: absorption in the optics and the quantum efficiency of the photosensor, blurring of the spot on the FS due to aberration of the optics, and the geometrical inefficiencies of the FP [24].

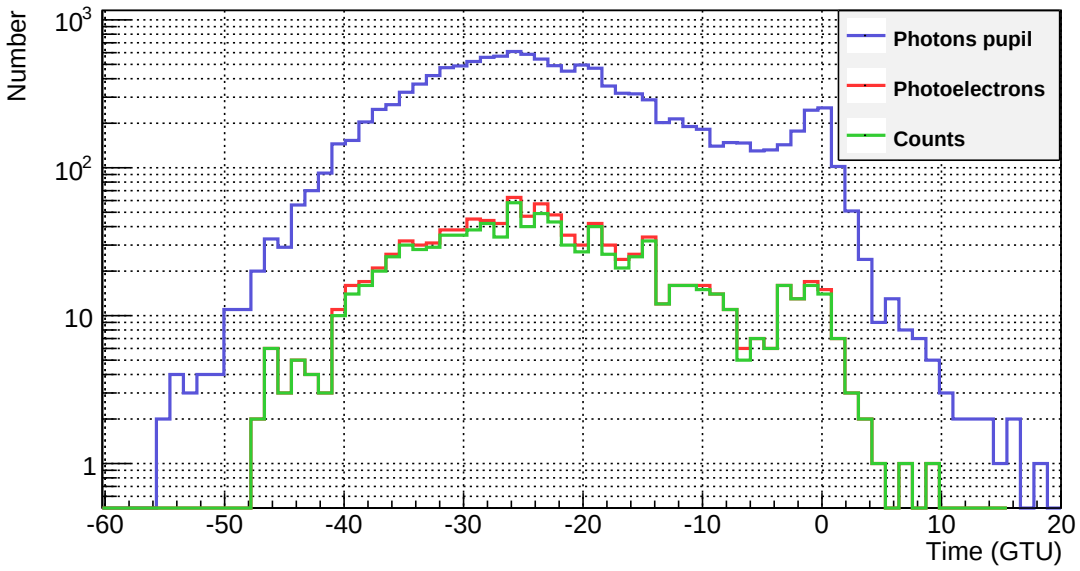

Figure 4.6: Number of photons produced by an EAS of θ=60° and $E = 10^{20}$eV, photoelectrons produced by these photons inside the JEM-EUSO electronics, and number of counts produced by these photoelectrons in the FEE.

In Figure 4.6 it is represented these three stages for the same shower in logarithmic scale. We can observe the reduction of the number of photoelectrons compared to the number of photons due to the former losses. Also, the number of photoelectrons are very similar to the counts. The reason is that one count is only equivalent to more than one

photoelectron in rare cases, such as when several photoelectrons come to the same pixel in a very short period of time.

4.4 Extensive Air Showers simulation

EAS light coming to the telescope is observed as a spot moving at the speed of light [6]. EAS light curves (number of photons detected by the telescope as a function of time) have different shapes depending on the incident angle of the shower. Horizontal showers

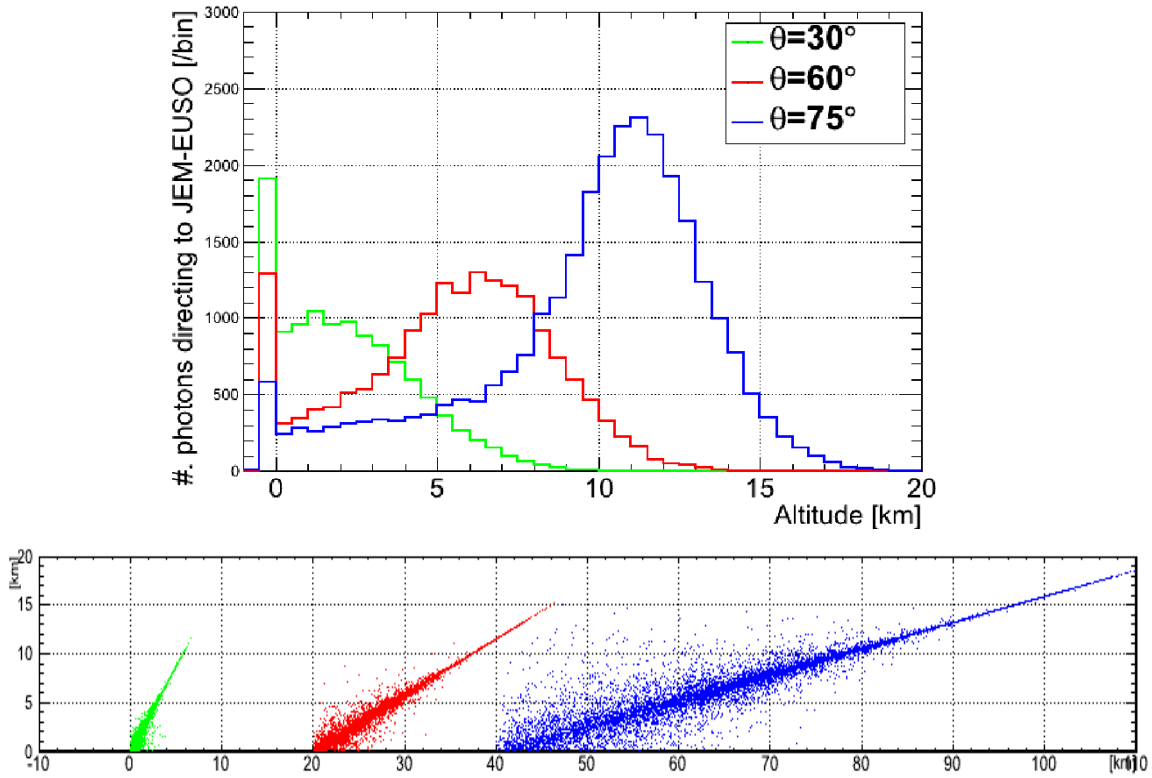

Figure 4.7: In the upper pannel, it is represented the light curve of three showers of 10^{20} eV with θ =30°, 60° and 75°. The altitude of the shower development strongly depends on the arrival direction of the shower. In the lower pannel, the image on the FP for the three showers is shown.

develop higher in the atmosphere, producing more photons in a wider period of time

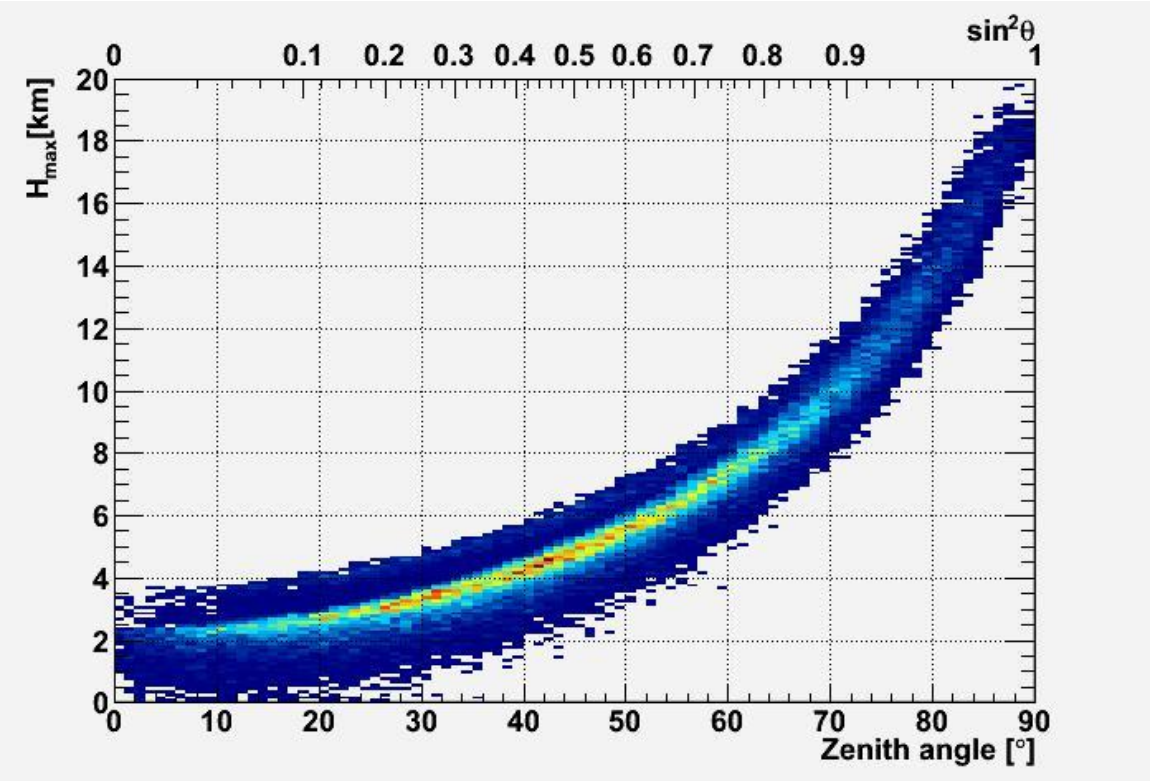

Figure 4.8: Altitude at which the shower maximum takes place as a function of the arrival direction.

than vertical showers, whose development takes place deeper in the atmosphere, where the density is higher. In Figure 4.7 we observe the light curve that an equivalent shower (same primary particle and same energy) will produce for three different arrival directions (30°, 60° and 75°). Unlike ground-based telescopes, JEM-EUSO will detect better more horizontal showers, since they are brigther and their shower track is longer. Moreover, more inclined showers will arrive to the ground before ending their development.

In Figure 4.8 it is represented for 10^6 proton-induced shower simulations the altitude of their shower maxima depending on the arrival direction of the shower. We observe that, as stated before, more horizontal showers develop higher in the atmosphere, and thus, their shower maximum takes place at higher altitudes than the shower maximum for less inclined showers.

But not only the EAS development vary with the incident angle. In ESAF it is possible

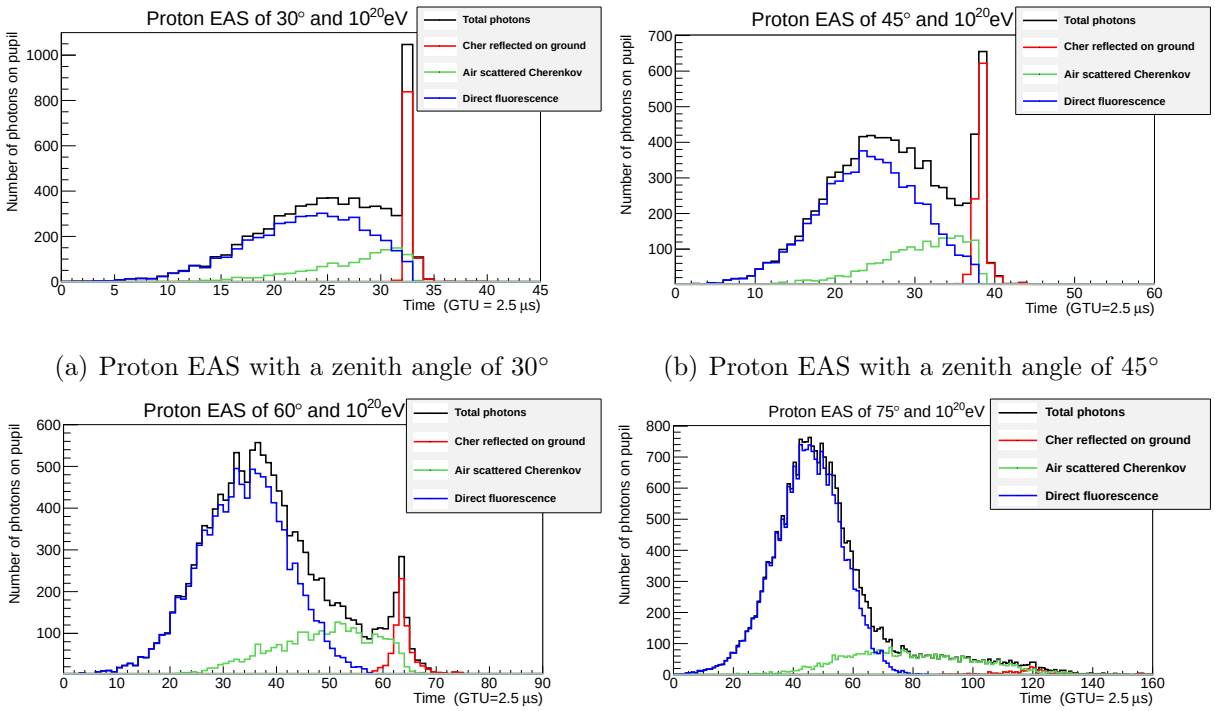

(a) Proton EAS with a zenith angle of 30°

(b) Proton EAS with a zenith angle of 45°

(c) Proton EAS with a zenith angle of 60°

(d) Proton EAS with a zenith angle of 75°

Figure 4.9: Cherenkov and fluorescence light components (reflected Cherenkov on ground, scattered Cherenkov in air, direct fluorescence and total signal) for a proton-induced shower arriving at different zenith angles (30°, 45°, 60° and 75°), and with an energy of $E = 10^{20}$ eV.

to simulate EAS from different primary particles. In Figures 4.9 and 4.10 it has been plotted different shower conditions for iron and proton for comparison. We have chosen these two primaries because iron is the heaviest nuclei which can iniciate a secondary chain, meanwhile proton is the lightest one. Some other particles such as neutrinos are also included in ESAF. Main difference between proton showers and iron showers is that iron-induced shower starts developing earlier, the associated shower maximum is smaller and statistically fluctuates less around its mean value [86]. The reason to this earlier development is that the iron-air interaction cross section is four times higher than the proton-air interaction cross section.

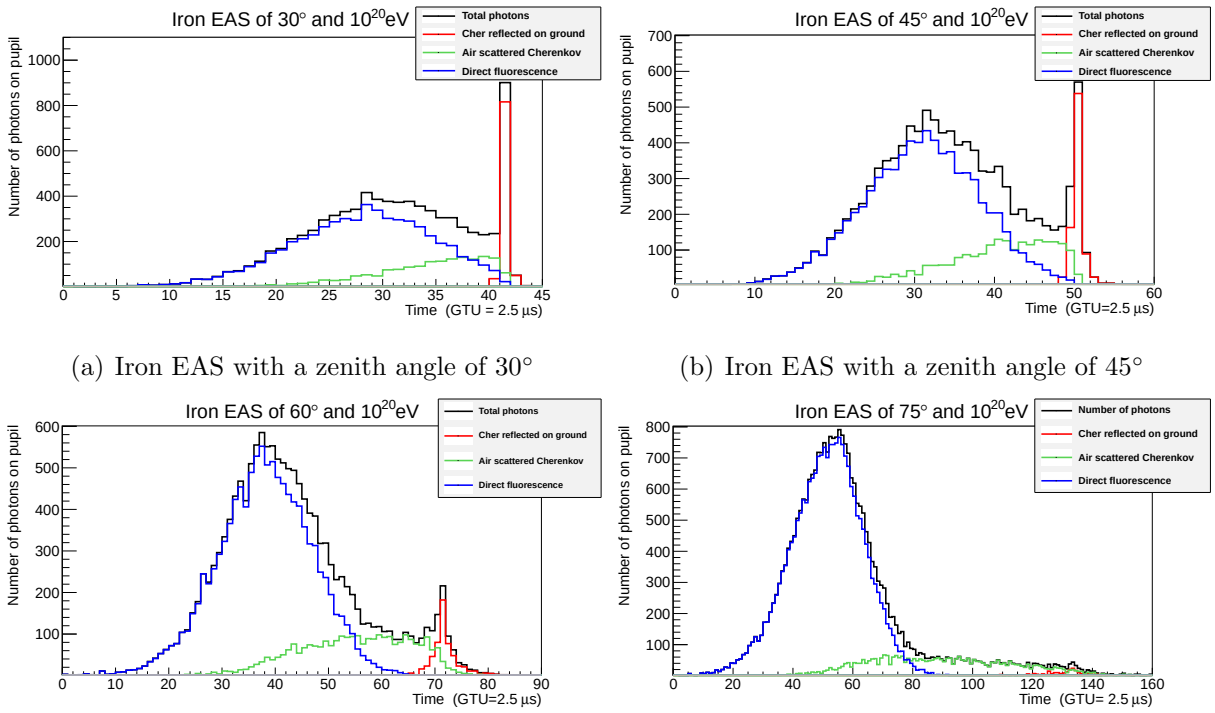

(a) Iron EAS with a zenith angle of 30°

(b) Iron EAS with a zenith angle of 45°

(c) Iron EAS with a zenith angle of 60°

(d) Iron EAS with a zenith angle of 75°

Figure 4.10: Cherenkov and fluorescence light components (reflected Cherenkov on ground, scattered Cherenkov in air, direct fluorescence and total signal) for iron primary particles at different zenith angles (30°, 45°, 60° and 75°), and with an energy of $E = 10^{20}$ eV.

4.5 EAS in different locations of the FS

Another important factor to consider is the location in the FoV where an EAS has taken place. EAS landing at the center of the FoV have their line of sight (which is the line between the detector and the landing point) perpendicular to the detector plane. Therefore, they have the shortest distance between the landing point and the telescope that we can have. EAS occurring at the edge of the FoV, on the other hand, do not only have a longer line of sight, but might not even take place enterelly inside the FoV. Therefore, shower is not only fainter but shower track might be shorter than that for the former case.

In the upper pannel of the Figure 4.11 we observe the position of two EAS photons detected by the telescope on the FS. It is well distinguished that the shower track of the

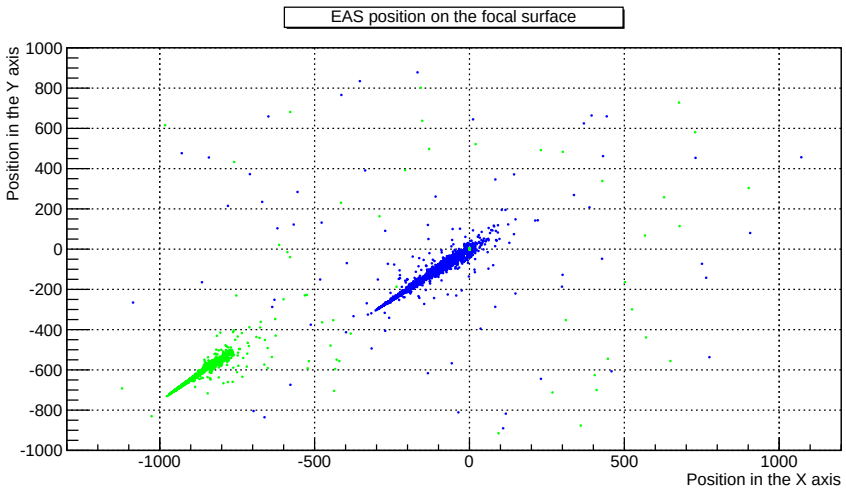

(a) EAS image for a standard shower depending on the position of the FoV

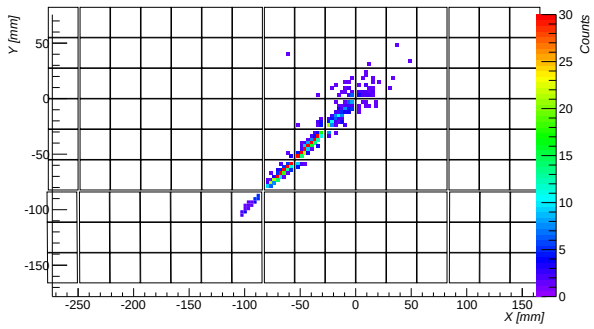

(b) EAS image on the focal plane for the EAS landing at the center of the FoV

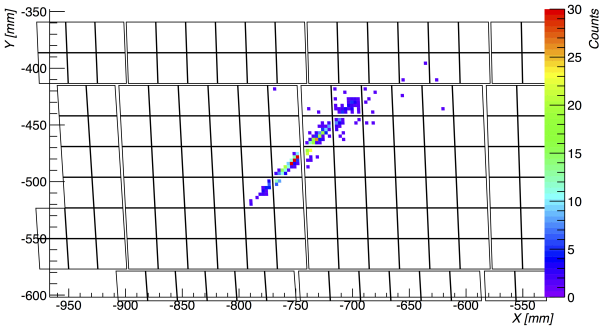

(c) EAS image on the focal plane for the EAS landing at the edge of the FoV

Figure 4.11: EAS images at different positions of the FoV

EAS in the center (blue signal) is longer than the one located at the edge of the FoV (green signal). The images in the bottom pannel correspond to the counts produced in every pixel of the FS by both EAS (the centered is the one on the left, and the one at the edge is on the right part). For the one on the right, the signal is fainter (less photons are detected by the pixels). It is important to clarify that the brightest part of the EAS image is not always the shower maximum, since some photons might have arrived in different Gate Time Unit (GTU). To clearly identify the shower maximum, the distribution of photons as a function of time is needed.

4.5.1 EAS arrival time

Then, we need to consider that the number of EAS photons as a function of time also depends on the EAS location inside the FoV. In Figure 4.12 the photons distribution along the arrival time for one shower in two different locations of the FoV has been plotted. As can be observed, the shower produced further from the center of the FoV produces in the detector a shorter signal in time.

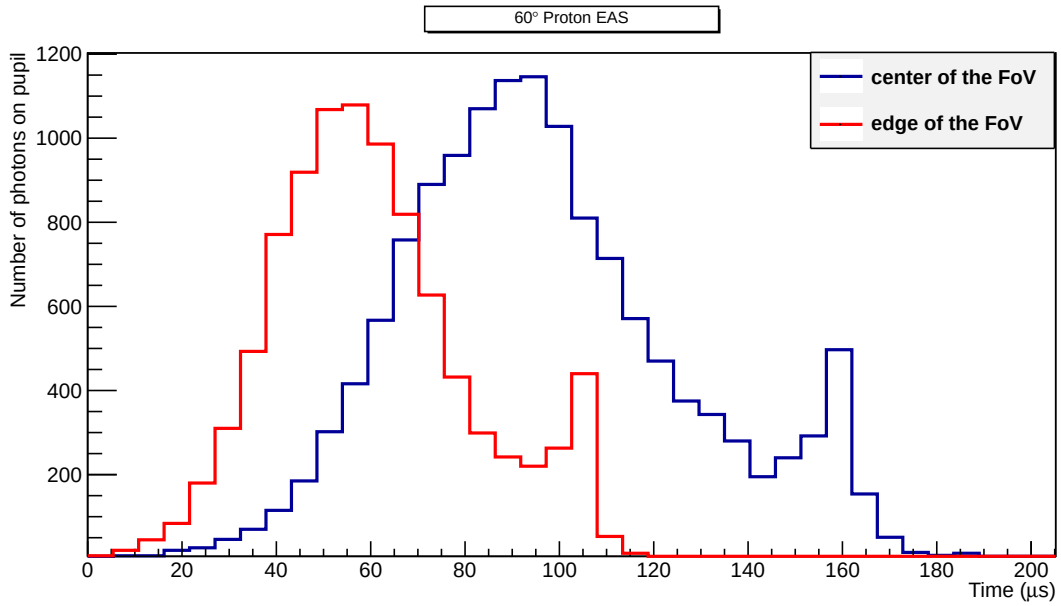

Figure 4.12: Number of photons on pupil as a function of time depending on the position of the FoV. From the comparison between the blue line (centered EAS) and the red line (EAS at the edge) we can point out that more photons are detected in the former case. Also, its light curve is longer in time.

To understand this effect, we need to describe with equations the relation between the photons arrival time and their position in the FoV for EAS developed as in Figure 4.13. Thus, we calculate the difference in the arrival time between the beginning and the end of the shower. For a shower landing in the center of the FoV (Figure 4.13, left) we assume that t_1 is the time when the first photon is produced (assumed to be cero for simplicity), and t_2 is the time when the last EAS photon is created. Both photons arrive

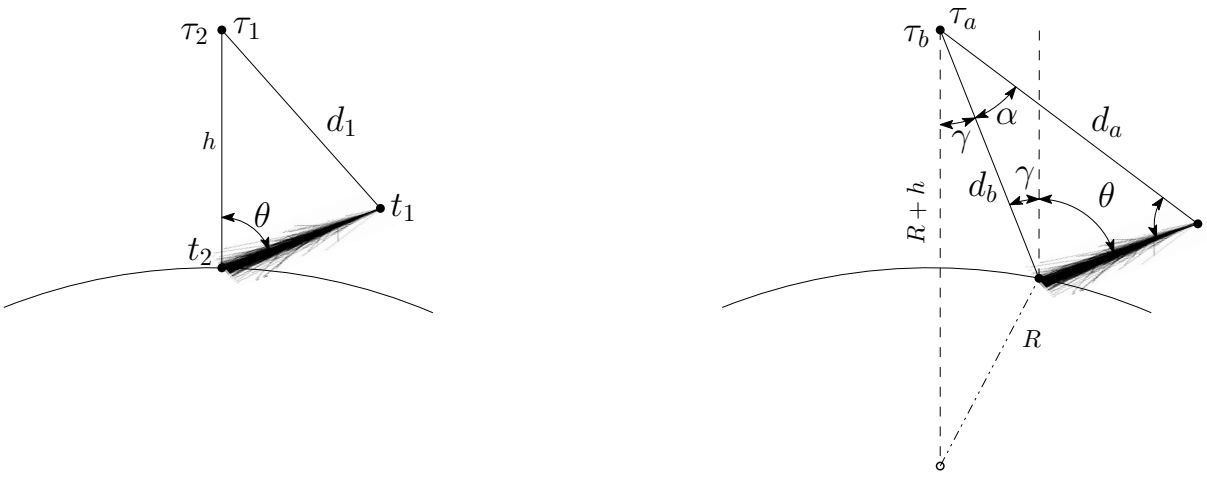

Figure 4.13: Photons reaching the telescope for a standard shower centered on the FoV (on the left) or at the edge of the FoV (on the right).

to the telescope with a time difference $\tau_2 - \tau_1$ which corresponds to:

$$\tau_1 = \frac{d_1}{c} = \frac{\sqrt{h^2 + l^2 - 2lh\cos\theta}}{c} \tag{4.3}$$

$$\tau_2 = \frac{(l+h)}{c} \tag{4.4}$$

$$\tau_2 - \tau_1 = \frac{(h+l) - \sqrt{h^2 + l^2 - 2lh\cos\theta}}{c} \tag{4.5}$$

where d_1 is the distance from the emission point of the first photon to the telescope, h is the distance between the emission point of the last photon to the telescope, l is the longitude of the shower and θ is the zenith angle.

For a shower landing at an angular distance γ from the center of the FoV (Figure 4.13, right), t_a is the time of the first photon emission (also cero for simplicity), and t_b is the time of the last EAS photon emission. Both photons arrive to the telescope in a time difference $\tau_b - \tau_a$, being τ_a and τ_b:

$$\tau_a = \frac{d_a}{c} = \frac{\sqrt{d_b^2 + l^2 - 2ld_b\cos(\theta+\gamma)}}{c} \tag{4.6}$$

$$\tau_b = \frac{(l+d_b)}{c} = \frac{\cos\gamma(h+R) - \sqrt{\cos^2\gamma(h+R)^2 - (h^2+2hR)} + l}{c} \tag{4.7}$$

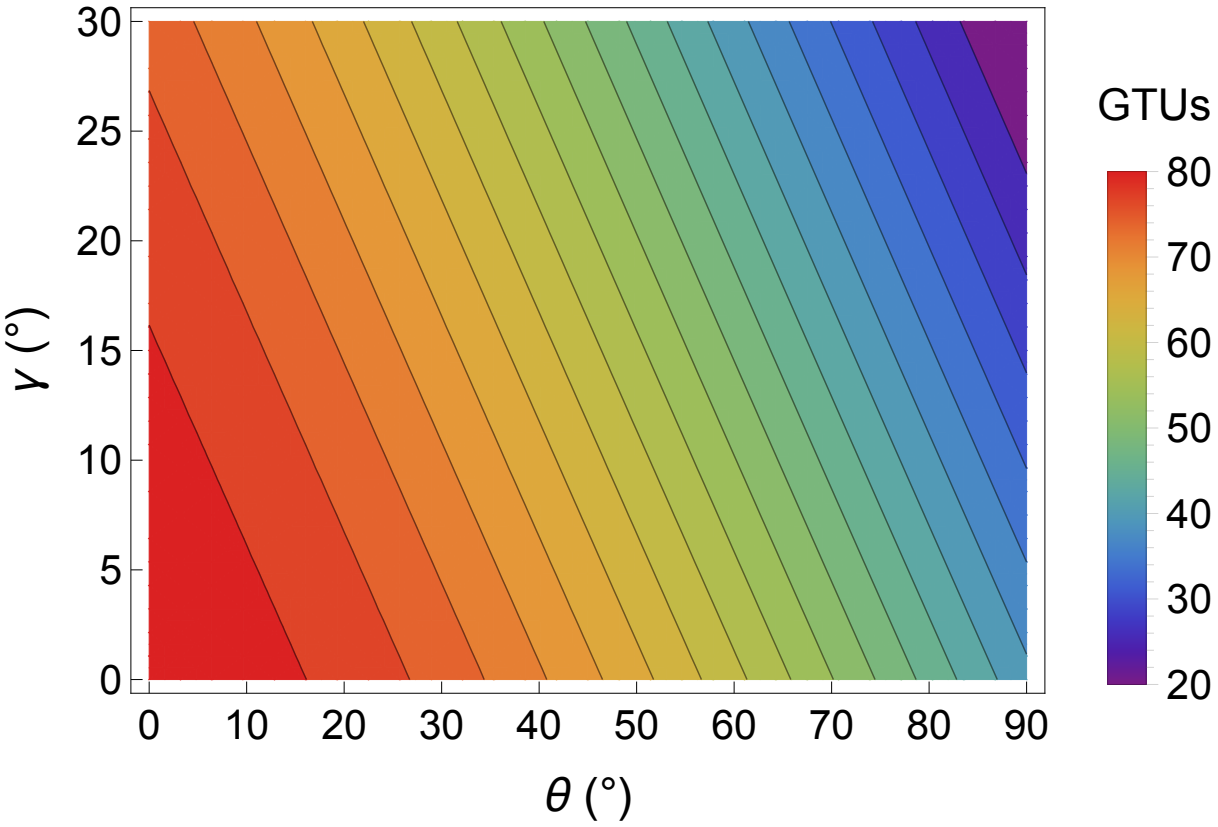

Figure 4.14: Time difference in GTUs ($\tau_b - \tau_a$) in terms of the zenith angle θ and the angular distance γ.

where R is the Earth's radius, d_a is the distance from the emission point of the first photon to the telescope and d_b is the distance between the emission point of the last photon and the telescope.

The arrival time difference $\tau_b - \tau_a$ has been plotted in Figure 4.14. We can point out that, for a given zenith angle, the lower γ, the larger the difference in time is.

Thus, it is proved that the time difference of the EAS light curve depends not only on the arrival direction of the cosmic ray but also on the location of the event in the FoV, given by γ.

4.5.2 Brightness variation

The number of EAS photons detected by a JEM-EUSO pixel which are produced at a certain altitude (we assume ground for simplicity) mainly depends on the number of emitted photons (Υ_{emi}), the optical depth (τ) along the path (d) from the emission point to the telescope, and the solid angle (Ω) subtended by the JEM-EUSO area perpendicular to the line of sight ($A_{JE\perp}$) at the ground, as it is shown in 4.8:

$$\Upsilon_{det} \propto \Upsilon_{emi} \cdot e^{-\tau} \cdot \Omega = \Upsilon_{emi} \cdot e^{-\tau} \cdot \frac{A_{JE\perp}}{4\pi d^2} \tag{4.8}$$

Then, there is a reduction of an image's brightness if the EAS image takes place at the periphery of the FoV instead of at the center, due to these three already mentioned factors:

- distance to the telescope (d_b):

  The distance between the telescope and the photon emission point is: $d_b = (h + R)\cos\gamma - \sqrt{(h+R)^2\cos^2\gamma - (h^2 + 2hR)}$, where h is the JEM-EUSO altitude. If we represent d_b/h in terms of γ, we observe that this ratio increases as a function of the separation angle (Figure 4.15).

- Efficient area of the pixel ($Area_{JE\perp}$):

  JEM-EUSO area perpendicular to the line of sight is: $Area_{JE\perp}$=$Area_{JE} \times \cos\gamma$, corresponding $Area_{JE}$ to the area of the telescope. Since $\cos\gamma < 1$, $Area_{JE\perp}$ is smaller than $Area_{JE}$. This means that when γ increases, the area perpendicular to the line of sight $Area_{JE\perp}$ decreases. However, this effect will be corrected by the JEM-EUSO optics. Actually, due to the optics structure, each pixel observes only in a particular direction.

  From these first two effects we know that when γ increases $Area_{JE\perp}$ decreases and d_b increases. Therefore, the solid angle Ω decreases.

- Atmospheric optical depth along the path (τ):

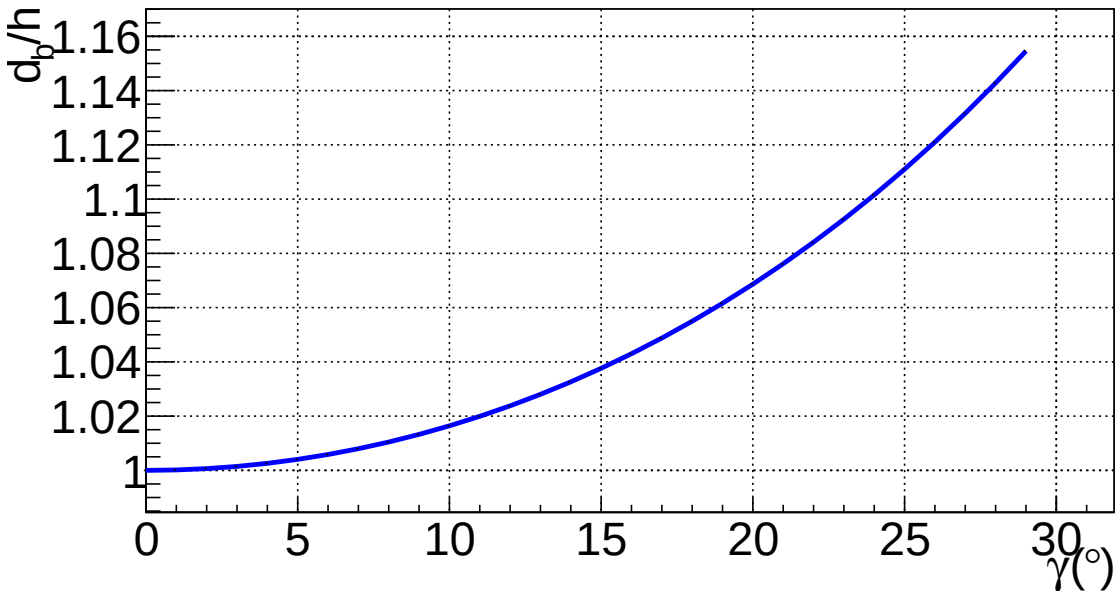

Figure 4.15: Ratio between the distance from ground at an angular distance γ to the telescope and the perpendicular distance from ground to JEM-EUSO as a function of γ. The maximum value of γ corresponds to the one at the limit of the FoV.

Since the optical depth gives a measure of the opacity of a medium, it depends on the light path along this medium. We can express atmospheric (τ) as:

$$\tau = \int_0^L \frac{\rho(l)dl}{\Lambda} \tag{4.9}$$

where Λ is the attenuation length and $\rho(l)$ is the density along the path (L). For an atmosphere without clouds, $\rho(l)$ can be expressed as:

$$\rho(h_i) \simeq \rho_0 \cdot e^{(-h_i/h_0)} \tag{4.10}$$

Being ρ_0 the density at a given altitude h_0, and h_i the altitude of the photon measured perpendicular to the Earth's surface:

$$h_i(l,\gamma) = \sqrt{-2\cos(\gamma)(H+R)(d_b(\gamma)-l) + (d_b(\gamma)-l)^2 + (H+R)^2} - R \tag{4.11}$$

If we represent $\tau(\gamma)/\tau(0)$ in terms of the separation angle (Figure 4.16), we observe that this ratio increases as a function of γ.

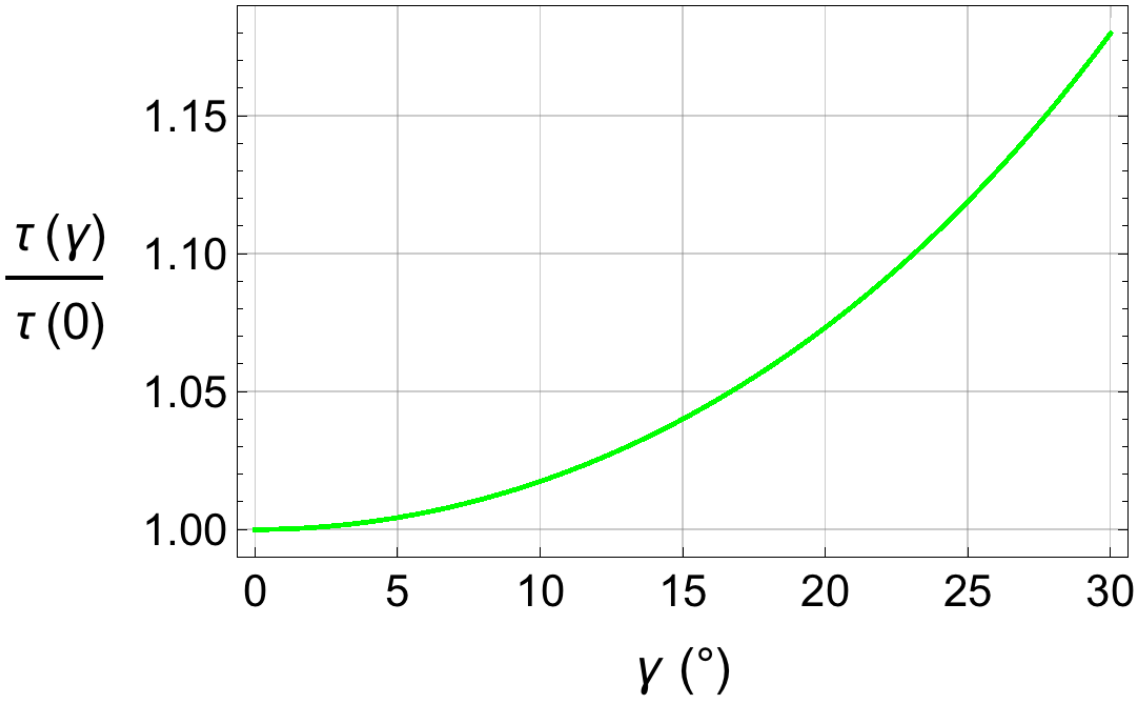

Figure 4.16: Ratio between the attenuation along the photon emission to the telescope, and the attenuation along the perpendicular distance to JEM-EUSO as a function of the angular distance γ. The maximum value of γ corresponds to the one at the limit of the FoV.

Summarizing, the three previously mentioned factors make the EAS detected signal fainter when γ increases. Thus, we prove that the signal at the center of the FoV is brighter than at its edge.

4.5.3 Pixel resolution as a function of the distance

One pixel at the edge of the FS has lower resolution that another at the center. Although both pixels have a size of 3 mm and a spatial resolution of $\delta = 0.075°$, the observation area for the pixel at the edge is higher than that of the pixel at the center. The main reason is that for the one which is at the center, the distance to the ground is lower than for one pixel located at the edge. In Figure 4.17, an ilustration of the observation area

for both pixels is represented.

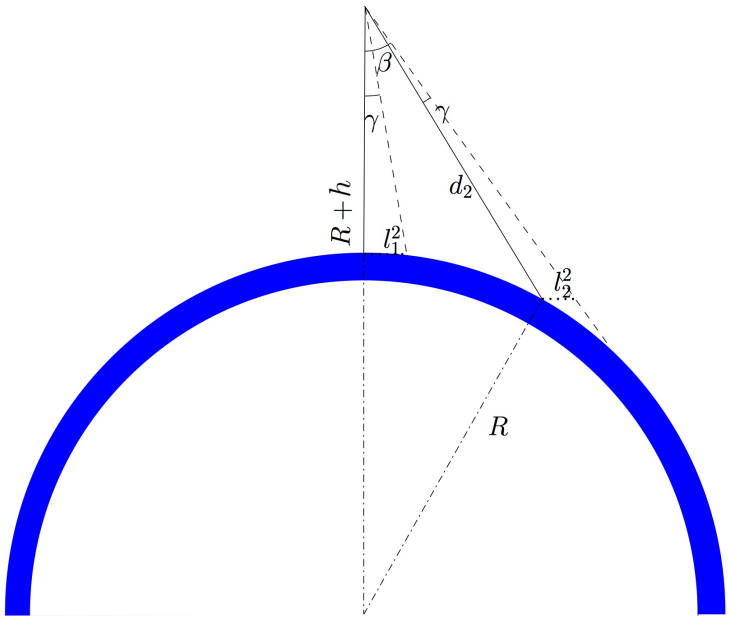

Figure 4.17: Ilustration of the observation area for two pixels; one at the center of the FoV and the other one, at the edge.

The pixel at the center covers an area on ground A_1 corresponding to:

$$A_1 = l_1^2 \tag{4.12}$$

where l_1 is the projection of the pixel size on ground. Since h is the JEM-EUSO altitude, we can roughly estimate l_1 with the altitude of the telescope and the angle subtended by the pixel:

$$l_1 = h \times \sin\delta \tag{4.13}$$

Therefore:

$$A_1 = h^2 \times \sin^2\delta \tag{4.14}$$

On the other hand, a pixel which is located at an angular distance β covers an area on ground A_2 corresponding to:

$$A_2 = l_2^2 \tag{4.15}$$

where l_2 is the projection of this second pixel size on ground. In this case, we need to take into account the angle between the perpendicular to the JEM-EUSO area and the direction of observation of this pixel:

$$l_2 = \frac{d_2 \times \sin\delta}{\cos\beta} = \frac{\left(\cos\gamma(h+R) - \sqrt{\cos^2\gamma(h+R)^2 - (h^2+2hR)}\right) \times \sin\delta}{\cos\beta} \tag{4.16}$$

In Figure 4.18 we represent the ratio between the observation area of a pixel separated at an angular distance γ and the observation area of a pixel located at the center of the FoV, as a function of γ. We observe that the observation area increases with the angular distance γ.

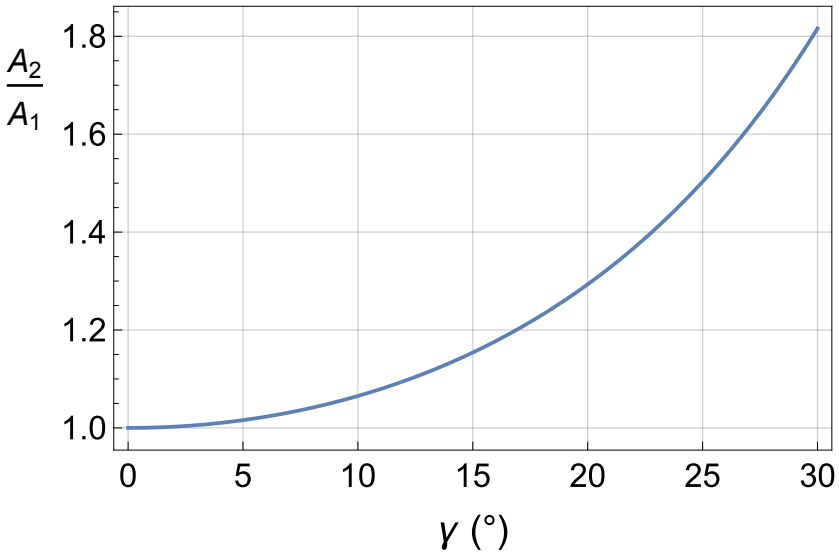

Figure 4.18: Ratio between the observation area of a pixel at an angular distance γ and the observation area of a pixel at the center of the FoV, as a function of γ. The maximum value of γ corresponds to the one at the limit of the FoV.

4.6 Point Spread Function

The Point Spread Function (PSF) describes the two-dimensional distribution of light in the telescope FP for astronomical point sources. In modern large telescopes, a lot of effort

is put into reducing the size of the PSF. With ESAF, we can also study how the PSF looks like due to the JEM-EUSO optics, and its dependence with the light wavelength.

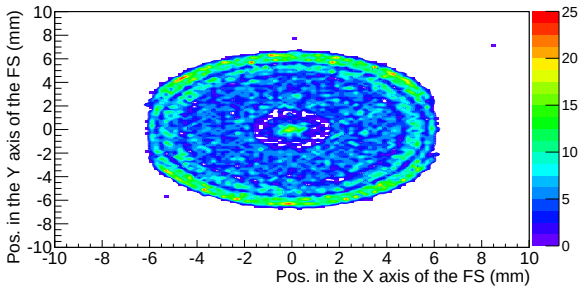

(a) PSF at 300 nm.

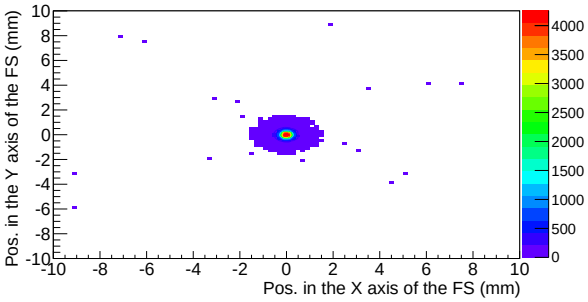

(b) PSF at 350 nm.

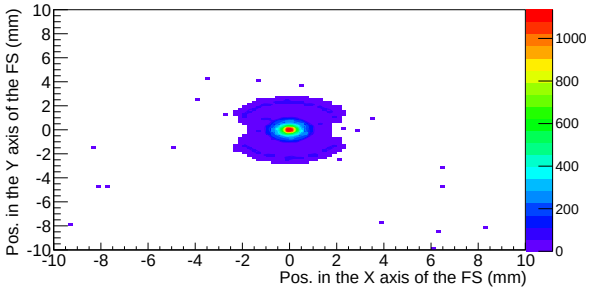

(c) PSF at 400 nm.

Figure 4.19: Point Spread Function produced in JEM-EUSO by light sources emitting at different wavelengths: 300nm, 350nm and 400 nm

In Figure 4.19 the JEM-EUSO PSF is represented for different wavelegths. To show the dependence of the PSF with the wavelength, the same energy (10^{20} eV) and the same location at the FS have been used. The light shadow produced by a puntual source is smaller at 350 nm. Also, for this wavelength there is a higher number of photons concentrated at the center of the FS than for the other two wavelengths. This is due to the optimization of the JEM-EUSO optical system for this wavelegth.

4.7 Reconstruction

After the event signal is recognized, the reconstruction of events will be done down in the Earth. Any direction or energy reconstruction must have as input a set of GTUs per each

pixel. The first necessary step would be the recognition of the signal inside the data sent after trigger. Additionally, at this stage some selection algorithm should be present in order to reject the large amount of fake trigger still keeping the real events. The selection algorithms should therefore prove the ability of rejecting the fake triggers with a certain reliability. Such rejection performance is necessary to guarantee the presence of less than 1 fake reconstructed event over 100 real events [87].

4.7.1 Angular reconstruction

In order to perform any angular reconstruction at least two data are necessary. The first is the already mentioned reconstructed track. The second fundamental one is a map which associates to each pixel a direction in the FoV (called PixelAngleMap in ESAF). The information of the position on the FS, the timing and intensity of the signal are used to approximate the geometrical characteristics of the EAS track.

To disentangle the background from the signal coming from the EAS, the JEM-EUSO instrument has a dedicated trigger technology that filters the relevant information from the whole focal surface. Thus, the instrument keeps only information from pixels that are most likely to contain an EAS signal. The pattern recognition module is resposible of disentangling the signal counts generated by the EAS track from the background. First, the PWISE (Peak and WIndow SEarching technique) module looks at each activated pixel's photon-counts as a function of time. Using this information, it searches for photon-counts that resemble the expected behavior as the moving spot of the EAS shines upon the given pixel. Then, the track finding method makes possible to find a shower track on the focal plane, using the photon-count distribution on the focal plane at each GTU. To optimize the results, the Linear Tracking Trigger Pre-Clustering (LTT-PreClustering) technique can be used to make a pre-selection of the data. It selects the pixels on the FS containing the highest number of counts. Then, it searches for the track that maximizes counts by moving an integration box along a pre-defined set of directions intersecting this point [88].

4.7.2 Energy and X_{max} reconstruction

Once the arrival direction is reconstructed, the geometrical projection on ground of the track can be also determined. Several algorithms have been implemented to reconstruct the altitude of the shower at each step.

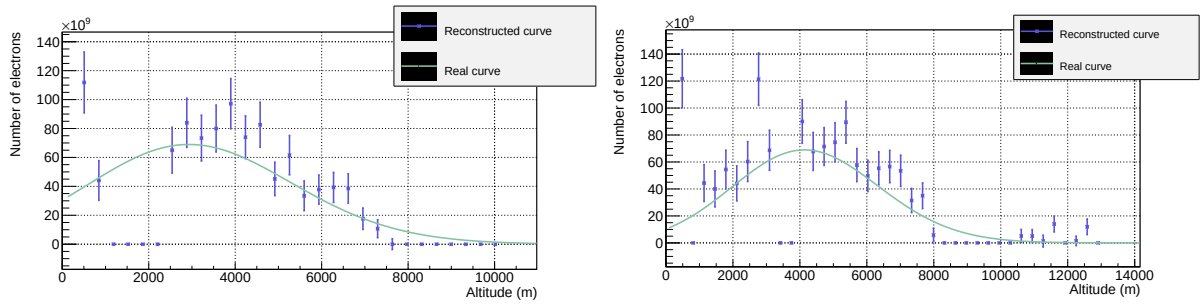

(a) Shower electron curve for $\theta = 30°$

(b) Shower electron curve for $\theta = 45°$

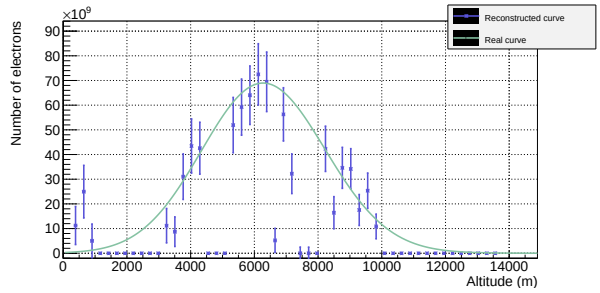

(c) Shower electron curve for $\theta = 60°$

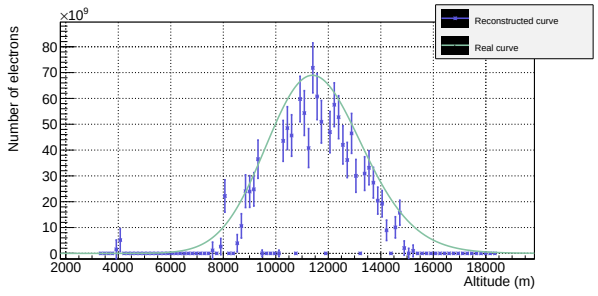

(d) Shower electron curve for $\theta = 75°$

Figure 4.20: The plots represent the shower electron curve for a proton with an energy of 10^{20}eV at different zenith angles. Crosses show the reconstructed electron curve. The black continuous lines corresponds to the simulated (real) event.

Using a parameterization of the atmospheric transmittance and the position of the shower at each time, the shower luminosity is calculated. An estimate of the number of electrons for each step is also made considering the Cherenkov light contamination [87]. The final electron profile is then fitted with a shower parameterization function to obtain the energy and X_{max} parameters. The PmtToShowerReco module receives as input the information on the timing and on the position for all the counts of a triggered event. This is used to reconstruct the total signal intensity as a function of time (counts curve). The

maximum and the Cherenkov peak in the reconstructed counts curve are identified. The number of detected photo-electron as a function of time is converted into the number of photons hitting on the FS. The PmtToShowerReco module, developed in [87] is the one used for this thesis. It mainly uses two methods for energy and shower maximum reconstruction: with or without recognition of the Cherenkov bump. They will be more deeply explained in Chapter 6. In Figure 4.20 both real and the reconstructed curves are shown for four shower electrons curve for a proton with an energy of 10^{20}eV at different zenith angles (30°, 45°, 60° and 75°).

Chapter 5

EAS propagation in cloudy conditions

The accuracy in the determination of air shower parameters such as the longitudinal profile or the primary energy are strongly dependent on atmospheric conditions such as temperature, pressure and humidity. These parameters may alter the development and, in particular, the detection of extensive air showers. In this section we discuss how EAS fluorescence and Cherenkov light from UHECRs are affected by a particular atmospheric condition: the presence of clouds. We also calculate the trigger efficiency in cloudy conditions, which is very important for the estimation of the JEM-EUSO duty cycle or the effective aperture of the instrument (exposure), as some contaminated events are excluded from the analysis. Moreover, a rough energy and arrival direction estimation for different cases with presence of clouds is presented. Until now, the cloud modelling used in ESAF consisted of an uniform, homogeneus layer of a particular optical depth (τ_c), physical thickness and cloud top height (H_c). In this section, a simple model of fluorescence and Cherenkov light propagation in 3D clouds is introduced.

5.1 Atmospheric radiative transfer: emission, absorption and scattering

When the scale of a system is much larger than the wavelength of radiation, this radiation can be considered to travel in straight lines in homogeneous media. Radiative transfer is the energy transfer in the form of electromagnetic radiation. The propagation of radiation through a medium is affected by absorption, emission, and scattering processes [89].

The equation of radiative transfer describes these interactions mathematically. Although analytic solutions to the Radiative Transfer Equation (RTE) exist only for simple cases, there are two approaches to the solution. One involves the solution of an integral equation for the source function, while the other deals directly with the differential equation of transfer. Both are widely used [90].

The medium where the light is being propagated can also generate photons. This emission of radiation can be described by the Kirchhoff's law, which states that the emissive power of a body only depends on its temperature for a given wavelength [91]. Kirchhoff's law conceives that the ratio of emissivity, ϵ, to absorptivity, α, of all bodies can be described by an universal function, f, common to all radiation within enclosures, as is espressed in [92]:

$$\frac{\epsilon}{\alpha} = f(\lambda, T) \tag{5.1}$$

In thermal equilibrium the emissivity is equal to the absorptivity. If the medium can be considered as a blackbody, we could apply the Planck's distribution; for a body at temperature T, the emitted radiance at a wavelength λ is given by:

$$B_\lambda(T) = \frac{2hc^2}{\lambda^5} \frac{1}{e^{\frac{ch}{\lambda k_B T}} - 1} \tag{5.2}$$

where k_B is the Boltzmann's constant [93].

A fraction of the incident radiation is lost along the path of propagation in the medium. The Beer-Lambert's law governs this reduction in the radiation intensity I_λ at a wavelength λ. This law relates the absorption of light to the properties of the medium. Unlike emission, the amount of absorption occuring in a medium depends on the intensity of the

incident radiation. Absorption coefficient, α_λ, (inverse distance) is the rate at which the fraction of the total intensity (i.e. dI_λ/I_λ) decreases per unit distance along the ray path (ds) at a given wavelength as shown in:

$$dI_\lambda = -\alpha_\lambda(s) I_\lambda ds \Rightarrow \frac{I_{\lambda 2}}{I_{\lambda 1}} = e^{-\int \alpha_\lambda(s) ds} \tag{5.3}$$

where $I_{\lambda 2}$ and $I_{\lambda 1}$ are the intensities at two different points along the paths. In the UV range of interest, absorption is mainly due to ozone.

Moreover, both fluorescence and Cherenkov light are affected by scattering (such as Rayleigh or Mie scattering) due to the atmospheric particles. Rayleigh scattering is produced by the air molecules, is strongly wavelength dependent and it slightly depends on humidity, temperature and pressure. When the diameter of the targets is of the order of the radiation wavelength, Mie scattering takes place. Aerosols (dust, smoke, ...) in atmosphere and droplets (clouds) are responsible for Mie scattering of light [24]. The difference between water and ice crystal clouds have one important difference: the number density of scatterers. The density of water molecules in a low level cloud is 10-100 times greater than that of ice crystals in a high altitude cirrus cloud. As a consequence, a much smaller scattering length for the low level cloud is produced. Also, the relation between the cloud optical depth and its physical thickness becomes qualitatively different. Depending on the values of optical depth and physical thickness of the cloud, the effect of multiple scattering inside the cloud becomes significant [94]. Isotropic (elastic or monochromatic) scattering occurs when the total amount of radiation emitted per unit frequency range is equal to the total amount absorbed in that same frequency range. EAS photons that are not emitted in the direction of the detector may be scattered later in this direction. The phase function $P(\theta)$ is the angular distribution of light intensity scattered by a particle at a given wavelength. It is given at an angle θ which is relative to the incident beam. $P(\theta)$ can be thought of as a probability density function, showing the chances of a light photon being scattered in a particular direction, θ [95]. For Rayleigh scattering, the phase function can be written in terms of the scattering angle as [96]:

$$P_{ray}(\theta) = \frac{3}{4}(1 + \cos^2(\theta)) \tag{5.4}$$

where θ is the angle between the propagation direction and the scattering direction at the moment of the scattering process. Normalized to the zenith angle: $P_{Nray}(\theta) = \frac{3}{8\cdot\pi}(1 + \cos^2(\theta))$.

It is often convenient to have an analytic formula that approximates the shape of an actual complex phase function (this is the case for the Mie scattering). Henyey and Greenstein introduced a function which, by the variation of one parameter (the assymetry factor), -1$\leq g \leq$1, the ratio between the backscattering and the forward scattering can be modeled [97]. The Henyey-Greenstein function is:

$$P_{HG}(\theta) = \frac{1}{4\pi}\frac{1-g^2}{(1+g^2-2g\cos\theta)^{3/2}} \tag{5.5}$$

5.2 EAS in clear sky and in cloudy conditions using ESAF

Since JEM-EUSO will have a wide FoV, different atmospheric conditions will take place in the observation area at the same time. We have discussed how differences in atmospheric conditions such as temperature, pressure or humidity might affect the shower development. Also, the amount of clouds (fractional cover) and the distribution of clouds in terms of H_c and τ_c will undoubtedly affect the detectors trigger aperture. As an example of a cloud effect, the reflectivity of an optically opaque cloud is 80-90%, several times larger than that of the surface of the ocean, which is 10-20% [94]. Here we want to focus on how the different types of clouds will affect the light curves of the EAS.

To include clouds in ESAF, there are two different options in its atmospheric model: with TOVS (TIROS Operational Vertical Sounder) database or as an uniform and homogeneous layer (called test cloud) whose physical parameters are τ_c, H_c and its physical thickness. We have selected the second option for our work.

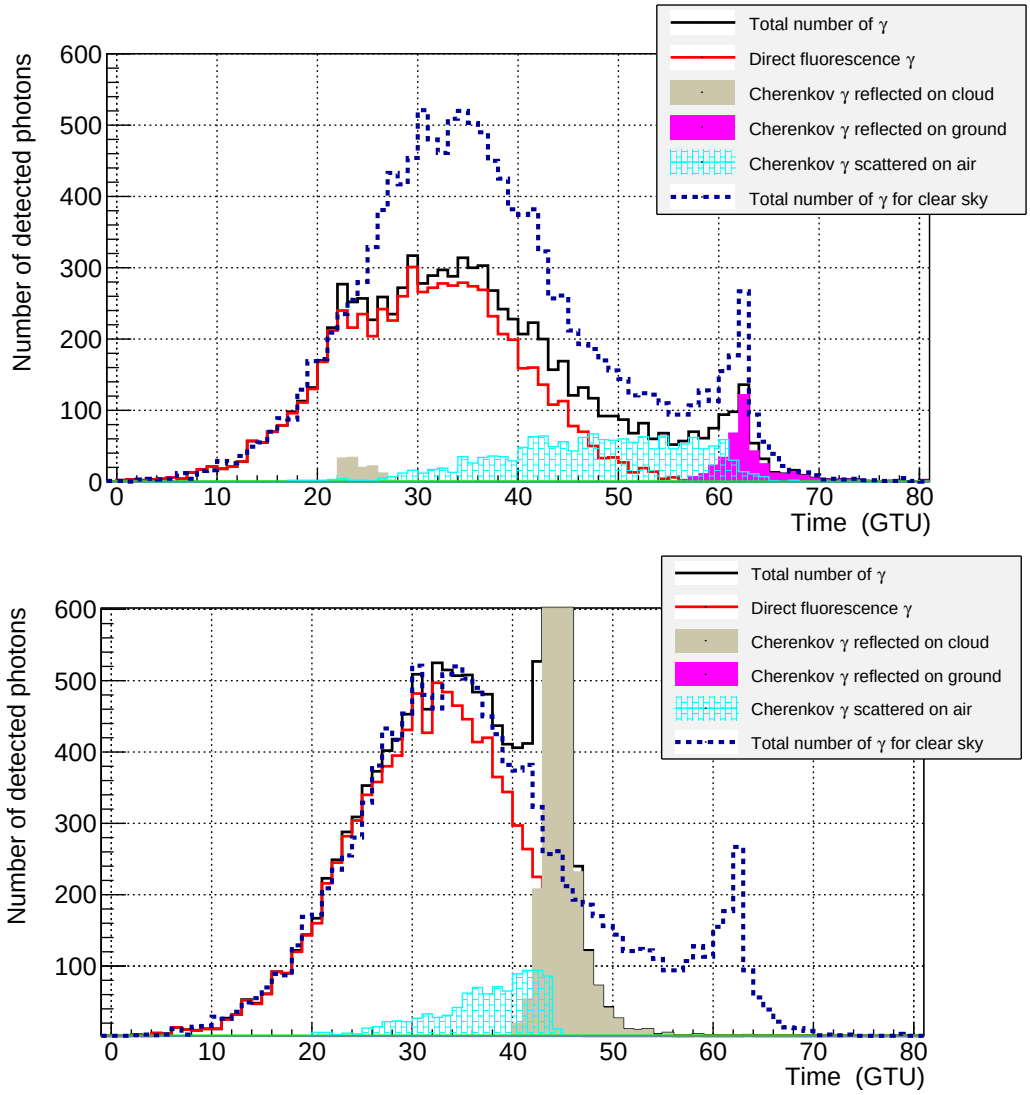

Figure 5.1: Light curves for a standard UHECR ($\theta = 60°$ and $E = 10^{20}$ eV) under two different cloudy conditions: in presence of a high and optically thin cloud (upper panel) and in presence of a low and optically thick cloud (lower panel). In both cases the light curves are compared with the one we would obtain in a cloud-free atmosphere.

As an example of how clouds influence EAS detection, in Figure 5.1 it is represented the same shower simulation (a proton EAS with a zenith angle of 60° and an energy of 10^{20} eV) for two cloudy cases: in presence of a high and optically thin cloud and in presence of a low and optically thick cloud. Both are compared with the light curve for

the free cloud atmosphere case. The X axis shows the Gate Time Units (1 GTU = 2.5μs) and the Y axis, the number of detected photons. The coloured lines present the total number of detected photons for a clear atmosphere case (blue line), the total number of detected photons for the cloudy case (black line), the number of fluorescence photons directly emitted to the telescope (red line), the Cherenkov photons reflected on the top of the cloud (grey area), the Cherenkov photons reflected on ground (magenta area), and the Cherenkov photons scattered on air (dashed light blue area).

We observe how the shower is produced in the presence of an optically thin cloud (like the upper panel of Figure 5.1); the signal suffers slight absorption after the cloud, although the signal is still well visible. Also, the Cherenkov signal reflected on ground is still observed. For these cases where an optically thin cloud is present in the JEM-EUSO FoV, we may at least mark such event as rejected or give a lower limit energy estimation of the UHECR event. Moreover, the apparent EAS track is not affected by the clouds and therefore the angular reconstruction is still possible for these cloudy scenarios. For optically intermediate clouds, we may identify two main Cherenkov contributions. One is the Cherenkov light reflected on the top of the cloud. The other, since these clouds are not optically thick enough to truncate the signal below the cloud, is the Cherenkov component reflected on Earth's surface.

Clouds with large τ_c produce a very high scattered Cherenkov peak. If the cloud is low enough (like the lower panel of Figure 5.1), the detected signal is similar or even better than that for the clear sky case. The reason is that directed fluorescence signal is not affected by the cloud (because the shower will develop above the cloud), but the Cherenkov peak produces a more clear signal (we have already commented above that the reflectivity for an opaque cloud is a few times larger than for ground). However, the EAS signal which develops after the cloud will be lost and the shower development cannot be enterely observed. These optically thick clouds, as long as the maximum development of EAS is located above the cloud, may even have a positive effect as it ensures us a bright Cherenkov reflected light from the top of such a cloud. With a reasonable accuracy, this gives the location of a point of the shower track that helps to reconstruct geometrical and

physical parameters of the EAS [73].

Photons emitted in the direction of the telescope at altitudes higher than H_c are only affected by the atmospheric τ from the emission point to the detector. On the other hand, photons emitted in the JEM-EUSO direction below H_c will also suffer an attenuation according to τ_c as expressed in [6]:

$$At = \int e^{-\tau(s)} ds \tag{5.6}$$

where $\tau(s)$ is the optical depth along the path s. This fact can be understood thanks to Figure 5.2

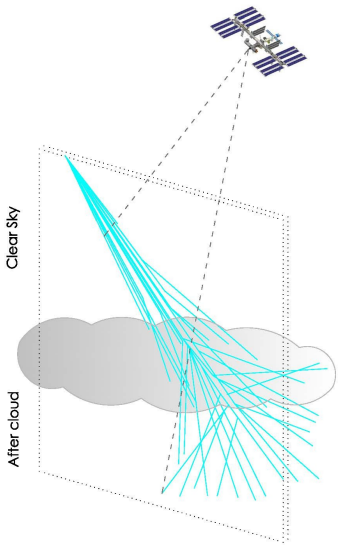

Figure 5.2: Light emitted from the shower to the telescope in the presence of clouds

Since EAS with different inclinations develop at different altitudes in the atmosphere, they are not equally affected by the same clouds. For example, the shower maximum of an EAS with a zenith angle of $\sim 30°$ develops at an altitude of around 3 km. This means that clouds with H_c higher than 3 km will strongly affect this shower. Less inclined showers,

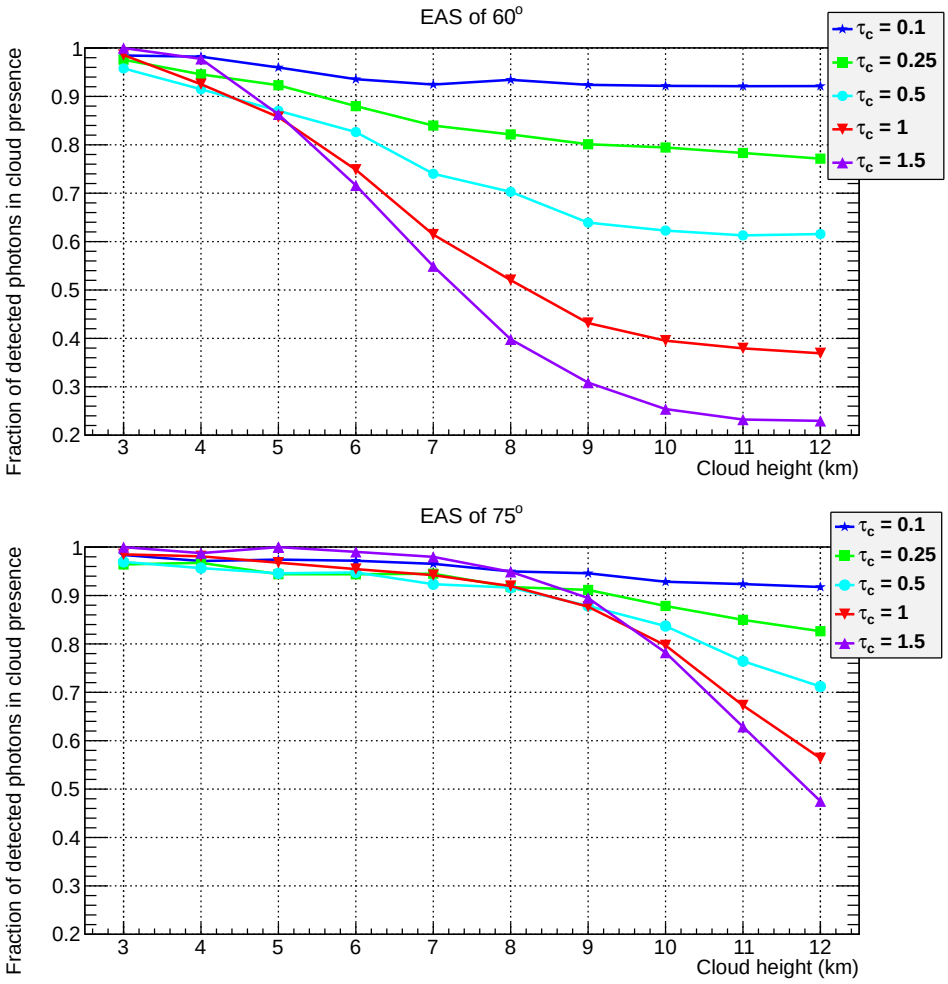

Figure 5.3: Fraction of detectable photons in different clouds scenarios compared with clear atmosphere, as a function of H_c along different τ_c denoted by different symbols. Top and bottom panels indicate the cases of $\theta = 60°$ and $\theta = 75°$, respectively. We observe how the attenuation is more pronounced as H_c is higher. Also, this attenuation has more impact in more vertical showers.

on the other hand, develop higher in the atmosphere and there will not be affected by low clouds. Figure 5.3 represents the attenuation of photons in different cloudy scenarios compared with clear atmosphere as a function of H_c to that of clear atmosphere for two showers: 60° and 75°. Different τ_c are denoted by different symbols. We observe that, as H_c increases, the influence of the cloud is more pronounced. Also, for the 60° shower, the

influence of intermediate-high clouds (7-8 km) is more significant than for the 75° shower due to the altitude at which the shower develops. Showers originated from different types of primary particles are affected by H_c in different ways. For example, neutrino-induced showers will develop much deeper in the atmosphere than showers induced by protons in the same inclination and with the same energy.

5.3 Trigger efficiency in cloudy conditions

To quantify the effect of cloud contamination, it is needed a study of the climatological distribution of clouds, regarding its H_c, τ_c, and geographical location. In [2], databases such as TOVS, CACOLO and ISCCP have been used. For TOVS, the occurrence of clouds according to their H_c and τ_c is summarized in Figure 5.4 [2].

Clouds whose $\tau_c < 0.1$ can be considered clear atmosphere and occurs $\sim 30\%$ of the time. Also, clouds below 3 km do not difficult the measurements (except for vertical showers that are, anyway, difficult to trigger) since the shower maximum develops at higher altitudes. This case account for $\sim 30\%$ too. Therefore, we can assume that $\sim 60\%$ of the time the shower detection is produced in clear atmosphere.

To investigate clouds impact in the overall observation efficiency by the JEM-EUSO Space Mission, we define "cloud efficiency" $\zeta(E, H_c, \tau_c)$ as follows [6]:

$$\zeta(E, H_c, \tau_c) = \frac{A(E, H_c, \tau_c)}{A(E, clear\ atm)} \tag{5.7}$$

being $A(E, H_c, \tau_c)$ the geometrical trigger aperture as a function of energy E, H_c and τ_c. The numerator and denominator are those of cloudy and clear atmosphere conditions, respectively. The aperture for each case with a certain atmospheric condition is defined as:

$$A(E) = \frac{N_{trig}}{N_{total}} \cdot S_0 \cdot \Omega_0 \tag{5.8}$$

where N_{trig} is the number of triggered EAS, N_{total} is the total number of considered EAS, S_0 is the area where the considered showers have taken place, and Ω_0 is the solid angle.

Cloud-top altitude H_C	Optical depth τ_C			
	<0.1	0.1–1	1–2	> 2
	All data			
> 10 km	1.2%	5.0%	2.5%	5.0%
6.5–10 km	< 0.1%	3.2%	4.2%	8.5%
3.2–6.5 km	< 0.1%	2.0%	3.0%	6.0%
< 3.2 km	31%	6.4%	6.0%	16%

Clear atmosphere

~ clear atmosphere

Observable with reduced signals

Observable for high ZA

Hardly observable

Figure 5.4: Occurrence (%) of clouds between 50° N and 50° S latitudes on TOVS database in the matrix of cloud-top altitude vs optical depth [2].

The average values of $\zeta(E, H_c, \tau_c)$ for showers simulated with energies higher than $10^{19.8}$ eV are summarized in Table 5.3, for the sixteen test clouds considered above for the TOVS classification.

Optically thin clouds (defined as $\tau_c < 1$) attenuate the EAS signal only by a factor of $e^{-\tau_c}$. Therefore, their influence in the trigger efficiency is not significant. Optically thick clouds (defined as $\tau_c > 1$) significantly absorb the EAS signal originated below the cloud. This means that the number of photons emitted in the direction of the JEM-EUSO telescope above the cloud need to activate the trigger. Then, the trigger efficiency in these cases depends on H_c and the zenith angle of the shower. High clouds may affect most EAS, lowering JEM-EUSO trigger efficiency, while clouds at intermediate altitudes (for instance, at $\sim$ 5 km) only affect less inclined showers. If the optically thick cloud is low enough, trigger efficiency is not affected because most part of the EAS develops above the cloud top height [6].

To properly infer the UHECR physical parameters, the EAS maximum development and the geometrical parameters of the shower have to be inferred. To do so, we estimate a priori selection which includes: clear atmosphere, optically thin clouds ($\tau < 1$) and clouds whose H_c is lower than the altitude of the EAS depth of maximum development, independently of its τ_c. The reason is that thin clouds affect the energy estimation but

	H_c			
τ_c	2.5 km	5 km	7.5 km	10 km
5	90%	70%	26%	18%
1.5	89%	74%	43%	37%
0.5	89%	82%	69%	66%
0.05	90%	88%	89%	88%

Table 5.1: Average cloud impact for sixteen different type of clouds for protons primary energy above $10^{19.8}$ eV.

still the angular reconstruction is feasible because, even if the signal suffers a certain absorption, the shower track and the arrival time will not be modified. Optically thick clouds located below the shower maximum truncates the signal after the shower maximum and, therefore, enough shower track is detected to apply the reconstruction algorithms.

Figure 5.5 shows the cloud efficiency as a function of the proton primary energy for all triggered event by circles, and for the "maximum development visibility" selection, (i.e., $\tau_c < 1$ or $H_{max} > H_c$) by triangles. We consider the cloud occurrence by the previously mentioned TOVS database to estimate the overall effect. The error bar shown represents the error due to the different statistical and systematic uncertainties in the procedure [6]. In the X axis, the proton energy is represented. From the Figure 5.5 we conclude that triggered events occurs at least $\sim 80\%$ of the time. The fraction of events that fulfill the "maximum development visibility" requirements over the ones triggering in clear sky conditions (the reference case) is almost constant at higher energies. We name this quantity "cloud efficiency" (κ_c), and it accounts for $\sim 72\%$ of the trigger EAS above $\sim 3 \times 10^{19}$ eV. It is important to stress that the shower maximum height dependence is much more dominated by the zenith angle than by the energy of the primary particle.

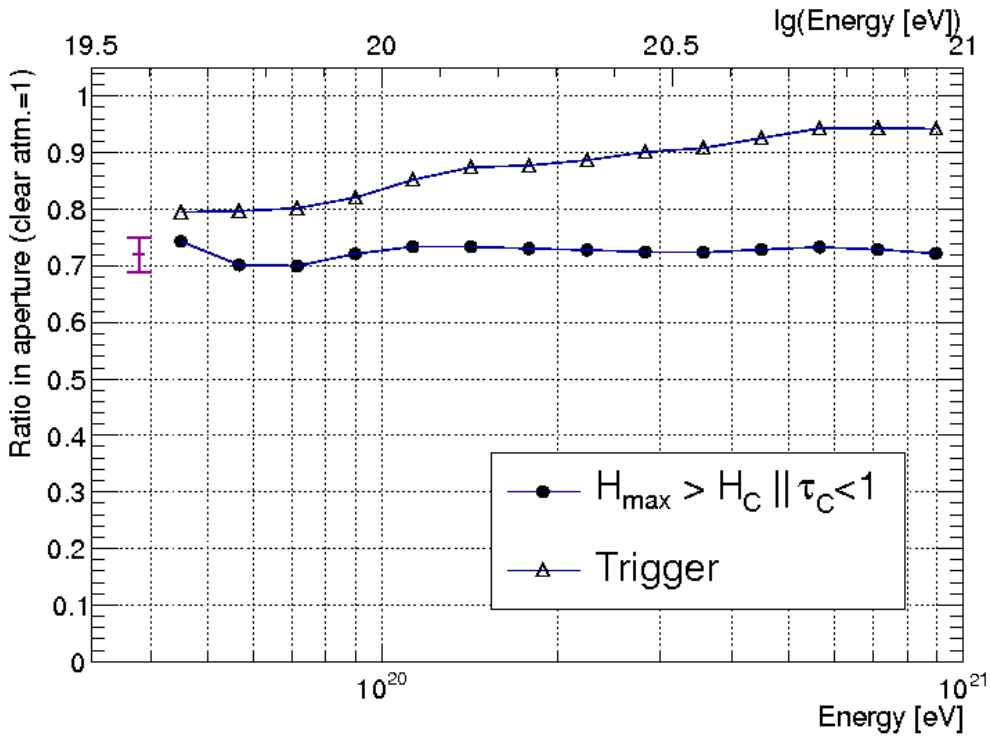

Figure 5.5: Cloud efficiency as a function of the energy for all triggered event by circles, and for the "maximum development visibility" selection, (i.e., $\tau_c < 1$ or $H_{max} > H_c$) by triangles. Cloud occurrence has been taken into account.

5.4 Shower geometry in cloudy conditions

To analyze the direction of the incoming shower, it can be understood as the composition of two projections: the azimuthal angle (ϕ) and the zenith angle (θ). The azimuthal angle is contained in the FP, while the zenith angle is contained in the Track Detector Plane (TDP), which is the plane that includes the shower track and the detector. The former angle is calculated with the projection of the image of the shower in the FS. The latter, from the timing information and arrival angle of the EAS photons to the detector. The zenith angle can be obtained by fitting the arrival time method from Section 4.5.1. For simplicity, we will consider for this exercise that $d_b = \frac{h}{\cos(\gamma)}$ (see Figure 5.6) [98].

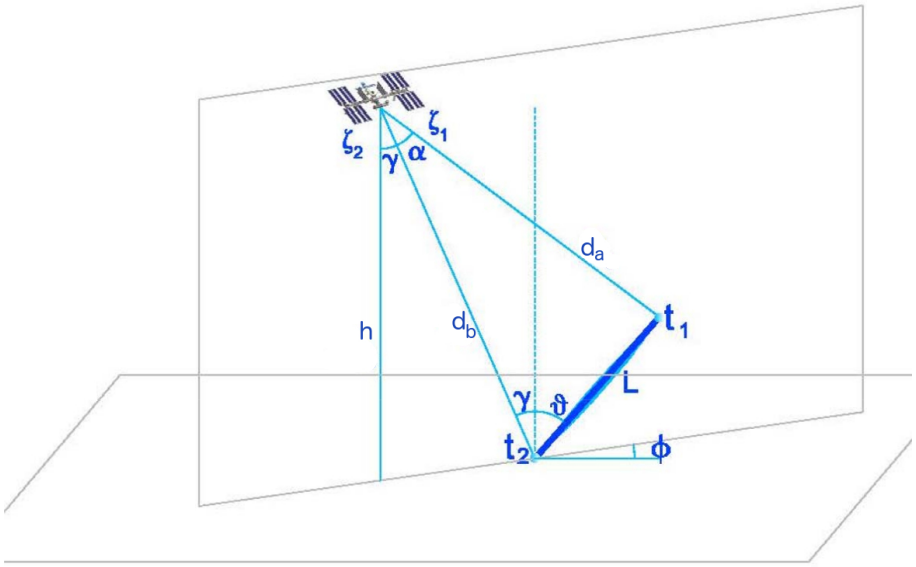

Figure 5.6: Scheme of the EAS geometrical relations for JEM-EUSO.

Then, the relation between the time and the zenith angle will be given by:

$$\tau_1 - \tau_2 \;=\; \frac{1}{c} \cdot \frac{h}{\cos\gamma} \cdot \left(1 + \frac{\sin\alpha - \sin(\gamma+\theta)}{\sin(\alpha+\gamma+\theta)}\right) \tag{5.9}$$

where α is the viewing angle for each detected photon (its angular distance from the EAS core), and γ is the angular distance between the shower core and the center of the FoV. For showers landing on the center of the FoV (this is, γ=0), this equation is simplified to:

$$\tau_1 - \tau_2 = \frac{h}{c} \cdot \left(1 + \frac{\sin\alpha - \sin\theta}{\sin(\alpha+\theta)}\right) \tag{5.10}$$

In Figure 5.7 it has been represented the viewing angle as a function of the arrival time for a proton EAS, with $\theta = 60°$ and $\phi = 45°$ landing on the center of the FoV in three different cases: in clear atmosphere (upper panel), in presence of an optically thin cloud (intermediate panel), and in presence of an optically thick cloud whose top cloud is slightly below the shower maximum (lower panel). The signal has been fitted with the equation (5.10). For the three cases, the slope of the track changes when the photons

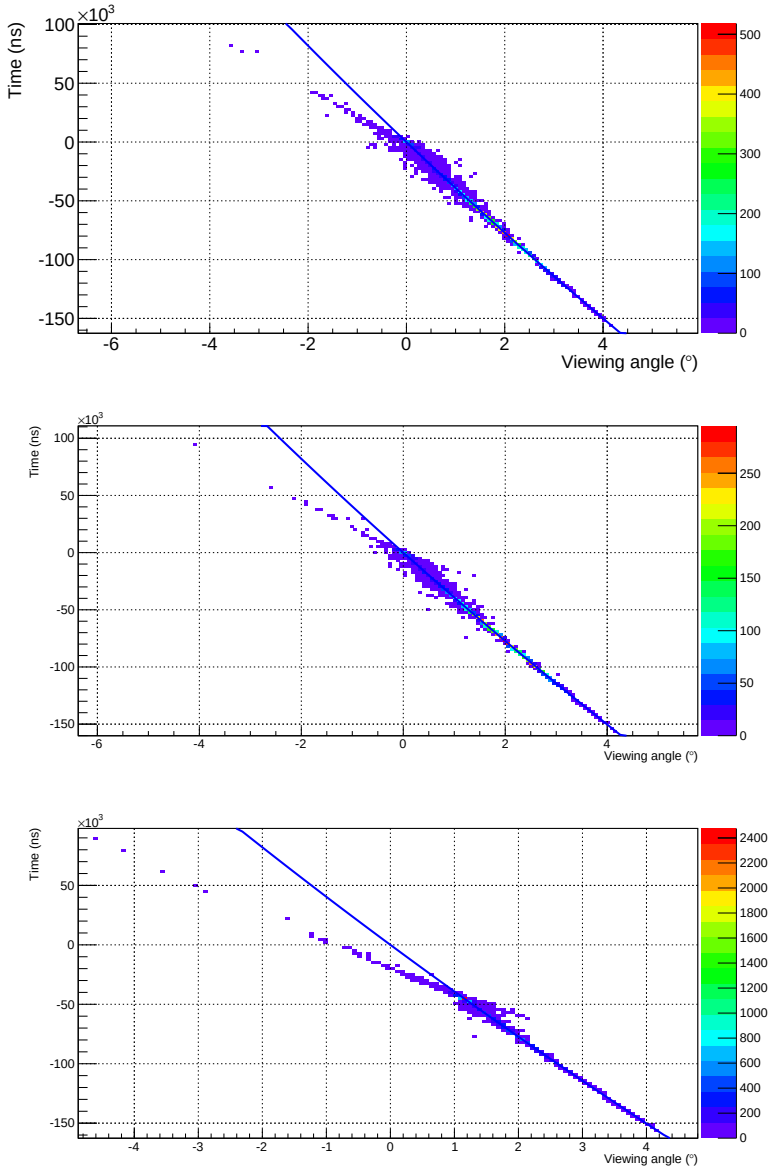

Figure 5.7: Viewing angle as a function of time for three different cases landing on the center of the FoV: in clear atmosphere (upper panel), in presence of an optically thin cloud (intermediate panel), and in presence of an optically thick cloud (lower panel). The color scale represents the number of detected photons. The continuous line represents the fitted equation (5.10). The photons corresponding to negative viewing angles are those that have been reflected either on ground or on the cloud top.

arriving to the telescope are those which have been reflected either on ground or on the cloud surface. For the optically thin cloud case, even if some few photons have been scattered due to the cloud and their trajectory has changed, the track of the shower is still well defined. On the other hand, in the case of the optically thick cloud the signal after the cloud has been lost. However, a good fit can be achieved with the part of the signal from above the cloud.

In Figure 5.8 the projection of the shower track in the focal plane has been represented. To obtain the value of the azimuthal angle (ϕ), one needs to calculate the arctangent of the slope of this projection. Therefore, we can plot a theoretical model as the continuous line in Figure 5.8, which represents $\theta \cdot \sin(\phi)$ in terms of $\theta \cdot \cos(\phi)$. As well as before, for the optically thin cloud case (intermediate panel), even if some few photons have been scattered, shower track projection is still well defined. On the other hand, in the case of the optically thick cloud (lower panel) the signal after the cloud has vanished. However, a good fit can be achieved with projection of the signal from above the cloud. From the results presented above, we can assume than angular reconstruction (θ and ϕ reconstruction) is feasible in the previously called "maximum development visibility" cases. Although here only one particular arrival direction has been presented, the "maximum development visibility" cases would present enough signal to activate the JEM-EUSO trigger, and therefore enough shower track to apply the already presented study.

Nevertheless, in presence of optically thick clouds the angular resolution gets worse. Since the signal after the cloud is totally lost, the EAS shower track will be shortened, and therefore the angular resolution for an EAS in presence of an optically thick cloud will be equivalent to that of an EAS in clear atmosphere with a lower zenith angle. On the other hand, the apparent movement of an EAS in presence of an optically thin cloud will not be significantly modified, since the length of the shower track and its timing does not vary. Therefore, the angular resolution will be similar to that of the same EAS in presence of clear atmosphere. For instance, in clear atmosphere conditions (upper plot of the lower panel in Figure 5.4) the $\theta = 60^\circ$ EAS extends $\sim 3^\circ$ and lasts ~ 60 GTUs (=150 μs). The same EAS in presence of an optically thick cloud at 3 km (intermediate

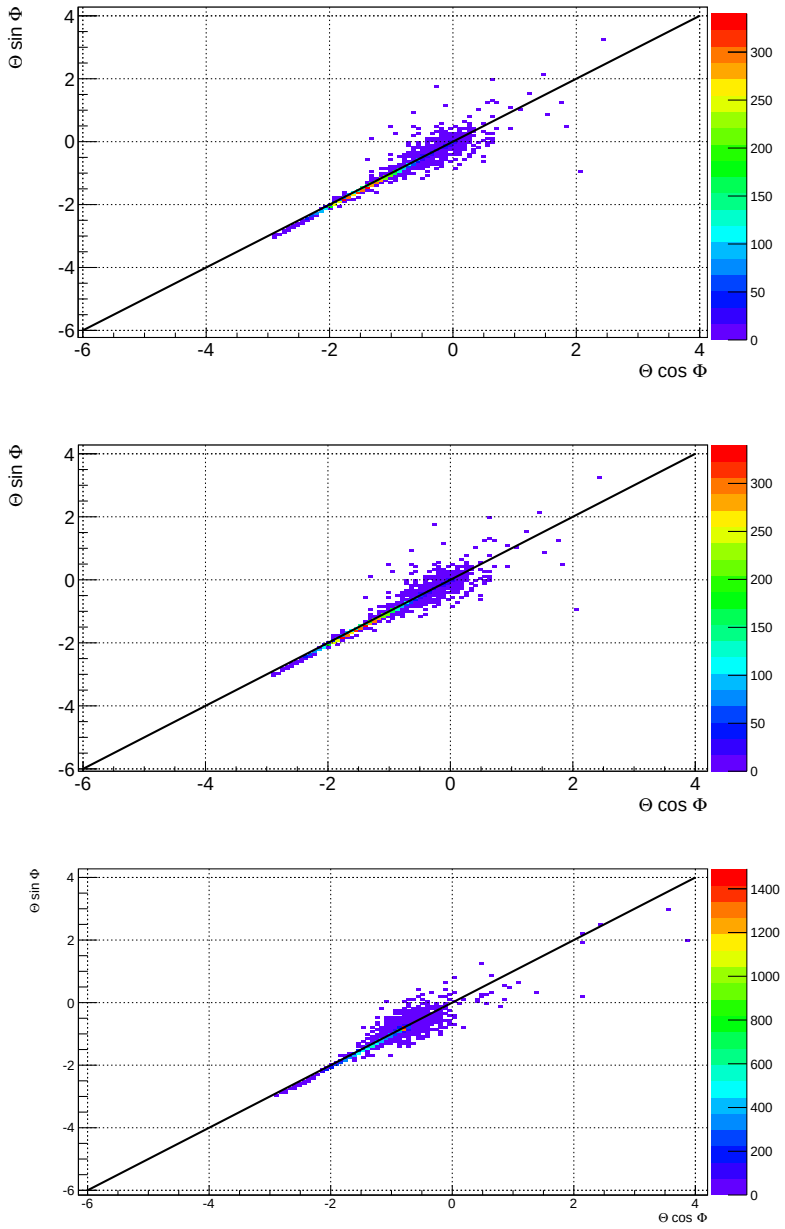

Figure 5.8: EAS projection on the FP of the three previous cases: in clear atmosphere (upper, left panel), in presence of an optically thin cloud (upper, right panel), and in presence of an optically thick cloud (lower panel). The color scale represents the number of detected photons. The continuous line represents $\theta \cdot \sin(\phi)$ in terms of $\theta \cdot \cos(\phi)$.

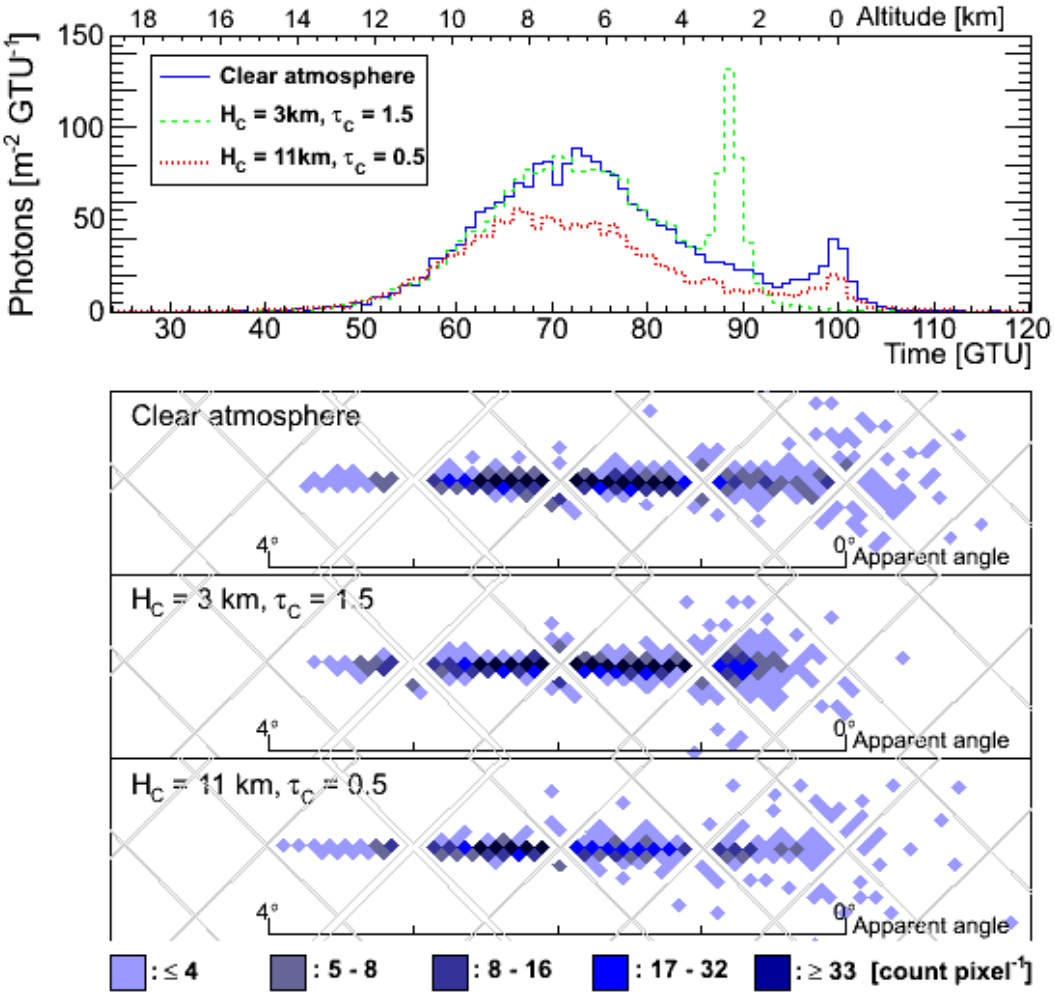

Figure 5.9: Arrival time distribution of photons (top panel) from a typical proton EAS of $E_0 = 10^{20}$ eV and $\theta = 60°$ for different atmospheric conditions. The solid line represents the case for clear atmosphere. Dashed and dotted lines denote the cloudy cases for $\tau_c = 1.5$ at $H_c = 3$ km and $\tau_c = 0.5$ at $H_c = 10$ km, respectively. The axis on the top indicates the altitude along the EAS axis where photons originate to arrive given time. Bottom panels show the time-integrated images of signals on the FS detector for those three cases. The color scale indicates the number of signal counts per pixel. The horizontal position along the EAS track axis corresponds to the arrival time on the top panel [99].

plot of the lower panel in Figure 5.4), only extends $\sim 2^{\circ}$ and lasts 40 GTUs. Thus, we can claim that the resolution for an EAS in presence of an optically thick cloud will be equivalent to that of a more vertical EAS in clear atmosphere [88]. On the other hand, the apparent movement of an EAS in presence of an optically thin cloud (lower plot of the lower panel in Figure 5.4) is not significantly modified. Therefore, the angular resolution will be similar to that of the same EAS in presence of clear atmosphere.

5.5 Estimation of the energy reconstruction in cloudy conditions

The isotropically emitted UV fluorescence light from EAS is proportional to the energy deposited in the Earth's atmosphere and can be used to perform a measurement of the air shower energy [100]. In order to understand how the energy estimation of the UHECR can be affected by a cloud, we analyze the amount of fluorescence photons detected by JEM-EUSO as a function of time under different cloud conditions. To compare among these different conditions, the same EAS have been simulated for the sixteen different cloudy cases represented in the cloud occurence in Figure 5.4. Around 10^5 simulations have been performed under 17 conditions (16 cloudy cases and 1 clear atmosphere case). For each EAS, the light curve has been fitted to a gaussian function, and the integral of these functions have been calculated. This integral is proportional to the estimated energy of the cosmic ray. Therefore, comparing the integral of a certain EAS in clear atmosphere with the integral of each of their sixteen corresponding cloudy cases, we can figure out how the energy estimation is affected by clouds. To fit the light curve to a gaussian function, two different approaches have been considered, depending on the optical depth of the involved cloud:

- if the cloud has a $\tau_c > 1$, the light curve is fitted using the signal detected before the cloud. Then, this gaussian fit is extrapolated up to the ground.
- If the cloud has a $\tau_c < 1$, we fit the signal as it is detected.

In Figure 5.10 an EAS is fitted with this method for the sixteen cases of clouds. Since the effect of clouds depend on the shower inclination, for this study three different groups of showers, according to their arrival direction, have been considered (i.e., $\theta < 30°$, $30° < \theta < 60°$, $60° < \theta < 90°$). For the three ranges of θ, we classify the sixteen cloud cases as follows:

- green case: the maximum of the shower is located above H_c.
- Yellow case: the cloud has an intermediate τ_c, and H_c is above the shower maximum.
- Red case: the shower maximum takes place after H_c and the cloud has a $\tau_c > 1$.

The results are summarized in tables 5.2, 5.3, 5.4. In each box, the median ratio between the number of fluorescence photons in the cloudy condition and in clear atmosphere for the same event is written. The errors correspond to the 68% confidence interval. For low cloud altitudes (green boxes), especially for large θ, light curve is very similar to that for clear sky. Therefore, showers are potential to reproduce arrival direction and energy. For intermediate clouds (yellow boxes), absorption is present in light curves. However, at least, a lower limit of the energy can be estimated. Also, since the shower track is not affected, the angular reconstruction can be achieved. On the other hand, for higher cloud altitudes (red boxes), specially for vertical showers, light curve is cut at the firsts GTUs. Therefore, to reconstruct the primary energy is not feasible. Nevertheless, for these cases trigger efficiency is low also in a clear atmosphere.

	H_c <3 km	3< H_c <7 km	7< H_c <10 km	H_c > 10 km
$\tau_c > 2$	$1.06^{-0.18}_{+0.18}$	$1.13^{-0.55}_{+2.94}$	$0.27^{-0.17}_{+37.16}$	–
$1 < \tau_c < 2$	$1.05^{-0.09}_{+0.20}$	$1.48^{-0.90}_{+11.40}$	$12.00^{-11.97}_{+920.01}$	$0.00^{-0.00}_{+0.23}$
$0.1 < \tau_c < 1$	$0.72^{-0.10}_{+0.06}$	$0.60^{-0.03}_{+0.03}$	$0.65^{-0.03}_{+0.05}$	$0.60^{-0.04}_{+0.02}$
$\tau_c < 0.1$	$0.96^{-0.06}_{+0.04}$	$0.96^{-0.05}_{+0.04}$	$1.06^{-0.18}_{+0.18}$	$0.95^{-0.02}_{+0.04}$

Table 5.2: Ratio between the integral of the fit for cloudy conditions and for a clear atmosphere for $\theta < 30°$

	H_c <3 km	3< H_c <7 km	7< H_c <10 km	H_c > 10 km
$\tau_c > 2$	$0.99^{-0.03}_{+0.03}$	$1.02^{-0.10}_{+0.27}$	$1.13^{-0.22}_{+2.59}$	$2.186^{-0.30}_{+25.13}$
$1 < \tau_c < 2$	$0.99^{-0.04}_{+0.03}$	$1.03^{-0.09}_{+0.28}$	$1.32^{-0.73}_{+112.77}$	$12.91^{-12.89}_{+408.76}$
$0.1 < \tau_c < 1$	$0.99^{-0.09}_{+0.06}$	$0.74^{-0.08}_{+0.14}$	$0.64^{-0.02}_{+0.06}$	$0.60^{-0.02}_{+0.02}$
$\tau_c < 0.1$	$1.00^{-0.02}_{+0.01}$	$0.97^{-0.02}_{+0.02}$	$0.96^{-0.02}_{+0.01}$	$0.95^{-0.02}_{+0.01}$

Table 5.3: Ratio between the integral of the fit for cloudy conditions and for a clear atmosphere for $30° < \theta < 60°$

	H_c <3 km	3< H_c <7 km	7< H_c <10 km	H_c > 10 km
$\tau_c > 2$	$1.00^{-0.01}_{+0.01}$	$0.99^{-0.01}_{+0.01}$	$1.00^{-0.01}_{+0.01}$	$1.17^{-0.16}_{+3.20}$
$1 < \tau_c < 2$	$1.00^{-0.01}_{+0.01}$	$0.99^{-0.02}_{+0.01}$	$1.00^{-0.02}_{+0.01}$	$1.23^{-1.01}_{+3.24}$
$\tau = 0.1 - 1$	$1.00^{-0.01}_{+0.01}$	$1.00^{-0.02}_{+0.01}$	$0.93^{-0.13}_{+0.07}$	$0.73^{-0.09}_{+0.22}$
$\tau < 0.1$	$1.00^{-0.01}_{+0.01}$	$1.00^{-0.01}_{+0.01}$	$0.99^{-0.02}_{+0.01}$	$0.97^{-0.02}_{+0.03}$

Table 5.4: Ratio between the integral of the fit for cloudy conditions and for a clear atmosphere for $60° < \theta < 90°$

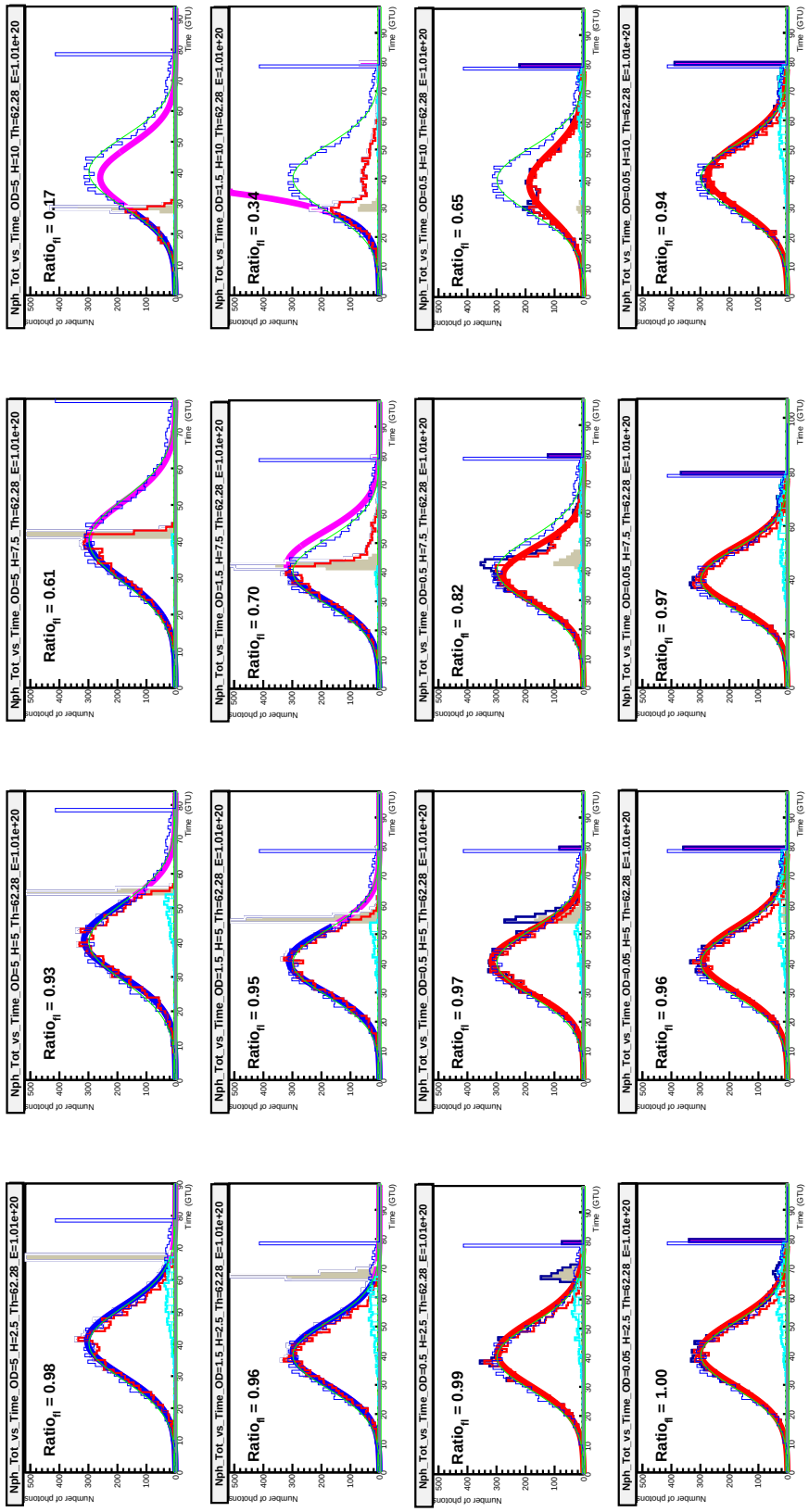

Figure 5.10: Light curves fitted with a gaussian function. The fit has been done up to H_c for optically thick clouds (blue line), and extrapolated until the end of the light curve (magenta line), and using all the EAS signal for optically thin clouds (red line).

5.6 EAS propagation in 3D simulated cloudy scenaries

In the previous sections, several analysis in cloudy conditions with ESAF have been performed. However, ESAF uses a simple model to simulate the cloud (uniform, homogeneus and infinite layer). Improved and more complex atmospheric scenarios are provided thanks to the end-to-end simulations carried out in [101], which will give us simulated atmospheric images based of those we expect to obtain with the JEM-EUSO infrared camera.

In this section we develop a photon propagation module for fluorescence and Cherenkov light, to simulate EAS in different reallistic atmospheric scenarios, which include inhomogeneus and finite 3D scenarios.

5.6.1 3D clouds simulation

Scenarios performed in [101] start with the simulation of an IR image with an atmospheric simulation software, such as the Satellite Data Simulator Unit (SDSU), although also real satellite IR images can be used. The model considers simulated radiation produced by the Earth's surface and atmosphere, the effect of the optics, the detector, the electronics and the image compression algorithm. To perform the simulations, the atmosphere is divided in three dimensional cells (as represented in Figure 5.11), filled with different atmospheric properties (such as humidity, density or type of particles), and including the cloud properties present in some atmospheric scenaries.

5.6.2 Earth's atmosphere curvature

Simulations carried out in [101] have been performed considering the Earth as a plane. This approximation would only be valid for a shower that propagates in this atmospheric model with a low incident angle. Since we want to use this model for showers with any arrival direction, before starting the photon propagation module, we have curved the simulated atmosphere (as an be seen in Figure 5.6.2) following the next steps:

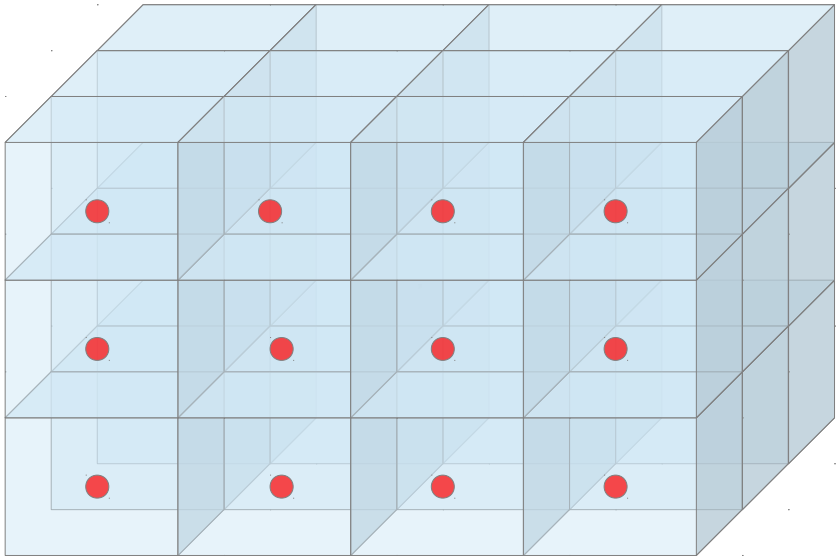

Figure 5.11: The atmosphere is modeled as a rectangular prism divided in cells. In each cell, different phyisical parameters (such as attenuation coefficient) are considered

- first step in our method is to change the coordinates origin from the Earth's surface, to the Earth's center. Therefore, $H = \sqrt{x^2 + y^2 + (z + R_\oplus)^2} - R_\oplus$, where $R_\oplus$ is the Earth radius and corresponds to $R_\oplus$=6.371×10^6 m.

- Second step is to curve the cells and to use angular, better than cartesian, coordinates. To do so, we define two angular variables, θ and ϕ, and a radius r, such that every cell has a size given by:

$$\begin{aligned} \Delta\theta &= \arctan\left(\frac{\Delta x}{H}\right) \\ \Delta\phi &= \arctan\left(\frac{\Delta y}{H}\right) \\ \Delta r &= \Delta z \end{aligned} \tag{5.11}$$

  being Δx, Δy and Δz the half-widths of each cell in the X, Y and Z directions. Now, the width of the cells can be written in terms of $\Delta\theta$, $\Delta\phi$ and Δr.

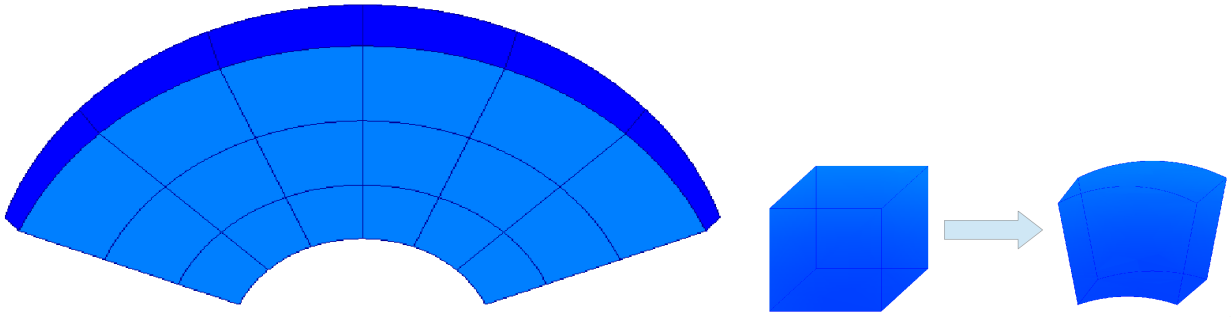

Figure 5.12: The left plot represents how we have curved the simulated atmosphere. The right plot represents how each atmospheric cell is transformed.

- Third step is to translate the coordinates of each bunch and for each step into these angular coordinates, so they can be compared with those of each atmospheric cell to check in which of them the photon bunch is located. Being X_{cr}, Y_{cr} and Z_{cr} the coordinates of each bunch of photons, if $H_{cr} = \sqrt{X_{cr}^2 + Y_{cr}^2 + (Z_{cr} + R_\oplus)^2} - R_\oplus$, the conversion needed will be:

$$\begin{aligned} \theta_{cr} &= \arctan\left(\frac{Y_{cr}}{Z_{cr}}\right) \\ \phi_{cr} &= \arctan\left(\frac{Y_{cr}}{X_{cr}}\right) \\ r_{cr} &= H_{cr} \end{aligned} \tag{5.12}$$

  When the bunch is located in an atmospheric cell, each one of the three coordinates of the bunch is contained inside the lower limit and the upper limit of the corresponding coordinates of the atmospheric cell:

$$\begin{aligned} \theta_{cell} - \Delta\theta_{cell} \leq \theta_{cr} \leq \theta_{cell} + \Delta\theta_{cell} \\ \phi_{cell} - \Delta\phi_{cell} \leq \phi_{cr} \leq \phi_{cell} + \Delta\phi_{cell} \\ r_{cell} - \Delta r_{cell} \leq r_{cr} \leq r_{cell} + \Delta r_{cell} \end{aligned} \tag{5.13}$$

- After these steps, the propagation model can be applied.

5.6.3 Photons propagation

The propagation module developed is independent of ESAF. However, we have used ESAF for the shower generation, although another generator can be used. The number of photons produced by a typical shower of 10^{20} eV is $\sim 10^{15}$. Therefore, raytracing each photon is very time consuming. One solution might be to treat packages of photons instead of individual ones. For this reason, in ESAF the light simulation is done by introducing the concept of bunch. The shower longitudinal distribution is split in slant depth steps dL that can be manually chosen. For this study we have used $dL = 10\text{g/cm}^2$. At each step, one bunch for the fluorescence emission and another for the emitted Cherenkov light are produced. The number of photons contained in each bunch is not constant and depends on the air density at the position where the bunch is assumed to be located [85].

In the upper panel of Figure 5.13, an example of bunches of photons (in this particular case, fluorescence photons) for an EAS of 60° is shown as an example. In the lower panel, the number of fluorescence and Cherenkov photons per bunch for a 60° EAS is presented. The one where more photons are produced would correspond to the shower maximum.

From the shower emission to the telescope detection the photons will travel along the atmosphere, suffering from a certain extinction due to processes such as scattering or absorption, because of the presence of atmospheric particles. This will result into an attenuation of the detected number of photons in comparison to the emitted ones. To calculate this extiction we need to calculate the optical depth between the photon emission point and the telescope as expressed in:

$$\tau = \int_0^L \frac{\rho(l) \cdot dl}{\Lambda} = \int_0^L \alpha(l) \cdot dl \tag{5.14}$$

where $\rho(l)$ is the atmospheric density along the path, Λ is the attenuation length, L is the path and $\alpha(l)$ is the attenuation coefficient along the path [102].

Fluorescence propagation

Fluorescence photons are emitted isotropically. Considering that JEM-EUSO is located at 400 km and its size is ~ 3 meters of diameter, the probability of fluorescence scattered

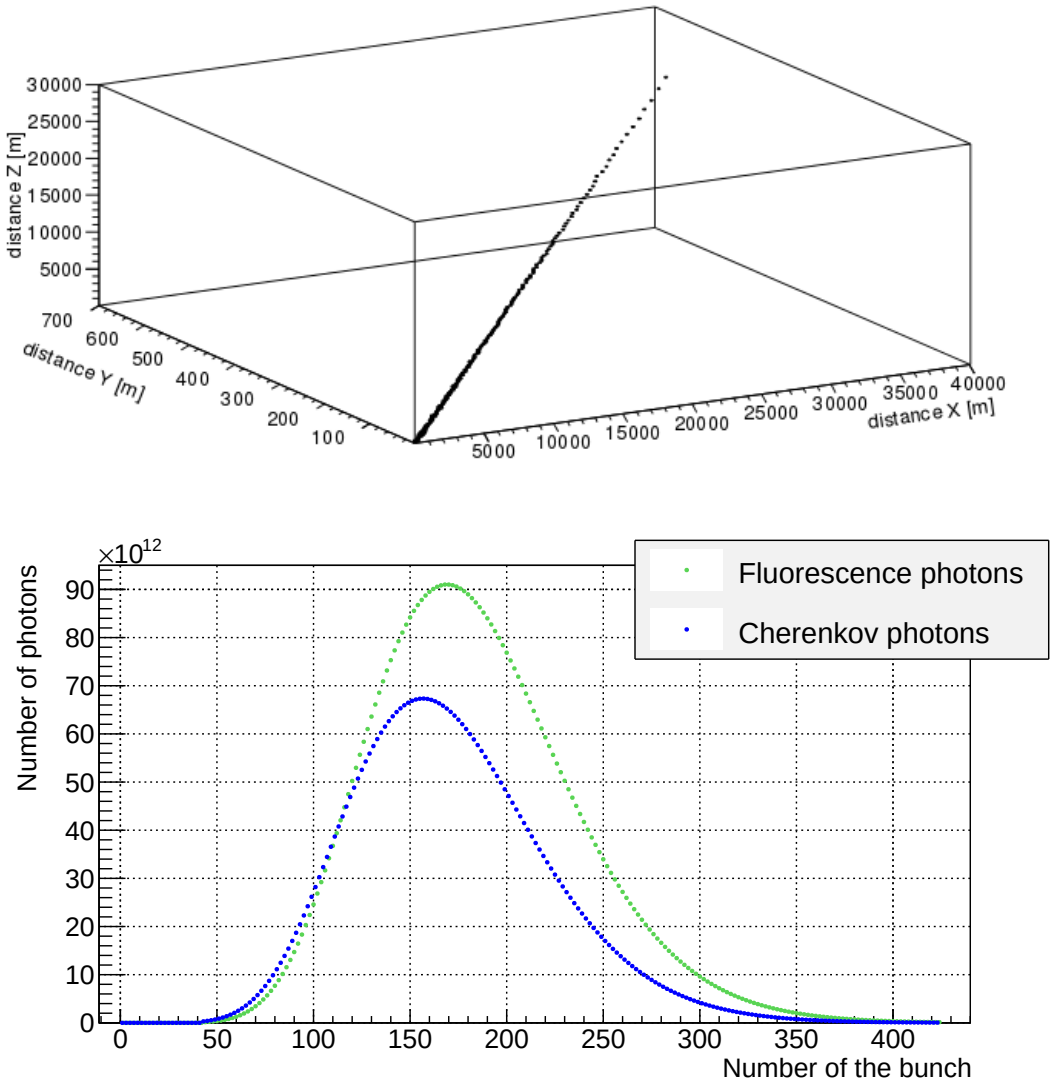

Figure 5.13: In the upper panel, bunches are simulated for an standard shower of 60° and 10^{20} eV. Each bunch is created every 10 g/cm^2 and produces a different number of photons. In the lower panel, the number of fluorescence and Cherenkov photons per bunch for a 60° EAS is presented.

photons reaching the telescope is very small. Therefore, as a good first approximation, we consider in our model that only fluorescence photons emitted in the JEM-EUSO direction arrive to the telescope. Then, we find out in which atmospheric cell the fluorescence

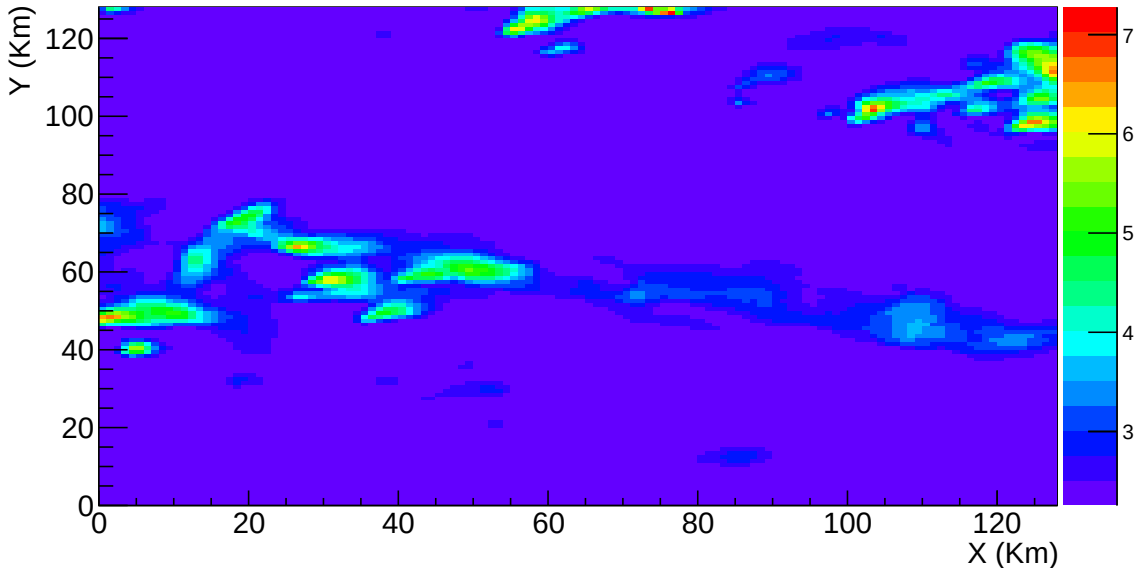

Figure 5.14: Simulation of how a real cloud would be seen by the IR camera.The color scale represents the optical depth vertical profile.

bunches are produced, and for each one of them, the attenuation between the emission point and the detector is calculated. Considering the number of photons created in each bunch to be I_0, the number of photons per bunch arriving to the telescope is:

$$I_{det} = I_0 \times e^{-\tau} \times \epsilon \times \frac{A_{JE}}{4\pi d^2} \tag{5.15}$$

where τ is the optical depth between the bunch emission point and the telescope, d is the distance between these two points, ϵ is the detector efficiency and A is the JEM-EUSO area. I_{det} is the number of detected photons per bunch. Figure 5.15 represents the optical depth suffered by each bunch (in terms of its altitude) of the EAS represented in the lower panel of Figure 5.13. The current atmospheric case is the one plotted in Figure 5.14. Figure 5.16 indicates the number of photons detected by JEM-EUSO in this scenario as a function of their detection time.

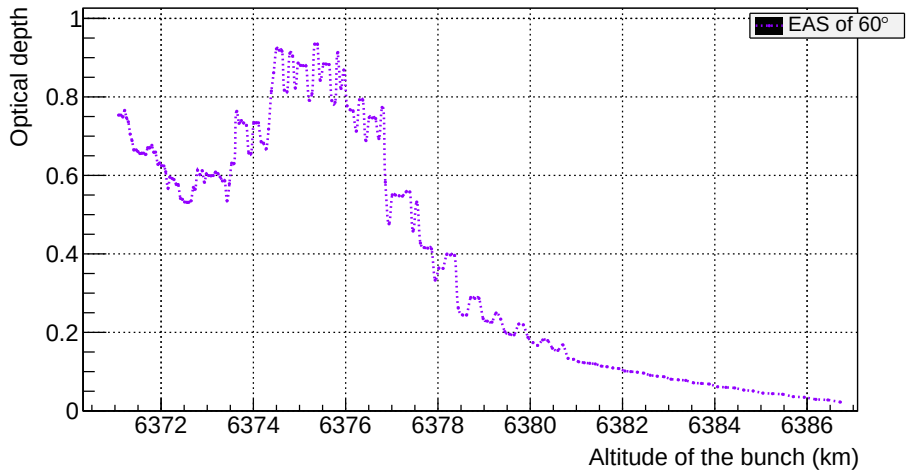

Figure 5.15: Optical depth from the emission point of each fluorescence bunch until the telescope.

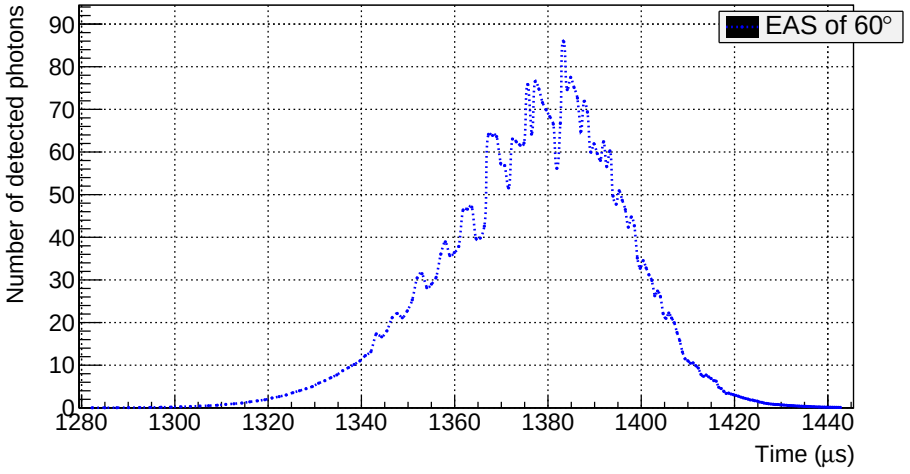

Figure 5.16: Number of photons reaching the telescope as a function of the detection time.

Cherenkov propagation

Cherenkov photons are more complicated to treat than fluorescence ones. Cherenkov photons are emitted very collimated along the path of the shower. Therefore, scattered

photons will arrive to the telescope much more likely than emitted photons. In this work we only take into account the first order of scattering. Thus, we need to consider for every Cherenkov bunch the probability to be scattered along the path, and the probability that this scattering is produced in the direction of the telescope. This scattering depends on the properties of the atmospheric particles, although Rayleigh scattering is assumed as a first approximation.

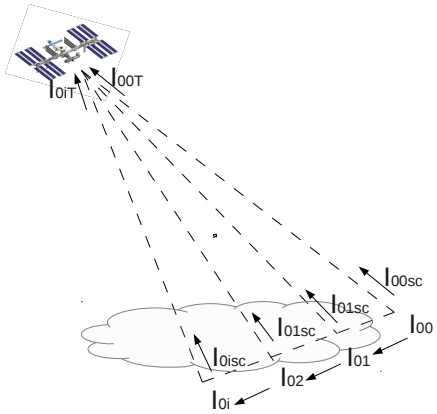

Figure 5.17: Scheme of how for a Cherenkov bunch (I_{00}), in each step i a certain number of photons might be scattered in the direction of the telescope (I_{0isc}).Also, other photons from the bunch are transmitted along the shower direction (I_{0i}).

The Figure 5.17 is a scheme of this procedure as folllows: each bunch (i.e., I_{00}) is propagated along the shower track in steps until the ground level. I_{01},..., I_{0i} are the number of photons that survive in each step. We calculate, from this number, the amount of Cherenkov photons that are scattered in the direction of the telescope (I_{01sc},..., I_{0isc}). Finally, we also consider the absorption produced by the atmosphere from the scattering point to the telescope. Therefore, I_{00T},..., I_{0iT} are the number of scattered Cherenkov photons that will arrive to JEM-EUSO.

Then, we can sumarize that, in our simulations, we will consider only transmitted photons for fluorescence light and scattered photons for Cherenkov component. Figure

5.18 indicates the number of once-scattered Cherenkov photons that are detected by JEM-EUSO in the previous atmospheric case as a function of their detection time.

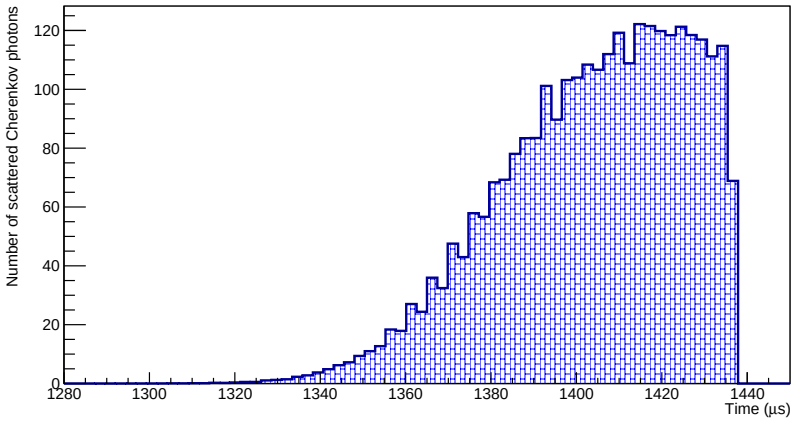

Figure 5.18: Detected Cherenkov light coming to the telescope as a function of the arrival time for the mentioned 60° EAS in the former atmospheric scenario.

Chapter 6

Energy and X_{max} reconstruction in stratus-like clouds

Since the primary energy of a cosmic ray is proportional to the integral of the EAS light curve, its reconstruction is very sensitive to the atmospheric variations. The aim of this chapter is to analyze the effect in the primary energy and X_{max} reconstruction of the presence of clouds in the part of the JEM-EUSO FoV where the EAS is produced.

PmtToShowerReco is the energy and X_{max} reconstruction algorithm created for ESAF in a clear atmosphere. The bases of this algorithm, developed in [87], have been used to reconstruct events in presence of low and optically thick clouds. This algorithm, that works in an iterative way to better constrain the basic parameters of the shower, receives as input the information on the timing and on the position of all the counts. Once the count curve is reconstructed, the The reconstructed signal of GTUs that fall in a gap of the FS are removed. Then, the average atmospheric background is substracted. Finally, the signal is corrected from the efficiency of the MAPMTs, the loss of the FEE, the transmittance of the optical filter and the optics efficiency [51]. There are two main approaches to reach the energy and X_{max} reconstruction through this PmtToShowerReco algorithm:

Slant depth method: it assumes a parameterization for the depth of the shower max-

imum and relies on the arrival direction obtained by the direction reconstruction algorithms (i.e., the direction and X_{max} projection on the FoV are assumed to be known). An initial X_{max0} is assumed but, since X_{max} depends on the primary and on fluctuations, we get rid of the effect of this X_{max0} by iterating the entire procedure [87].

Cherenkov method: it assumes the identification of a Cherenkov mark in the signal. With the time delay between the shower maximum and Cherenkov reflection, knowing the projection of X_{max} and of the Cherenkov bump on Earth is possible to calculate the altitude of the shower maximum (this is, H_{max}). If there is no peak recognized as the Cherenkov bump, the algorithm assumes that this bump corresponds to the last detected photon [87].

6.1 Algorithm modification for energy and X_{max} reconstruction

Even when clouds are present in the JEM-EUSO FoV when an UHECR event occurs, there are particular cases when the primary energy and X_{max} can be anyway reconstructed. In this chapter we adapt the PmtToShowerReco algorithms to be used in a particular case: the presence of stratus-like clouds (i.e., optically thick clouds). The optimal case is when H_c is below the H_{max} and, thus, X_{max} is visible and detected by the telescope. Since the cloud is optically thick, no EAS signal after the cloud will be detected by JEM-EUSO. Also, H_c might be determined by the AMS and, therefore, we can define the altitude of the Cherenkov peak as H_c (since Cherenkov light will be reflected on top of the cloud). Obviously, the lower the H_c is, or the higher the zenith angle of the shower is, more part of the shower develops above the cloud and the case would be more similar to a one in clear atmosphere.

The slant depth method has been modified as follows: once the light curve with the reconstructed peaks is set up, the only part used is the signal corresponding up to two

GTUs before what the algorithm interprets as Cherenkov peak.

On the other hand, for the Cherenkov method we set up the altitude of the Cherenkov reflected bump as the one supposedly obtained by the AMS. X_{max} is determined as in the clear atmosphere case. In Figure 6.1 four examples of real and reconstructed light curves using the Cherenkov method for four zenith angles (30°, 45°, 60° and 75°) at 10^{20} eV are represented. For low zenith angles the Cherenkov bump is more noticeable (first two plots), meanwhile for higher zenith angles it is not always well recognized (as in the last two panels).

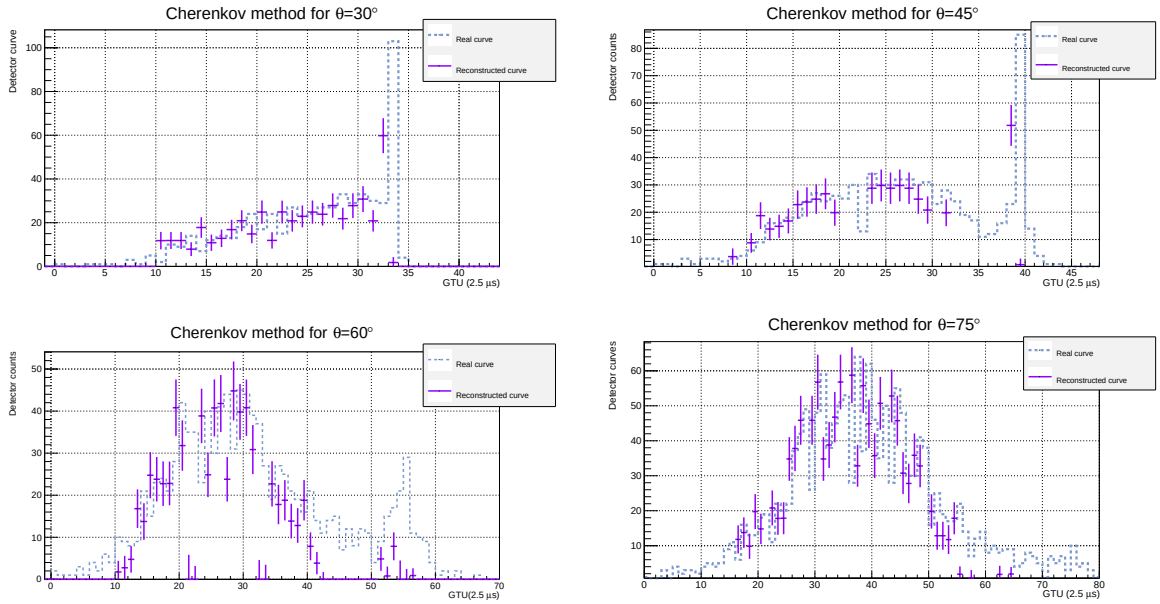

Figure 6.1: Real and reconstructed light curves for four different zenith angles: 30°, 45°, 60° and 75° using the Cherenkov method adapted to be used in presence of clouds.

For large zenith angles the Cherenkov reflected bump is more difusse and difficult to detect. Thus, in these cases the time at which the Cherenkov light has been reflected is more susceptible of not being properly reconstructed. Then, to optimize the reconstruction results for these cases we can set up a minimum number of GTUs that should exist between the shower maximum and the Cherenkov bump, so the algorithm recognize more properly the arrival time for the Cherenkov reflected light. To prove that the two modi-

fied algorithms are working properly, we reconstruct with them 2×10^3 showers at 10^{20} eV (500 EAS at four different zenith angles) in a clear atmosphere and with the EAS impact point along $\pm$ 20 km from the center of the FoV. The energy and X_{max} reconstruction for these events can be seen in Figures 6.2 and 6.3. If we compare these results with those obtained in [87] for similar cases, we can obseve that our results are compatible with those performed for clear sky. Therefore, we can assume that our modificated methods work properly.

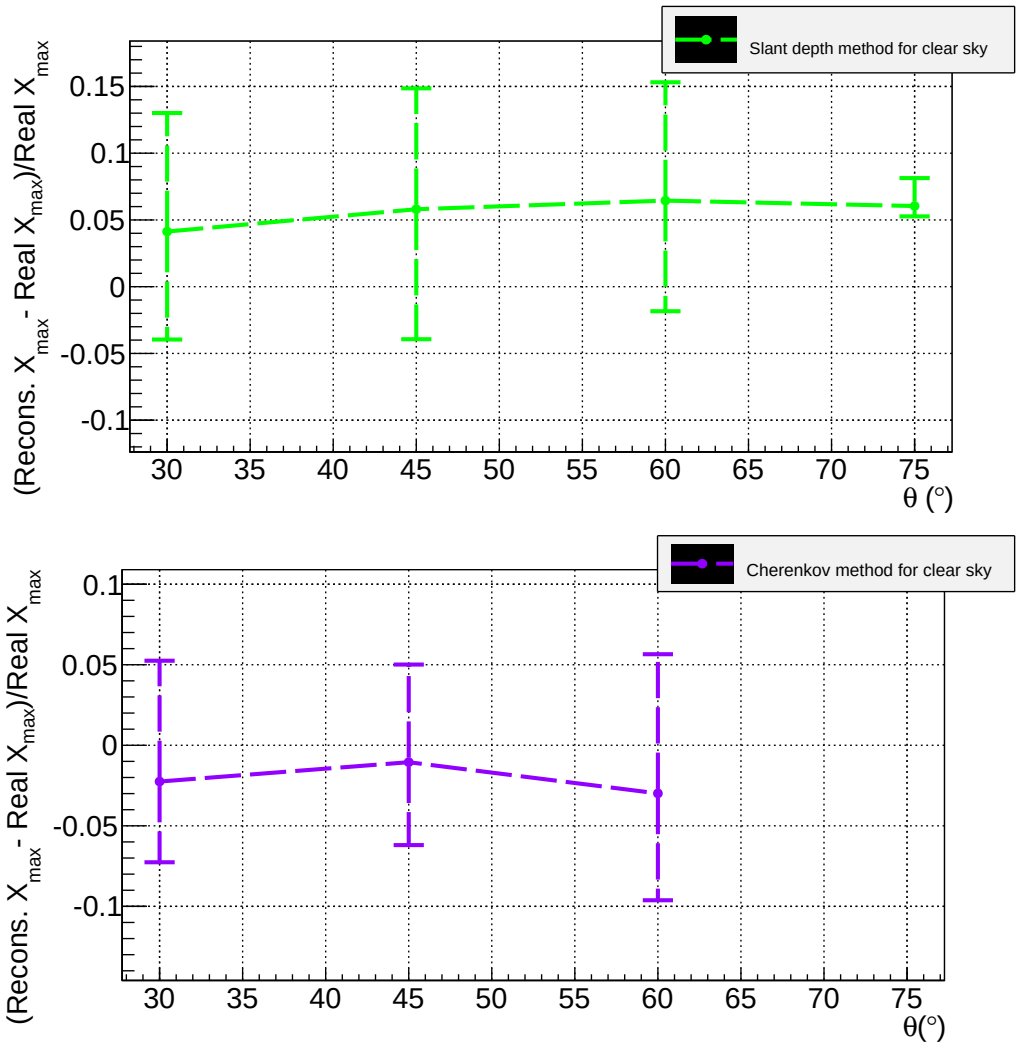

Figure 6.2: Shower maximum reconstruction for clear sky with slant depth method (upper panel) and Cherenkov method (lower panel).

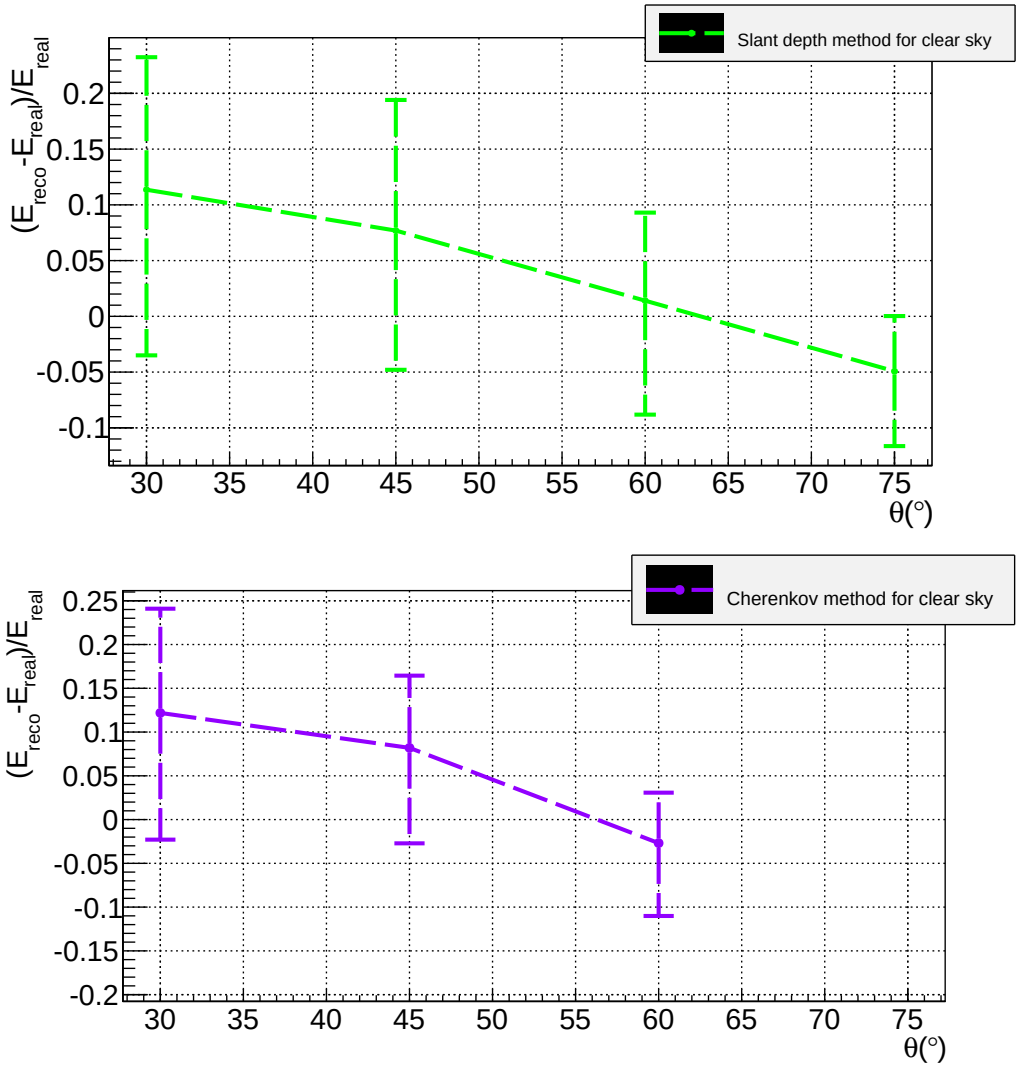

Figure 6.3: Energy reconstruction for clear sky with slant depth method (upper panel) and Cherenkov method (lower panel)

6.2 Efficiency in the detection of the reflected Cherenkov light

One important parameter for the energy and X_{max} reconstruction is the detection of the reflected Cherenkov light either on ground or on the top surface of optically thick clouds.

There are two important aspects to analyze when we are refering to the Cherenkov bump: what it is called *Cherenkov efficiency* and what we name *Cherenkov quality*.

The Cherenkov efficiency is the number of showers where a peak is selected as Cherenkov bump (i.e., the algorithm recognizes part of the signal as light arriving to the telescope that corresponds to the reflected Cherenkov light) divided by the total number of reconstructed showers. However, not all the peaks recognized as reflected Cherenkov light are properly identified. Thus, the Cherenkov quality is defined as the difference in GTUs between the reconstructed Cherenkov peak and the real Cherenkov bump. For both Cherenkov and slant depth method, the Cherenkov efficiency should be the same (as can be checked in Figure 6.4). This is because the search of the peaks is made before the election of one of the algorithms for the reconstruction.

For low zenith angles such as 30°, Cherenkov efficiency increases when H_c decreases. The reason is that for these EAS the signal track is short. Then, the higher the cloud is, the closer X_{max} and the cloud will be. For higher clouds, the Cherenkov bump might be confused with the shower maximum peak, or it even occurs before the maximum, so Cherenkov peak will not be recognized.

At intermediate zenith angles such as 60°, the Cherenkov efficiency slightly diminish in clear sky. Low clouds make the Cherenkov reflection brighter due to the scattering processes on the top surface of the cloud. That is why the Cherenkov efficiency increases in presence of low clouds for these inclinations.

For high zenith angles as 75°, the Cherenkov signal reflected to the telescope in clear sky is negligible. Since they develop higher in the atmosphere, the presence of low clouds (lower than 3km) could be considered as clear atmosphere. Thus, the Cherenkov efficiency in those cases will be very low. For higher clouds, on the other hand, the Cherenkov efficiency increases since the cloud is making the reflected Cherenkov signal much brighter.

To analyze the Cherenkov quality, we select only the showers where one peak has been reconstructed as the reflected Cherenkov contribution. We represent the difference in GTUs between the reconstructed Cherenkov bump and the real one for the 2×10^3 showers in Figure 6.5 (for the slant depth method) and Figure 6.6 (for the Cherenkov

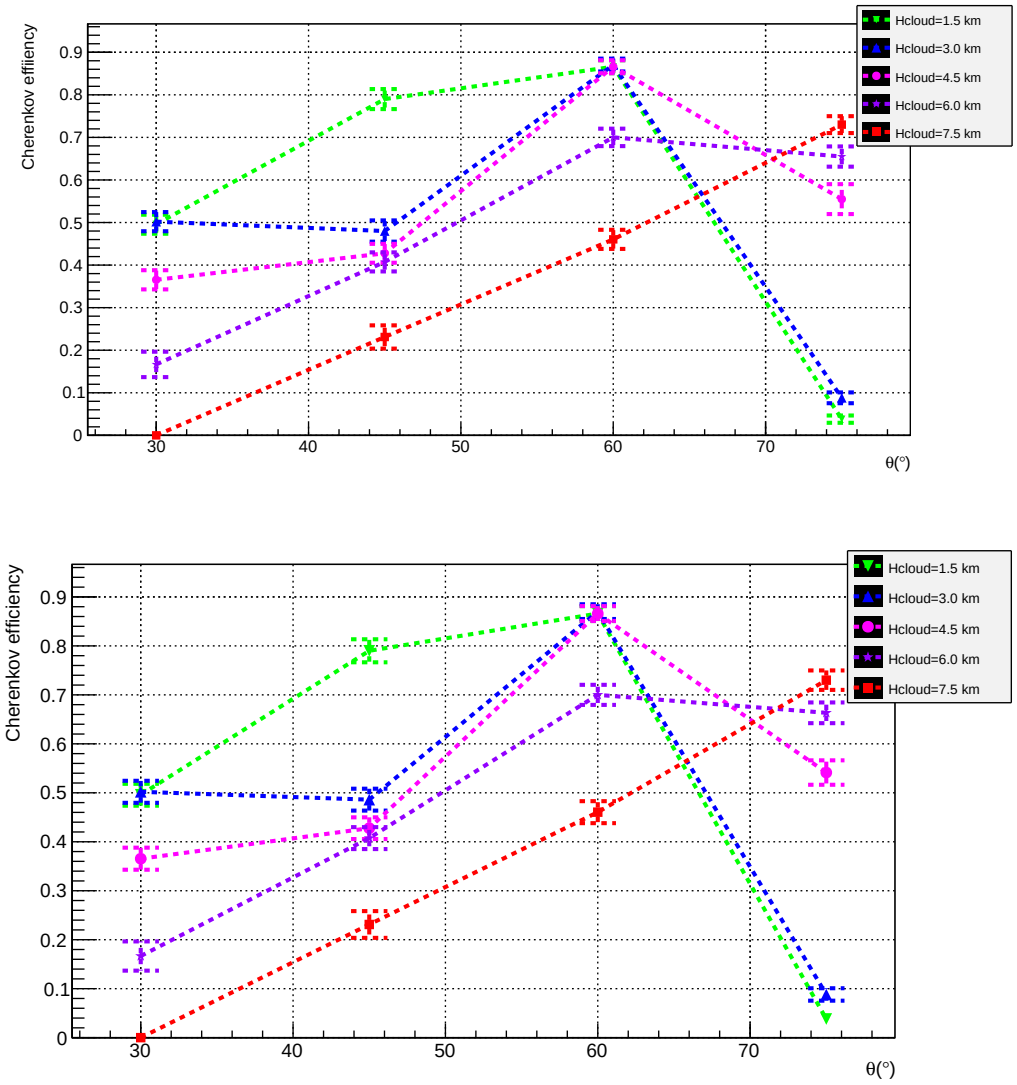

Figure 6.4: Cherenkov efficiency for 2×10^3 EAS of different zenith angles (30°, 45°, 60° and 75°) at 10^{20} eV in presence of optically thick clouds (whose altitudes are 1.5 km, 3 km, 4.5 km, 6 km and 7.5 km). The upper figure represents the Cherenkov efficiency obtained with the slant depth method. The lower one is for the Cherenkov method.

method).

We observe that the median GTUs difference for low, intermediate and high zenith angles is zero. This means that no sistematic errors have been found in our methods.

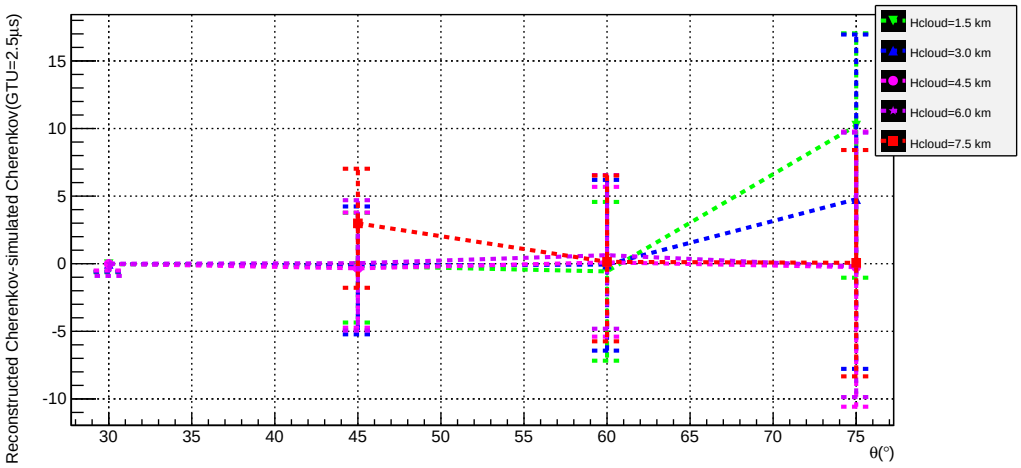

Figure 6.5: Difference in GTUs for the slant depth method between the reconstructed reflected Cherenkov light and the real one.

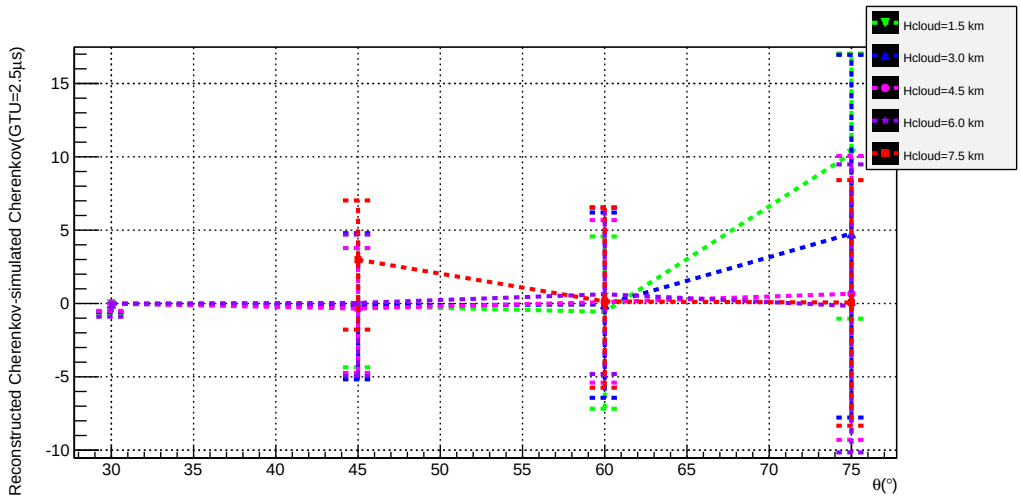

Figure 6.6: Difference in GTUs for the Cherenkov method between the reconstructed reflected Cherenkov light and the real one.

For low zenith angles, the differences in GTUs are very small (around 1 GTU). This is because very inclined showers develop very fast (they last around 30 GTUs). For showers with high zenith angles, on the other hand, this difference is very high, since these EAS

last much more (around 80 GTUs). However, the absolute difference is still small (Figure 6.7). Also, they develop high in the atmosphere where the atmospheric density is lower, and therefore the EAS slant depth differences will also be very small.

For the normalized differences we find out that worse results are given for clouds with higher altitudes than EAS maximum (for instance, for an EAS of 45° and a cloud of H_c = 7.5 km). However, cases where X_{max} is below H_c are not included in our 72% of cloud efficiency that was defined in Chapter 5.

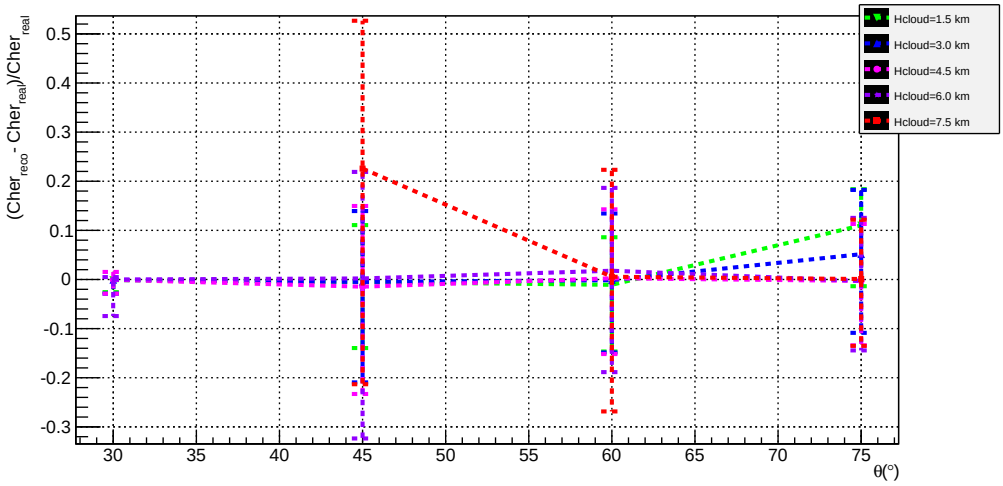

Figure 6.7: Normalized difference in GTUs between the reconstructed reflected Cherenkov light and the real one for the slant depth method (upper panel) and for the Cherenkov method (lower panel).

6.3 Quality parameters for the energy and X_{max} reconstruction

6.3.1 The χ^2_{pdf} parameter

The most common parameters used for defining the reconstruction quality are the number of degrees of freedom (DOF) and the χ_{pdf} of the fit. For a clear atmosphere, the number

of DOF considered as a good quality cut was $DOF > 5$ [87]. However, in presence of clouds with H_c near X_{max} this election will reduce significatly the reconstruction efficiency. Therefore, for cloudy cases we assume as a quality cut $DOF > 2$. We observe in Figure

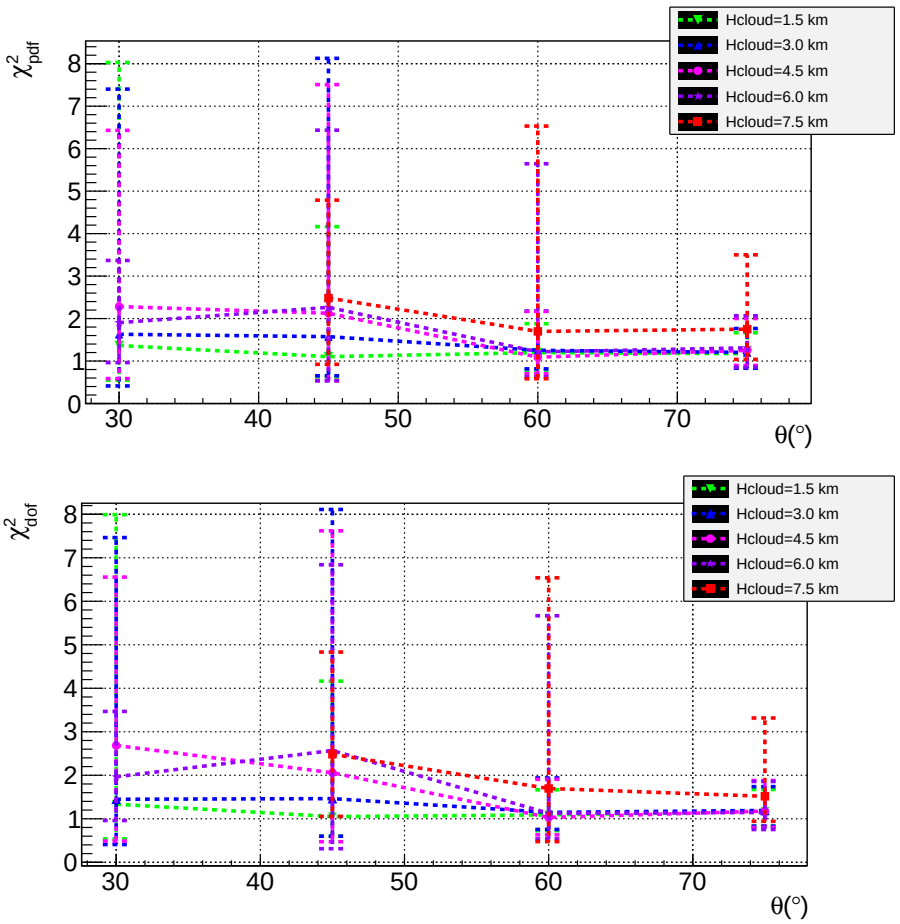

Figure 6.8: χ^2_{pdf} distribution for four zenith angles (30°, 45°, 60° and 75°) and four different cloudy conditions, when the slant depth method is used (upper panel) and when the Cherenkov method is used (lower panel).

6.8 that the χ^2_{pdf} distribution is not good (we would consider as a quality cut $\chi^2_{pdf} < 2$). To check if this effect is produced by the reconstructed geometry of the shower, we make the same plot considering only EAS where the reflected Cherenkov light has been detected. This is represented in Figure 6.9. Here, we can see that for both methods the χ^2_{pdf} gets better. Moreover, the Cherenkov method might give us slightly better results because

we assume the altitude of this Cherenkov peak is well known, unlike for the slant depth method.

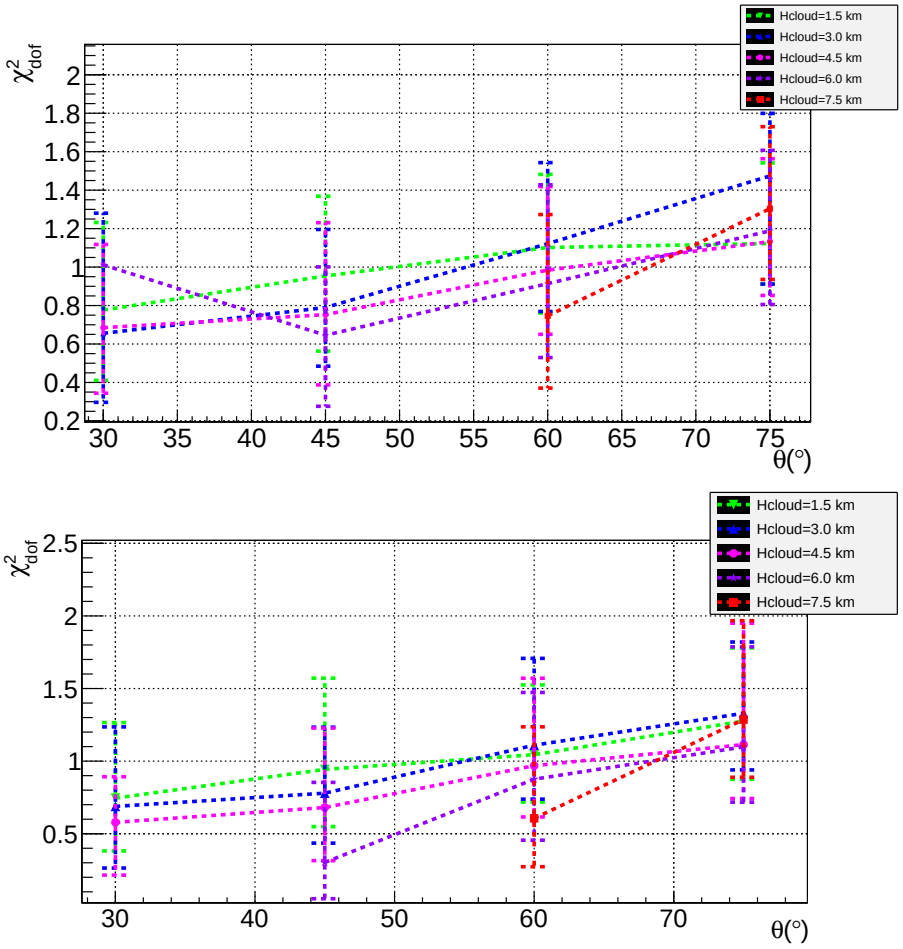

Figure 6.9: χ^2_{pdf} distribution for events whose Cherenkov bump has been recognized, for four zenith angles (30°, 45°, 60° and 75°) and four different cloudy conditions, when the slant depth method is used (upper panel) and when the Cherenkov method is used (lower panel).

6.3.2 Real and reconstructed GTUs between X_{max} and H_c

One of our goals was to analyze how the quality of the reconstruction varies depending on the proximity of the shower maximum to the cloud. To do so, we have studied the

number of GTUs between X_{max} and H_c. The example shown in Figure 6.10 consists of

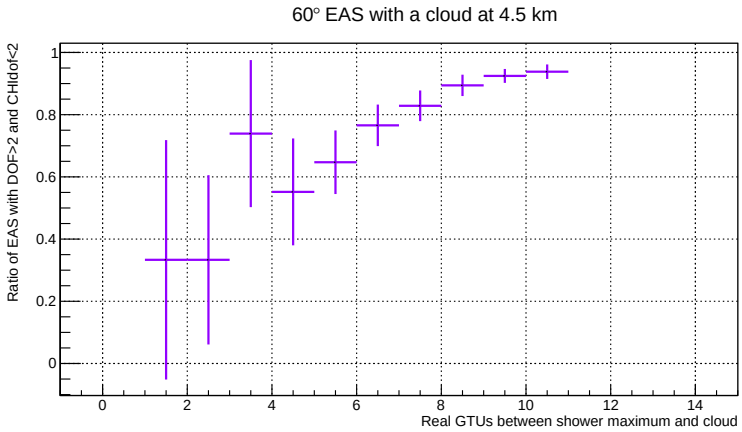

Figure 6.10: Number of real GTUs between the shower maximum and the cloud top height for 10^4 EAS with an energy of 10^{20}eV and a zenith angle of 60°.

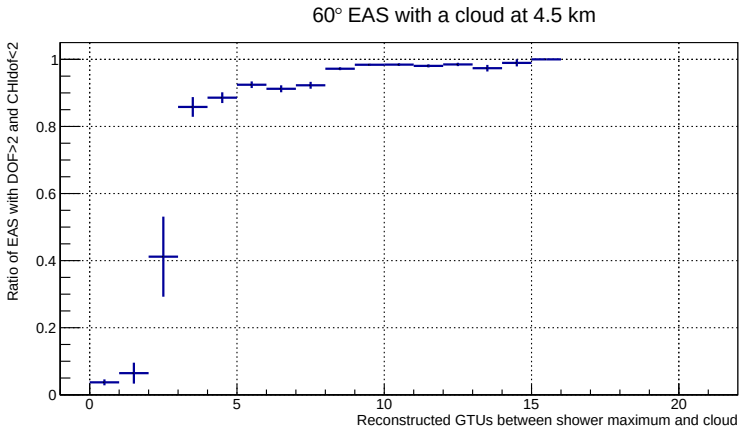

Figure 6.11: Number of reconstructed GTUs between the shower maximum and the cloud top height for 10^4 EAS with an energy of 10^{20}eV and a zenith angle of 60°.

10^4 EAS with an energy of 10^{20} eV and a zenith angle of 60°. Here, it is represented the number of showers that fullfill our quality requirements ($DOF > 2$ and $\chi^2_{pdf} < 2$) in terms of the number of GTUs between the shower maximum and the cloud top. It is seen that to achieve a $\sim 90\%$ of events fullfilling our quality criteria, the Cherenkov bump would

be produced at least eight GTUs after the shower maximum. On the other hand, looking at the reconstructed GTUs between the shower maximum and the cloud in Figure 6.11, only at least six reconstructed GTUs are neccesary to achieve a $\sim 90\%$ of events fullfilling our quality criteria.

6.4 Energy and X_{max} reconstruction efficiency for stratus-like clouds

Now that we have tested that the algorithm modification for stratus-like cases in both methods works properly, we calculate the energy and X_{max} reconstruction for these $2{\times}10^3$ cloudy cases at 10^{20} eV using the arrival direction information obtained by PWISE [88] (i.e., we use the reconstructed geometry and not the real one to determine the energy and the shower maximum). It is important to remember that these showers are simulated to impact on ground near the center of the FoV ($\pm$ 20km, $\pm$ 20km), where the efficiency of the telescope is better than in the rest of the FoV. Also, we consider for this analysis only EAS that have passed the JEM-EUSO trigger.

To analyze the quality of our algorithms in reconstructing the energy and X_{max} of the UHECR, we define "reconstruction efficiency" as the ratio between the number of showers that are reconstructed under certain quality cuts (for our study, $DOF > 2$ and $\chi^2_{pdf} < 2$) in a determined cloud condition, and the number of the showers that have triggered.

Note that depending on the resolution that we need for some studies, another quality cut that might be useful is the detection of the Cherenkov bump, no matter whether the altitude at which this bump occurs is known (Cherenkov method would be used) or not (slant depth method would be used). This quality cut would reduce our "properly reconstructed" showers to around $\sim 55\%$, although the quality of the reconstruction will increase.

In Figures 6.12 and 6.13 it is shown the reconstruction efficiency for the slant depth method and the Cherenkov method, respectively. For both methods the reconstruction

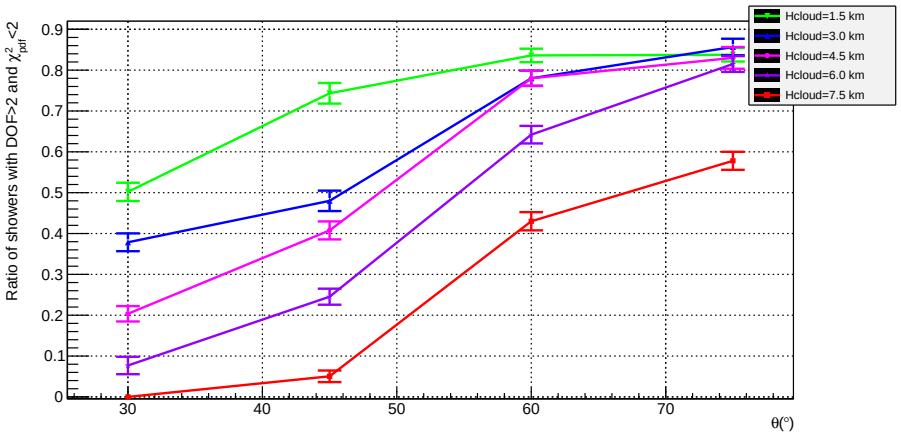

Figure 6.12: Efficiency reconstruction for the slant depth method.

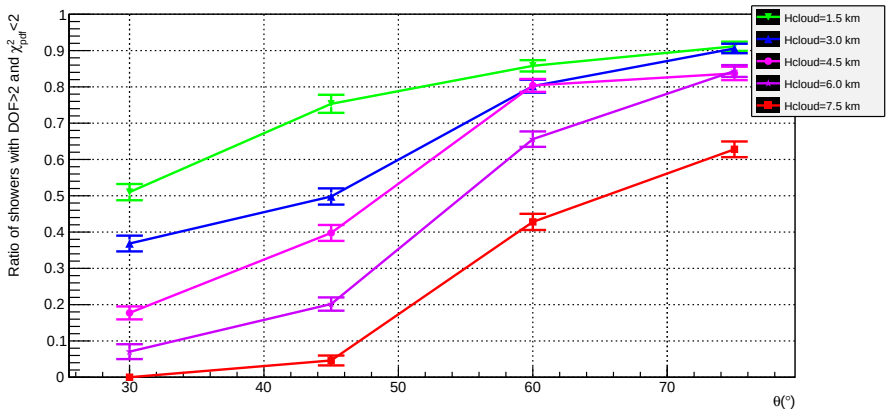

Figure 6.13: Efficiency reconstruction for the Cherenkov method.

efficiency is very similar for each cloudy case. This is because we have considered showers where the Cherenkov bump has been recognized and, as stated before, the Cherenkov bump search is produced before the reconstruction algorithm is selected.

For further studies, we only consider cases where $X_{max} > H_{cloud}$, because for optically thick clouds only these cases are included in the 72% of cloudy efficiency (Chapter 5).

6.4.1 Energy reconstruction

To analyze the resolution of the energy reconstuction we calculate the relative error in reconstructing the energy, given by $(E_{reco} - E_{real})/E_{real}$, as represented in Figure 6.14. The upper panel represents the resolution for the slant depth method, while the lower panel uses the Cherenkov method. The dots show the median of the distributions for each condition (for each zenith angle and cloud condition) while the errors show the $\pm 34\%$ confidence intervals.

For both methods in general the resolution is acceptable. However, it gets worse when zenith angles are small and H_c is near X_{max} (for example, $\theta = 30^\circ$ and $H_c = 3$ km). When zenith angles are higher, although H_c is near X_{max} (for instance, $\theta = 45^\circ$ and $H_c = 4.5$ km or $\theta = 60^\circ$ and $H_c = 6$ km), the resolution is better than for the former case. This is because the light curve above the cloud lasts more GTUs, so the fits (and therefore, reconstruction parameters) are better. The highest resolution for the energy reconstruction occurs at the highest zenith angles (such as $\theta = 75^\circ$), because from the beginning of the shower to the shower maximum there is more shower development to be used for our fit.

In the two panels we can observe a trend: the median ratio smoothly decreases when the zenith angle increases. The reason is the following: since the Cherenkov bump is very faint for $\theta = 75^\circ$, some background noise can be misinterpreted as the Cherenkov peak. To get rid of this effect, we slightly increased the background that was substracted from the signal before the reconstruction analysis. Then, the signal gotten is slightly lower and, thus, the reconstructed energy is also lower.

6.4.2 Shower maximum reconstruction

To analyze the resolution of the X_{max} reconstruction, a similar procedure for the same showers has been carried out. The shower maximum is more sensitive to the geometry of the shower. As in the case of clear atmosphere, an iteration procedure is needed to be performed in the future.

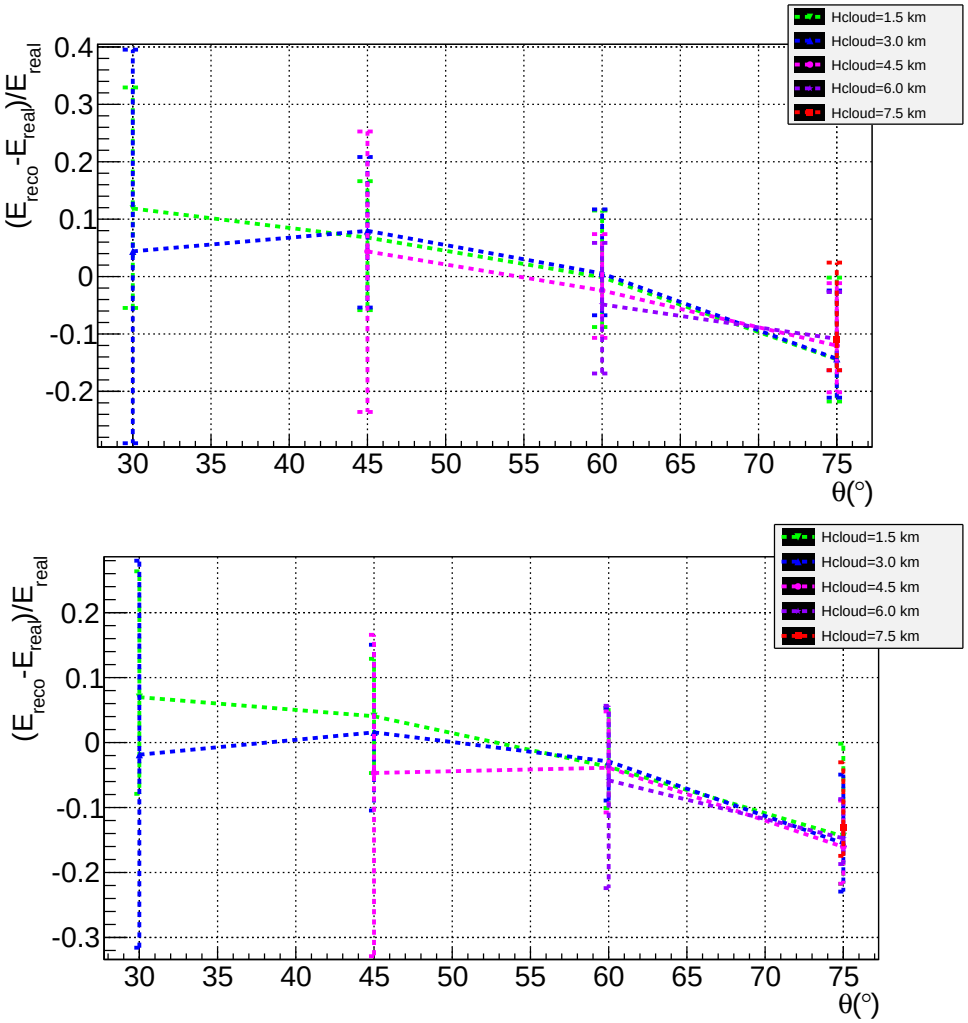

Figure 6.14: The upper figure shows the resolution of the energy reconstruction using the slant depth method for showers whose shower maxima are above the top cloud height. The lower figure shows the same using the Cherenkov method for the EAS reconstruction.

When we study the X_{max} resolution, expressed by $(Recons.X_{max} - RealX_{max})/RealX_{max}$, we obtain different results for the slant depth method (Figure 6.15, upper panel) and for the Cherenkov method (Figure 6.15, lower panel). For the slant depth method the results are worse for inclined showers in presence of clouds near their shower maximum. This is because, as stated before, the shower maximum is very sensitive to the EAS geometry changes. Since, for these EAS the geometry is more difficult to reconstruct, the shower

maximum resolution will be lower than that for higher zenith angles or EAS in presence of lower clouds. For the Cherenkov method, on the other hand, the resolution of the shower maximum is worse for more horizontal EAS in presence of low clouds. For this method, the Cherenkov bump determination is important and, since for these EAS the Cherenkov peak is more difficult to reconstruct (and it is used as a key part of the geometry), the shower maximum resolution is worse than that for more inclined showers or EAS in presence of higher clouds.

6.5 Reconstruction along the full FoV

The previous results are only valid for EAS located near the center of the FoV. The next step is to analyze EAS along the full FoV. To do so, 2×10^3 showers in four different cloudy conditions have been simulated along ($\pm$270 km, $\pm$200 km).

6.5.1 Energy reconstruction

The JEM-EUSO detector efficiency decreases with the distance to the center of the FoV. Moreover, showers detected at the edge of the FoV might not be fully developed inside the FoV, and the signal might be only partially observed by JEM-EUSO.

This is the reason why, for events whose X_{max} is above but near H_c (for example, in Figure 6.16, the 45° EAS in presence of a cloud at 4.5 km), the energy resolution gets worse with the core distance to the center of the FoV (as it is seen if Figures 6.14 and 6.16 are compared).

Also, as stated before, for high zenith angles the Cherenkov peak is broader and fainter (as can be seen in Figure 6.16, the 75° EAS in presence of a cloud at 1.5 km). When this peak takes place further from the center, its recognition is more problematic due to the worse detector efficiency. This can lead to a worse resolution for both (Cherenkov and slant depth) methods.

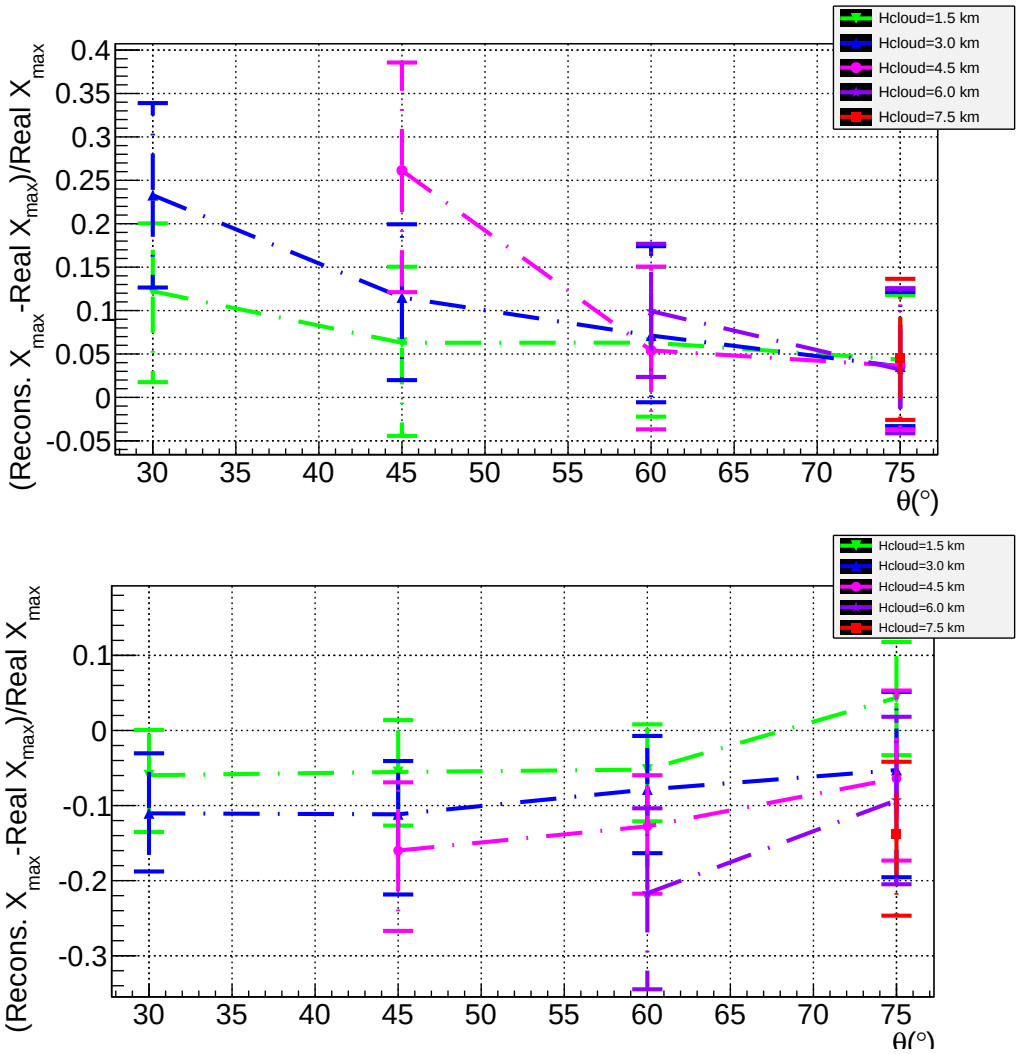

Figure 6.15: The upper figure shows the resolution of the shower maximum using the slant depth method. The lower figure shows the shower maximum resolution using the Cherenkov method for the EAS reconstruction.

6.5.2 Shower maximum

For the shower maximum reconstruction, we carry out a similar procedure to the one used for the energy reconstruction. This is, we reconstruct the shower maxima for the 2×10^3 events simulated along ($\pm$270 km, $\pm$200 km) using both (Cherenkov and slant depth) methods. Then, we compare the shower maximum reconstruction for events near

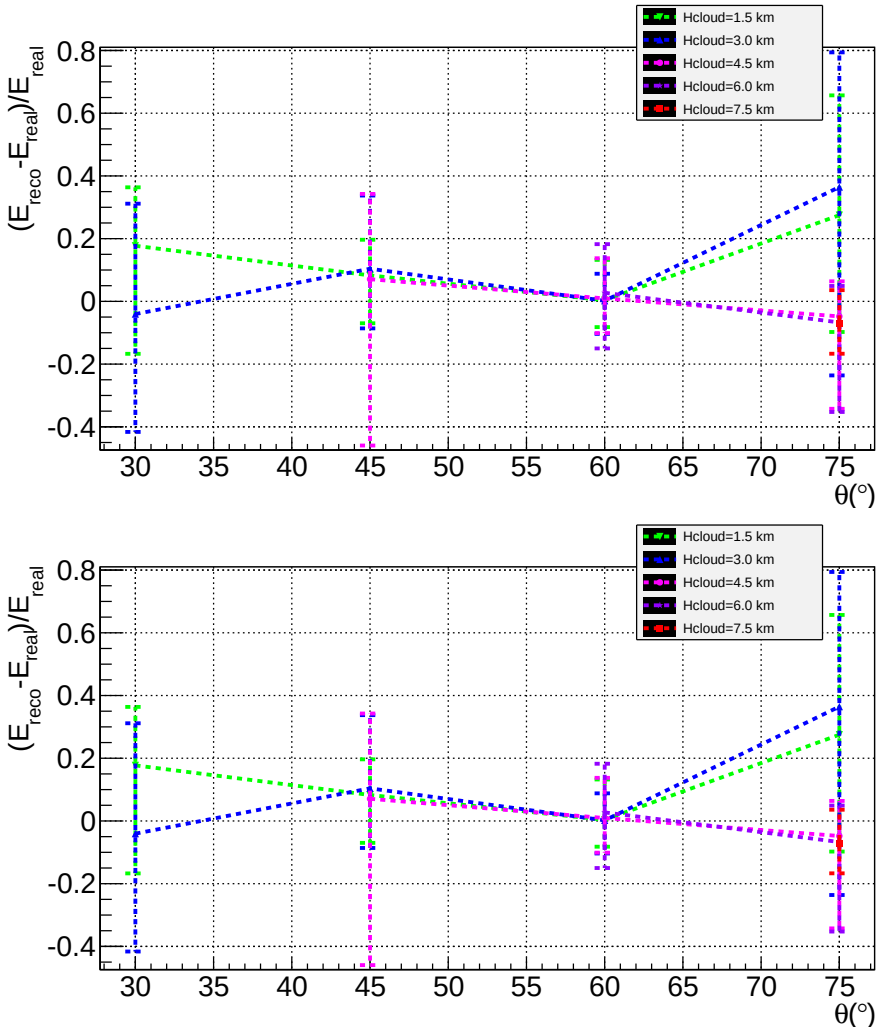

Figure 6.16: Resolution of the energy reconstruction for the slant depth method (upper panel) and for the Cherenkov method (lower panel)for showers along the whole field of view whose shower maxima are above the top cloud height.

the center (Figure 6.15) and for these events along the FoV (Figure 6.17).

For the Cherenkov method the results at higher zenith angles get worse with the distance to the center of the FoV, especially for low clouds (represented in the lower panel of Figure 6.17). This is again because this method is based on the recognition of the Cherenkov reflected signal and, for these cases, the recognition is difficult. Moreover, adding the effect of the lower quality of the optics at the edge of the FoV, the resolution

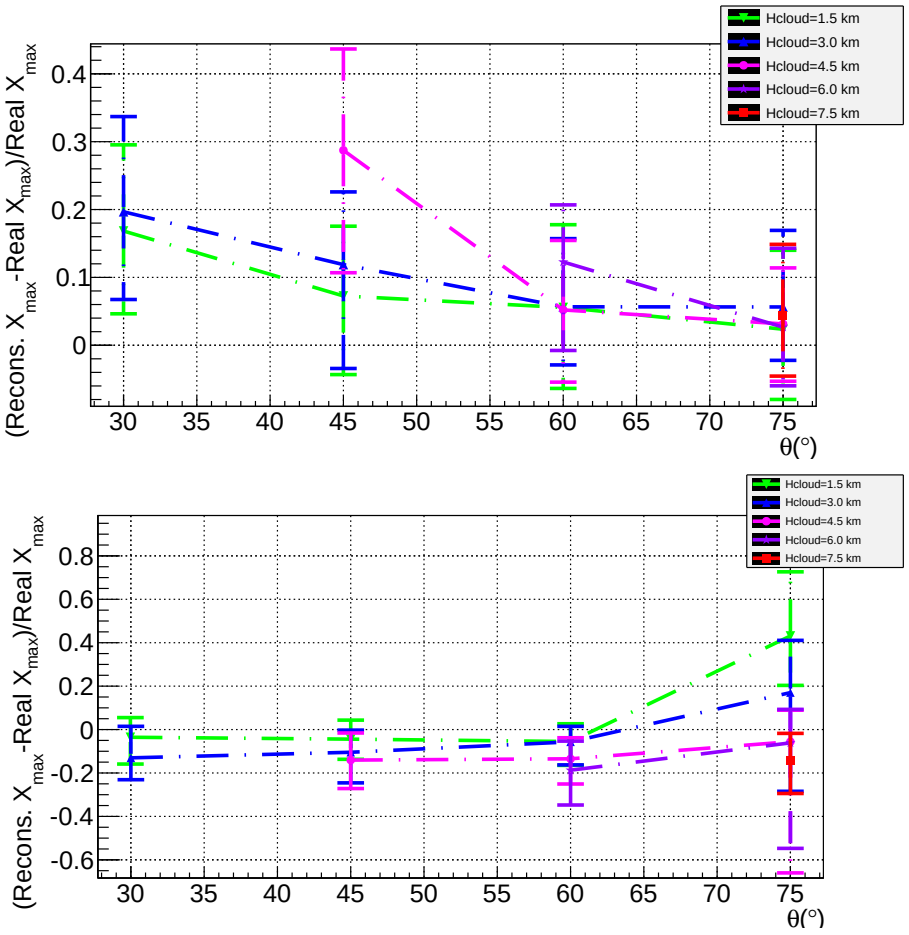

Figure 6.17: Resolution of the shower maximum for the slant depth method (upper panel) and for the Cherenkov method (lower panel)for showers along the whole field of view whose shower maxima are above the top cloud height.

decreases rapidly.

In the slant depth method the resolution slightly gets worse only for events whose shower maxima are above but very near to the cloud top height (for instance, for a 45° EAS and a cloud at H_c=4.5 km, or for a 60° EAS and a cloud at H_c=6 km). This is because the shower maximum is very near to the cloud top altitude. Therefore, if the shower takes place in a location of the FoV with a worse quality, the GTU at which the shower maximum is produced might be difficult to discriminate.

6.6 Energy dependence

The previous studies have been carried out for protons with a standard energy (10^{20}eV). The aim of this section is to find out how the results of both reconstruction algorithms are affected when the primary energy increases or decreases. For this study, 2×10^3 showers under the previous four different cloudy conditions have been simulated with two energies: 5×10^{19}eV and 3×10^{20}eV (one below 10^{20}eV and another one above 10^{20}eV).

When the primary energy is lower than 10^{20}eV (for example, 5×10^{19}eV), the signal of the shower is weaker. Less photons arrive to the detector, so the resolution of the reconstruction will decrease. As can be observed in Figures 6.18 and 6.19, for both methods, the energy (Figure 6.18, upper panels) and shower maximum resolution (Figure 6.19, upper panels) diminish when the energy decreases in a similar way to with the EAS distance to the center of the FoV.

EAS with energies higher than 10^{20}eV (for instance, 3×10^{20}eV) develop deeper in the atmosphere. This means that their shower maxima take place lower in the atmosphere. The inmediate consequence is that events whose shower maxima were located above but very near to the top cloud height for lower energies might have their maxima inside the cloud now. Therefore, the resolution will also decrease.

Then, we can conclude that these reconstruction algorithms are optimized for the energy 10^{20} eV.

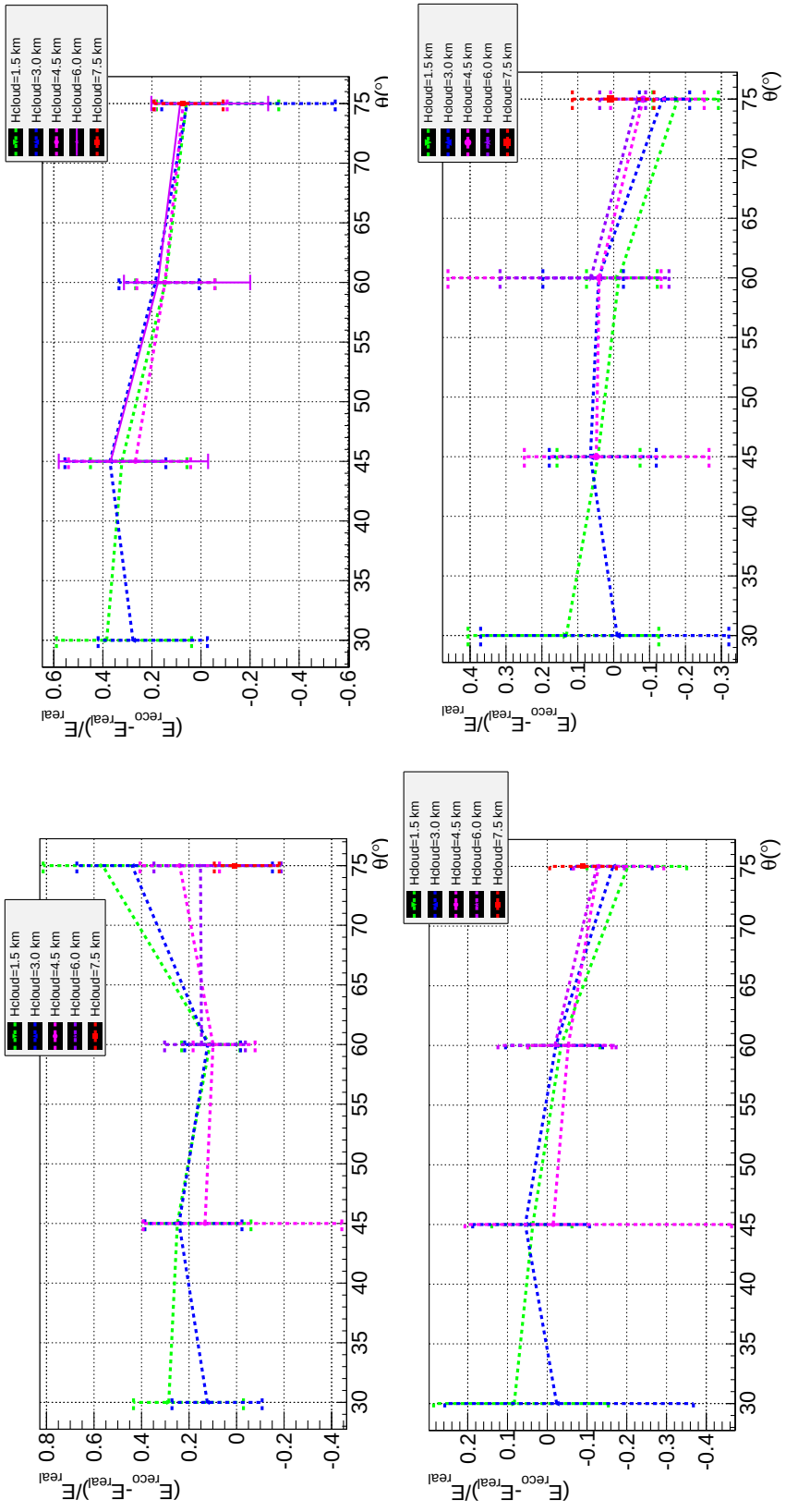

Figure 6.18: Energy resolution for Cherenkov method and 5×10^{19}eV EAS (first panel), for the slant depth method and the same energy (second panel), for Cherenkov method and EAS of 3×10^{20}eV (third one) and for the slant depth method and the same energy (fourth one).

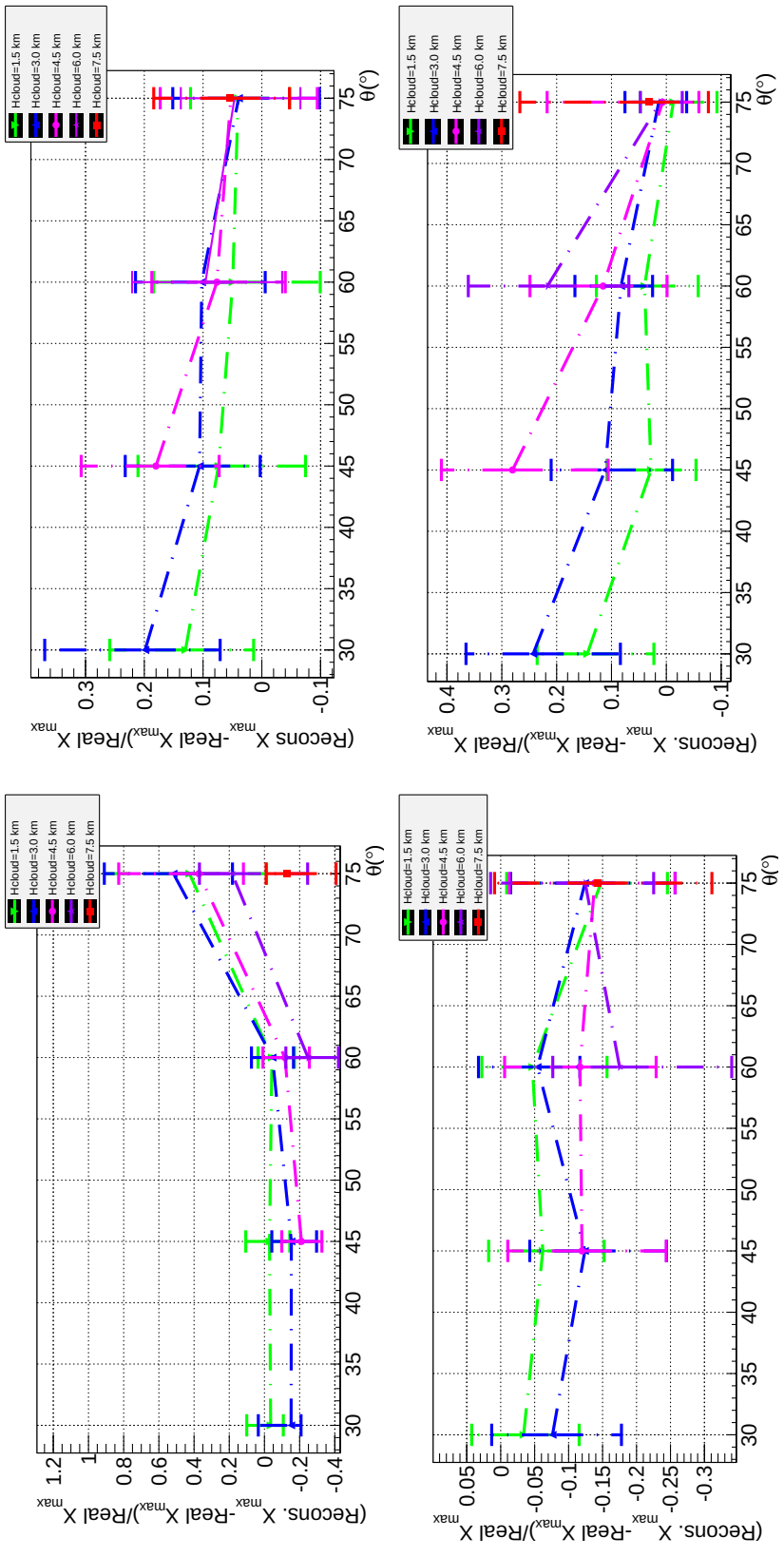

Figure 6.19: Shower maximum resolution for Cherenkov method and 5×10^{19}eV EAS (first panel), for the slant depth method and the same energy (second panel), for the Cherenkov method and showers of 3×10^{20}eV (third one) and for the slant depth method and the same energy (fourth one).

Chapter 7

Conclusions

JEM-EUSO is an international experiment devoted to detect Cherenkov and fluorescence light produced by Extensive Air Showers (EAS) created when Ultra High Energy Cosmic Rays (UHECRs) interact with atmospheric particles. Since the observation area of the telescope is extremely large, we can find very different atmospheric conditions in its Field of View (FoV) at the same time. The accuracy on the reconstruction of the primary cosmic ray parameters depends on the accuracy in measuring the atmospheric conditions in the region of EAS development.

Showers with large zenith angle (θ) produce a larger signal in time, as well as a higher number of photons, than showers with lower θ. An EAS of $\theta = 75°$ starts to develop at an altitude of $\sim$ 20 km, and reaches its maximum development at $\sim$ 12 km. An EAS of $\theta = 30°$, on the other hand, starts its development at $\sim$ 8 km, reaching its maximum at $\sim$ 2 km, deeper in the atmosphere than the previous case. Since JEM-EUSO will observe from above, unlike for ground-based telescopes, the detection of EAS with larger θ will be better than the detection of more vertical showers.

The EAS development also depends on the primary particle. EAS produced by heavier particles (i.e., iron) develop higher in the atmosphere than those produced by lighter particles. Then, heavy particle-induced EAS would be easier to observe by JEM-EUSO. The iron-air interaction cross section is four times higher than that of the proton-air interaction. Then, iron-induced showers develop higher, in the less dense part of the

atmosphere, making a longer lasting development. While a proton-induced shower at $\theta = 60^\circ$ reaches its maximum 25GTUs after the shower starts to develop, an iron-induced shower at the same zenith angle reaches its maximum 35GTUs after the beginning of the EAS development.

Besides the EAS physical parameters, we need to consider their location in the JEM-EUSO FoV. For instance, showers whose cores are located in the center of the FoV will be detected by JEM-EUSO as brighter and larger in time than the ones located at the edge of the FoV. We define γ as the angular distance between the center of the FoV and the shower core location. A standard shower with a primary energy of 10^{20} eV and a zenith angle of 60° with an angular distance of 15° (with a duration of $\sim$ 50GTUs), suffers a shortening in its shower track by a factor of $\sim$ 17% when it is compared with the same EAS landing at the center of the FoV(whose duration is $\sim$ 60GTUs). We can obtain a similar duration for different zenith angles and different γ. For instance, the duration of an EAS of 40° at the center of the FoV (γ=0) is equivalent to that of an EAS of 30° with a separation angle of $\gamma = 10^\circ$.

The number of detected photons by one pixel depends on the distance between the emission position and the telescope, the atmospheric attenuation between them, and the subtended solid angle from JEM-EUSO to the photon emission location. For example, we can compare an EAS landing on the center of the FoV with a similar one landing at $\gamma = 15^\circ$. The distance between the core and the telescope will increase 4%. The solid angle will be 1.12 times larger than the solid angle subtended by JEM-EUSO for $\gamma = 0$. One pixel at the edge of the focal surface will have lower resolution that another at the center of the FoV because it is observing a larger area. This observation area increases when the angular distance to the center of the FoV increases. For a pixel which observes at a distance $\gamma = 15^\circ$, its observation area increases a factor of 15% in comparison with the area observed at the center of the FoV.

To investigate clouds impact in the overall observation efficiency, we define the *cloud efficiency*. It corresponds to the fraction of events that fulfill the *maximum development visibility* requirements, where we include events in presence of optically thin clouds ($\tau_c <$

1) or those with lower than the altitude of the shower maximum. The reason is that optically thin clouds attenuate the EAS signal only by a factor of $e^{-\tau_c}$. For a cloud of $\tau = 0.25$, the number of photons after the cloud suffer a reduction of $\sim 22\%$. If this cloud is located at an altitude of 8 km (which is already a high cloud), an EAS arriving at $\theta = 60^\circ$ suffers an absorption of 18%. An EAS arriving at $\theta = 75^\circ$ reduces its number of photons only an 8%, since more part of the shower development takes place before the cloud than that for the previous case. For optically thin clouds the EAS signal is still significantly visible. Then, their influence in the JEM-EUSO trigger efficiency is not significant. Optically thick clouds ($\tau_c > 1$), on the other side, significantly absorb the EAS signal originated below the cloud. This means that the number of photons emitted in the direction of the JEM-EUSO telescope above the cloud need to activate the trigger. However, if the EAS is triggered and the shower maximum (X_{max}) is visible (above the cloud), we estimate that enough signal is visible to analyze the event. At high energies ($E > 10^{19}$ eV), this "cloud efficiency" is approximately constant and account for $\sim 72\%$ of the trigger EAS. This study has been carried out for proton-induced showers as a conservative approximation. Since proton-EAS develop deeper in the atmosphere than any other hadron-induced shower of similar parameters, UHECRs induced by heavy particles would have a higher cloud efficiency than protons.

According to the effect of clouds on the reliability on the energy estimation, we have classified the events plus atmospheric conditions in groups. The first group involves events whose shower maximum takes place above the cloud. The number of detected photons by the telescope is very similar to that of the same event in clear atmosphere and, therefore, the estimated energy is reliable. The second group involves events which take place in presence of an optically thin cloud above the shower maximum. For these events, the telescope detect a significantly reduced number of photons. This means that the energy of the event cannot be properly estimated, although a lower threshold can be given. Since the signal is not totally lost due to the low optical depth, the shower direction reconstruction is still achievable. The last group involves events whose development have taken place mainly below the cloud. These events cannot be included in our EAS studies.

However, most of them will not trigger. The classification of an event highly depends on the shower arrival direction.

Although in presence of clouds which fullfill the "maximum development visibility" the geometry reconstruction can be achievable, its resolution is worse than the one of a similar event taking place in a clear atmosphere. For instance, in a clear atmosphere a $\theta = 60^\circ$ EAS extends $\sim 3^\circ$ in the Focal Plane (FP) and lasts 60 GTUs (150μs). The same EAS in presence of an optically thick cloud at 3 km only extends $\sim 2^\circ$ in the FP and lasts 40 GTUs. Then, this event which takes place under cloudy conditions would have a similar resolution than an EAS produced in clear sky of a lower zenith angle ($\sim 50^\circ$).

To investigate more in detail how the detected EAS signal is affected by the presence of clouds when an event occurs, we have used a 3D atmospheric model to develop a photon propagation model, which do not propagate each single photon, but packages of photons. The main contribution for fluorescence light will be from photons that are emitted in the telescope direction, since it is emitted isotropically. Cherenkov photons, on the other hand, are emitted very collimated along the path of the shower. Therefore, scattered photons will arrive to the telescope much more likely than photons directly emitted to JEM-EUSO. The main purpose of this propagation model is to be implemented in a near future inside a shower generation program to perform a deeper study on the influence of the atmosphere in the EAS detection.

To reconstruct the energy and X_{max} of EAS events in presence of stratus-like clouds, algorithms meant for a clear atmosphere have been modified. The energy reconstruction in stratus-like cases is acceptable and similar for *Cherenkov method* and *slant depth method*, although it gets worse for small zenith angles. For example, for $\theta = 30^\circ$ and H_c =3 km the accuracy on the reconstructed energy is almost 4 times worse than the one for the same cloud but an EAS of $\theta = 60^\circ$. For larger θ the accuracy is very good. The X_{max} determination is more sensitive to the geometry of the shower. When the chosen method is the slant depth method, which relies on the arrival direction obtained by the direction reconstruction algorithms, showers whose X_{max} is near H_c, have a worse X_{max} reconstruction. For a $\theta = 45^\circ$ EAS (whose shower maximum is located at ~ 4.5 km) in

presence of a cloud with $H_c = 4.5$ km we obtain a resolution error of $\sim 50\%$. Then, we should not use this method to reconstruct the shower maximum of events whose shower maximum is very near to a cloud. When the selected method is the Cherenkov method, which assumes the identification of a Cherenkov mark in the signal, the resolution of X_{max} gets worse for more horizontal EAS in presence of low clouds. The reason is that for those cases the Cherenkov bump is more diffuse and difficult to identify with a good resolution. Regarding the primary energy, when it is lower than 10^{20} eV (for instance, $5{\cdot}10^{19}$ eV), the signal of the shower is weaker; less photons arrive to the detector, and the resolution of the reconstruction decreases. When the primary energy is higher than 10^{20} eV (for instance, $3{\cdot}10^{20}$ eV) the shower develops deeper in the atmosphere. Therefore, their shower maxima take place lower in the atmosphere. Then, events whose shower maxima would be located above but very near to H_c for lower energies, might have their maxima inside the cloud now. The resolution in the cases also gets worse. Then, we conclude that these reconstruction algorithms are optimized for the energy 10^{20} eV.

Appendix A

Summary

A.1 Introduction

Ultra High Energy Cosmic Rays (UHECRs) and Extremely High Energy Cosmic Rays (EHECRs) are the most energetic particles in the Universe. They cannot be measured directly. However, they can be measured by the observation of the cascades of secondary particles, called Extensive Air Showers (EAS), produced when cosmic rays interact with atmospheric particles. These EAS produce fluorescence and Cherenkov light that can be detected by cosmic ray telescopes. Electrons and positrons from the secondary cascade (which carry $\sim 90\%$ of the initial energy) excite nitrogen molecules from the atmosphere. When these molecules are de-excited, fluorescence light is emitted isotropically. This emission depends on pressure, on temperature and on the steam content in air. The EAS secondary particles travel faster than the speed of light in air. As a result, they induce the emission of Cherenkov light in a narrow, forward-beamed cone.

Cosmic rays suffer a certain deflection due to the galactic and extragalactic magnetic field. However, at the highest energies this deflection is negligible. Then, tracing back their trajectory, their can be investigated. The current models to explain the acceleration of UHECRs can be divided in two groups: bottom-up models, which consider the UHECRs to be accelerated by astrophysical objects (i.e., active galactic nuclei or gamma ray bursts),

and top-down models, which propose more exotic theories (such as the decay of super heavy dark matter or unknown particles emitted by topological defects). Since the flux of cosmic rays at such high energies is extremely small, a very large collected area is needed. Therefore, a space-based telescope is required to study these particles.

JEM-EUSO (the Extreme Universe Space Observatory onboard the Japanese Experiment Module) is a novel space mission that will be launched in 2019 and located on the International Space Station (ISS). Looking down to the Earth from space, it utilizes the atmosphere as a detector of EAS with the aim of significantly increasing the exposure to UHECRs compared to the largest ground-based air shower arrays. It focuses on the UV (290-430 nm) fluorescence and Cherenkov EAS light. There are three JEM-EUSO pathfinders at different stages (either functioning or under construction): EUSO-Balloon, EUSO-TA and Mini-EUSO. The objectives of these pathfinder missions are: to perform a full scale end-to-end test of the JEM-EUSO concept and key technologies, to test the electronic components in stratospheric conditions, and to measure the UV background at high altitudes. The main telescope is a digital camera with a wide Field of View (FoV) of 60°. It consists of four principal parts: the photon collecting optics, the focal surface (FS) detector, the electronics, and the mechanical structure. Since JEM-EUSO FoV covers a wide observation area, different atmospheric conditions will take place at the same time inside the FoV. Therefore, an Atmospheric Monitoring System (AMS) is needed to inspect the properties of the atmosphere where the EAS occurs. The goal of the JEM-EUSO AMS is to provide information on the distribution and properties of the atmosphere features (such as cloud or aerosol layers) within the telescope FoV. The two main AMS devices are a bispectral IR camera and a LIDAR (LIght Detection And Ranging device).

A.2 Objectives

The main objective of this thesis is to understand how the EAS produced by UHECRs are detected by the JEM-EUSO telescope under different atmospheric conditions. Specially, we analyze how the detection of showers with different initial energies and arrival direc-

tions are affected by the presence of clouds of diverse cloud top heights and optical depths in the JEM-EUSO FoV. Also, we modify the energy and shower maximum reconstruction algorithm so it can be used in presence of stratus-like clouds located below the shower maximum.

A.3 Results

To provide a full set of tools for EAS simulation, reconstruction and analysis for space-based cosmic observations, an official JEM-EUSO software is being developed by the JEM-EUSO Collaboration. This software is named ESAF (EUSO Simulation and Analysis Framework). EAS photons arriving to the telescope are observed as a spot moving at the speed of light. The number of photons detected by the telescope as a function of time will depend on the type of primary particle, its energy and the arrival direction of the shower. Besides the physical parameters of the event, the number of detected photons, their arrival time to the detector and the resolution of the obtained image also decrease with the distance of the detecting pixel to the center of the FoV. The number of detected photons is influenced by three factors: the distance between the telescope and the emission location, the solid angle subtended by JEM-EUSO to the observed position, and the attenuation produced in the propagation of the photons to the telescope through the atmosphere. Another point we need to consider when an event detected by JEM-EUSO is analyzed is that one pixel at the edge of the focal surface has a lower resolution than another at the center of the FoV. This is clear, since pixels at the edge subtend a higher observation area than pixels near the center. In modern large telescopes a lot of effort is put into reducing the size of the Point Spread Function (PSF). The PSF describes the two-dimensional distribution of light in the telescope focal plane for astronomical point sources. For JEM-EUSO, the optical system is optimized (gives a lower PSF) for wavelengths around 350 nm.

The accuracy in the determination of EAS parameters strongly depends on atmospheric conditions. These conditions alter the development and the detection of EAS.

Therefore, the amount of clouds (fractional cover) and the distribution of clouds in term of cloud height and optical depth would also affect the JEM-EUSO duty cycle. For instance, clouds with large optical depth ($\tau_c > 1$) produce a very high scattered Cherenkov peak. If the cloud is low enough, the detected signal is similar than that for the clear sky case. Directed fluorescence signal is little affected by the cloud (because the majority of the shower will develop above the cloud), and the Cherenkov light will be reflected on the top of the cloud, giving a brighter Cherenkov signal than the one that would have been reflected on ground. However, the EAS signal which develops after the cloud will be lost and the shower development cannot be enterely observed. If clouds are optically thin ($\tau_c < 1$), the shower light suffers an attenuation as $e^{-\tau_c}$, so their effect on the trigger is not significant. The fraction of events that fulfill the *maximum development visibility* requirement (either events in presence of clouds with $\tau_c < 1$ or those whose $H_c < H_{max}$) is almost constant for the highest energies ($E > 3 \cdot 10^{19}$ eV) at accounts for $\sim 72\%$. The effect of clouds on the energy estimation strongly depends on the zenith angle of the shower. In ESAF the clouds can be only considered as an uniform and homogeneous layer. Then, we have developed a 3D photons propagation module. Since the fluorescence is emitted isotropically, JEM-EUSO is located at an altitude of 400 km and its size is only a few meters, the probability of fluorescence scattered photons reaching the telescope is very low. Then, we have only considered as a first step that only direct fluorescence photons arrive to the detector. Cherenkov photons, on the other hand, are emitted in a beamed-forward direction along the shower track. Then, direct Cherenkov photons are very unlikely to reach the telescope. As a first approximation, we have only considered scattered photons at first order.

The atmospheric conditions also have to be considered when the EAS parameters are reconstructed. The purpose of our work is to analyze how the energy and shower maximum reconstruction are influenced by the presence of stratus-like clouds (optically thick clouds). We have modified the two reconstruction methods meant for events produced in a clear atmosphere. The *Cherenkov method* relies on the determination of the Cherenkov reflected bump on the top of the cloud. The *slant depth method* relies on the angular reconstruction

of the shower track for the shower development produced before the cloud. For the energy reconstruction at standard energies (10^{20}eV) with both cases the results are similar and acceptable. However, it gets worse for small zenith angles. These showers develop deeper in the atmosphere, so their detection is highly influenced even by low clouds. When we reconstruct the shower maximum, which is more sensitive to the shower geometry, the results slightly depend on the method. For the slant depth method showers whose maximum occurs at an altitude near the cloud top height, we get a worse shower maximum reconstruction. For the Cherenkov method, the resolution gets worse for those cases whose Cherenkov bump is more diffuse and difficult to identify with a good resolution, i.e., for large zenith angle showers. When we decrease the primary energy (i.e., $5{\cdot}10^{19}$ eV), the shower signal is weaker and less photons arrive to the detector. If we increase the primary energy (i.e., $3{\cdot}10^{20}$eV), the shower develop deeper in the atmosphere and their shower maxima take place lower in the atmosphere.

A.4 Conclusions

Showers with large zenith angle θ produce a larger signal in time and higher number of photons than showers with lower θ. An EAS of $\theta = 75°$ will start to develop at an altitude of $\sim$ 20 km and will reach its maximum development at $\sim$ 12 km. An EAS of $\theta = 30°$ will start its development at $\sim$ 8 km, reaching its maximum at $\sim$ 2 km (deeper in the atmosphere than the previous case). The EAS development also depends on the primary particle. While a proton-induced shower at $\theta = 60°$ reaches its maximum 25GTUs after the shower starts to develop, an iron-induced shower at the same zenith angle reaches its maximum 35GTUs after the beginning of the EAS development. We also need to consider their location in the JEM-EUSO FoV. For example, a shower with a primary energy of 10^{20} eV and a zenith angle of $\theta = 60°$ with an angular distance to the center of the FoV $\gamma = 15°$ (with a duration of $\sim$ 50 GTUs), will suffer a shortening in its shower track by a factor of $\sim$ 17% when it is compared with the same EAS landing at the center of the FoV (whose time difference is $\sim$ 60GTUs). The number of detected photons per pixel

depends on the distance to the telescope, the atmospheric attenuation and the subtended solid angle from JEM-EUSO to the emission point. The solid angle of an EAS landing at $\gamma = 15^\circ$ will be 1.12 times larger than the solid angle for $\gamma = 0$.

We have defined the cloud efficiency, which is the fraction of events that fulfill the maximum development visibility requirements (events in presence of clouds with $\tau_c < 1$ or those with $H_c < H_{max}$), over the ones triggering in clear-sky conditions. This cloud efficiency is almost constant for the highest energies and accounts for $\sim 72\%$ of the trigger EAS. In presence of clouds the geometry reconstruction can be achievable, however, the resolution is worse than that for a clear atmosphere. For instance, in clear atmosphere a $\theta = 60^\circ$ EAS extends $\sim 3^\circ$ in the Focal Plane and lasts 60 GTUs (150 μs). The same EAS in presence of an optically thick cloud at 3 km, only extends $\sim 2^\circ$ in the Focal Plane and lasts 40 GTUs. Then, this event which takes place under cloudy conditions would have a similar resolution than an EAS produced in clear sky of a lower zenith angle.

The energy reconstruction in stratus-like cases is acceptable and similar for Cherenkov method and slant depth method, although it gets worse for small zenith angles. For $\theta = 30^\circ$ and $H_c = 3$ km the resolution is almost 4 times worse than the resolution for the same cloud but an EAS of $\theta = 60^\circ$. For the highest cloud we have considered ($H_c = 7.5$ km), at $\theta = 75^\circ$ we only have an relative error of 20%. For the shower maximum reconstruction, the results depend on the method. The shower maximum is more sensitive to the geometry of the shower, so the resolution for both methods is worse for those showers whose geometry is more difficult to reconstruct. Both methods are optimized for the standard energy: 10^{20}eV.

Appendix B

Resumen

B.1 Introducción

Los Rayos Cósmicos de Ultra Alta Energía (UHECRs) y los Rayos Cósmicos de Extremadamente Alta Energía (EHECRs) son las partículas más energéticas del Universo. Aunque no pueden ser medidas directamente, sí pueden detectarse las cascadas secundarias de partículas (EAS) que producen cuando interaccionan con partículas de la atmósfera. Estas EAS producen luz de fluorescencia y Cherenkov que pueden ser detectadas por telescopios de rayos cósmicos. Cuando los electrones y positrones provenientes de estas cascadas secundarias (que llevan $\sim 90\%$ de la energía inicial) interaccionan con el nitrógeno atmosférico, lo excitan. Este nitrógeno más tarde se desexcita, emitiendo luz de fluorescencia de manera isótropa, que depende de la presión, temperatura y contenido de vapor en la atmósfera. Además, estas partículas secundarias viajan más rápido que la velocidad de la luz en la atmósfera. Por eso, inducen una emisión de luz Cherenkov en un estrecho cono en la dirección de propagación de la cascada.

Los rayos cósmicos sufren una cierta deflexión debido al campo magnético galáctico y extragaláctico. Sin embargo, a tan altas energías esa deflexión es despreciable. Por tanto, sabiendo la trayectoria que ha llevado el rayo cósmico en su llegada a la atmósfera, puede investigarse su origen. Los modelos actuales que explican la aceleración de los

UHECRs pueden dividirse en dos grupos: los modelos *bottom-up*, que consideran que el origen de la aceleración es una fuente astrofísica (por ejemplo, núcleos de galaxias activas o estallidos de rayos gamma), y los modelos *top-down*, que proponen un origen más exótico (como el decaimiento de materia oscura super pesada o la emisión de partículas desconocidas por defectos topológicos). Como el flujo de rayos cósmicos a tan altas energías es extremadamente pequeño, se necesitan telescopios que proporcionen un área de observación muy grande. Por eso, la construcción de un telescopio espacial es crucial para el estudio de estas partículas.

JEM-EUSO (el observatorio espacial del Universo extremo a bordo del módulo experimental japonés) es una misión espacial moderna que será lanzada al espacio en pocos años, y será colocada en la estación espacial internacional (ISS). Mirando desde el espacio hacia la Tierra, utilizará la atmósfera como calorímetro para detectar las EAS producidas por UHECRs con el propósito de incrementar de manera significativa la exposición a los UHECRs en comparación con los telescopios para EAS en Tierra. JEM-EUSO detectará la luz de fluorescencia y Cherenkov, centrándose en la banda ultravioleta (de 290 a 430 nm). Hay tres precursores de JEM-EUSO en diferentes estadios de desarrollo (aún en construcción o ya funcionando): EUSO-Balloon, EUSO-TA y Mini-EUSO. Los objetivos de estos precursores son: comprobar que la tecnología novedosa de JEM-EUSO funciona, comprobar el funcionamiento de los componentes electrónicos en condiciones estratosféricas y medir el ruido de fondo en el UV a grandes altitudes. El telescopio principal es una cámara digital con un amplio campo de visión (FoV) de 60°. Está formando por cuatro partes principales: la óptica, el detector, la electrónica y la estructura mecánica. Debido a su amplia área de observación, diferentes condiciones atmosféricas tendrán lugar de manera simultánea en el FoV del telescopio. Por tanto, que el telescopio posea un sistema de monitoreo atmosférico (AMS) es crucial para poder medir correctamente las propiedades de la atmósfera en el momento en el que un evento tenga lugar. El principal objetivo del AMS de JEM-EUSO es proveer información de la distribución y propiedades de las nubes o de las capas de aerosoles que se encuentren en el campo de visión del telescopio. El AMS consta fundamentalmente de dos instrumentos: una cámara infrarroja biespectral,

y un LIDAR (LIght Detection And Ranging device).

B.2 Objetivos

El objetivo principal de esta tesis es entender cómo las cascadas secundarias de partículas producidas por los Rayos Cósmicos de Ultra Alta Energía son detectadas por el telescopio JEM-EUSO bajo distintas condiciones atmosféricas. Especialmente, analizamos cómo la detección de lluvias con diferentes energías iniciales y direcciones de llegada son afectadas por la presencia de nubes de diversas alturas y profundidades ópticas en el campo de visión de JEM-EUSO. Además, modificamos el algoritmo de reconstrucción de energía y el de reconstrucción del máximo de la lluvia para que puedan utilizarse en presencia de nubes tipo estrato que se encuentren situadas bajo del máximo de la lluvia.

B.3 Resultados

La colaboración de JEM-EUSO está desarrollando un programa que provee las herramientas necesarias para la simulación, reconstrucción y análisis de EAS desde observaciones realizadas por telescopios de rayos cósmicos espaciales, llamado ESAF. La luz que llega al telescopio se observa como un punto que se mueve a la velocidad de la luz. El número de fotones detectados en función del tiempo depende del tipo de partícula primaria, su energía y su dirección de llegada. El número de fotones, su tiempo de llegada y la resolución de la imagen que producen no solo depende de los parámetros físicos del evento, sino que todos decrecen conforme aumenta la distancia desde donde han sido detectados al centro del FoV. El número de fotones detectados está influenciado por tres factores: la distancia desde el telescopio al lugar de emisión del fotón, el ángulo sólido subtendido desde JEM-EUSO al lugar de emisión, y la atenuación producida en la propagación de fotones hasta el telescopio a traves de la atmósfera. Un efecto más a considerar cuando un evento detectado por JEM-EUSO es analizado, es que un pixel perteneciente al centro de la superficie focal tiene una resolución mayor que uno menos centrado. Esto es evi-

dente, ya que a los pixels alejados abarcan un área de observación mayor. En los grandes telescopios modernos se realiza un importante esfuerzo para reducir la función de difusión del punto (PSF). La PSF describe una distribución bidimensional de luz en el plano focal del telescopio para fuentes astronómicas puntuales. Para JEM-EUSO, el sistema óptico está optimizado (se obtiene una menor PSF) para longitudes de ondas alrededor de los 350 nm.

La precisión en la determinación de los parámetros de las EAS dependen de manera considerable de las condiciones atmósfericas. Estas condiciones afectan el desarrollo y la detección de las cascadas. Por tanto, la superficie cubierta por nubes y la distribución de estas en términos de altura y profundidad óptica también afectará al tiempo efectivo de observación de JEM-EUSO. Por ejemplo, para nubes que tienen una alta profundidad óptica ($\tau_c > 1$) y son lo suficientemente bajas, la señal detectada es similar a la que se produciría en cielo claro. La señal de fluorescencia directa se ve pobremente afectada por las nubes (porque la mayor parte de la lluvia se desarrolla por encima de la nube), y la luz de Cherenkov se ve reflejada en la parte alta de la nube, produciento una señal más marcada que la que se reflejaría en la superficie terrestre. Sin embargo, la parte de la señal de la EAS que se desarrolla después de la nube no será detectada. Si la nube es ópticamente fina ($\tau_c < 1$), la luz de la cascada sufrirá una atenuación proporcional a $e^{-\tau_c}$, por lo que su efecto en el disparador no será significativo. La fracción de eventos que cumple el requisito de visibilidad del máximo del desarrollo (eventos en presencia de nubes de $\tau_c < 1$ o con alturas $H_c < H_{max}$) es prácticamente constante para altas energías ($E > 3 \cdot 10^{19}$ eV) y tiene un valor de $\sim 72\%$. El efecto de las nubes en la estimación de la energía es muy dependiente del ángulo de llegada de la cáscada. En ESAF las nubes pueden ser únicamente incluidas como capas uniformes y homogéneas. Por tanto, hemos desarrollado un modelo de propagación de fotones en una atmósfera tridimensional. Como la luz de fluorescencia se emite de manera isótropa, JEM-EUSO se encuentra a una altura de 400 km y sus dimensiones son de unos pocos metros, la probabilidad de que lleguen al telescopio fotones de fluorescencia dispersados es muy baja. Por tanto, como primera aproximación consideramos que solamente llegan aquellos que son directamente emitidos

en dirección al telescopio. Los fotones Cherenkov, por otro lado, se emiten en un estrecho cono en la dirección de la lluvia. El número de fotones Cherenkov emitidos en dirección a JEM-EUSO es despreciable. Por eso, consideramos que los fotones que llegan al telescopio son los dispersados a primer orden.

Es importante considerar las condiciones atmosféricas para reconstruir los parámetros de las EAS. El propósito de este trabajo es analizar cómo la reconstrucción de la energía y del máximo de la lluvia son afectados por la presencia de nubes tipo estrato (nubes de profundidad óptica alta). Hemos modificado los dos métodos de reconstrucción desarrollados para cielo despejado. El *método Cherenkov* se basa en la determinación del pico producido por la luz Cherenkov reflejada en la parte superior de la nube. El *método slant depth* se basa en la reconstrucción angular de la parte de la lluvia situada por encima de la nube. Para la reconstrucción de la energía obtenemos resultados similares y aceptables para ambos métodos. Aún así, la precisión es peor para cascadas más verticales. La razón es que se desarrollan en las partes más bajas de la atmósfera y de manera más rápida, por lo que son afectadas incluso por las nubes más bajas. Cuando reconstruimos el máximo de la lluvia, que es más sensible a la geometría de la misma, los resultados claramente dependen del método utilizado. Para el método slant depth, cascadas cuyo máximo se encuentre a alturas cercanas a la altura superior de la nube nos dan una peor reconstrucción. Para el método Cherenkov la resolución empeora para casos cuya señal de Cherenkov es más difusa y difícil de identificar con una buena precisión; es decir, para cascadas con ángulos de llegada mayores. Cuando la energía del primario es más baja (por ejemplo, $5 \cdot 10^{19}$ eV), la señal producida es más débil y menos fotones llegan al detector. Si incrementamos la energía del primario (por ejemplo, $3 \cdot 10^{20}$eV), la cascada se desarrolla en capas de la atmósfera más profundas, por lo que su máximo tiene lugar a una altura menor.

B.4 Conclusiones

Las lluvias con grandes ángulos cenitales (θ) producen una señal más duradera y un número mayor de fotones que las lluvias con θ menores. Un EAS de $\theta = 75°$ empezará a desarrollarse a una altura de ~ 20 km, y alcanzará su máximo desarrollo a ~ 12 km. Una lluvia de $\theta = 30°$ empezará su desarrollo a ~ 8 km, alcanzando su máximo a ~ 2 km (en capas de la atmósfera más profundas). El desarrollo de la EAS también depende de la partícula primaria. Mientras que una lluvia inducida por un protón alcanza su máximo 25 GTUs después del inicio de su desarrollo, un EAS inducida por un hierro con el mismo θ alcanza su máximo 35GTUs después del comienzo de su desarrollo. Para analizar una lluvia también tenemos que considerar su localización en el FoV. Por ejemplo, una lluvia de energía primaria 10^{20} eV y ángulo cenital $\theta = 60°$ con una distancia angular $\gamma = 15°$ (con una duración de $\sim$ 50GTUs) sufrirá un acortamiento en su trayectoria en el FoV en un factor de $\sim 17\%$ comparada con una lluvia que sucede en el centro (cuya duración es de $\sim$ 60GTUs). El número de fotones detectados por pixel también depende de la distancia al telescopio, la atenuación atmosférica y el ángulo sólido subtendido. Este ángulo sólido para una lluvia que impacta a $\gamma = 15°$ sera 1.12 veces mayor que el correspondiente a $\gamma = 0°$. Hemos definido la eficiencia nubosa, que es la fracción de eventos que cumplen el requisito de visibilidad del máximo desarrollo (eventos en prensecia de nubes con $\tau_c < 1$ o aquellas tales que $H_c < H_{max}$), en relación a las que activarían el disparador en condiciones de atmósfera libre de nubes. Esta eficiencia nubosa es constante para las más altas energías y tiene un valor de $\sim 72\%$.

En presencia de nubes la geometría de la lluvia puede ser reconstruida, aunque su resolución sea peor que en el caso de una atmósfera clara. Por ejemplo, en cielo despejado una lluvia de $\theta = 60°$ ocupa $\sim 3°$ en el plano focal y dura 60 GTUs (150 μs). La misma lluvia en presencia de una nube de profundidad óptica elevada a 3 km solo ocupa $\sim 2°$ y dura 40 GTUs. Por tanto, un evento en presencia de nubes tendrá una resolucion similar que un evento producido en atmósfera despejada de menor ángulo cenital. La reconstrucción de la energía es aceptable y similar para el método Cherenkov y el método

slant depth. Aún así, empeora para pequeños ángulos cenitales. Para una lluvia de $\theta = 30°$ y $H_c = 3$ km la resolución es casi 4 veces peor que la resolución para la misma nube y una lluvia de $\theta = 60°$. Para una nube alta de $H_c = 7.5$ km y una lluvia a $\theta = 75°$ solo tenemos un error relativo de 20%. En la reconstrucción del máximo de la lluvia, los resultados dependen del método utilizado. El máximo de la lluvia es más sensible a la geometría de la lluvia, por lo que la resolución para ambos casos es peor para aquellas lluvias en las que la geometría no se puede reconstruir con suficiente precisión. Ambos métodos están optimizados para la energía estándar: 10^{20}eV.

Bibliography

[1] Gaisser, T.K. . *Cosmic Rays and Particle Physics*. Cambridge Univ. Press, 1990.

[2] Adams, J.H. et al. An evaluation of the exposure in nadir observation of the JEM-EUSO mission. *Astropart.Phys.*, 44:76–90, 2013.

[3] The JEM-EUSO Collaboration. The JEM-EUSO Mission: Contributions to the ICRC 2013. *Proc. of 33rd International Cosmic Ray Conference (ICRC), Rio de Janeiro, Brazil. ArXiv:1307.7071*, July 2013.

[4] The JEM-EUSO Collaboration (corresponding authors: Morales de los Rios, J. A. & Rodríguez Frías, M. D.). Towards the Preliminary Design Review of the Infrared Camera of the JEM-EUSO Space Mission. *Experimental Astronomy*, 37, 2014.

[5] Rodríguez Frías, M.D., Toscano, S., Bozzo, E., del Peral, L., Neronov, A., and Wada, S. for the JEM-EUSO Collaboration. The Atmospheric Monitoring System of the JEM-EUSO Space Mission. *Proceedings of the 2nd AtmoHEAD Conference, Padova (Italy) May 19-21, 2014, ArXiv:1501.04821*, January 2015.

[6] Sáez-Cano, G., Shinozaki, K., del Peral, L., Bertaina, M. and Rodríguez Frías, M.D. for the JEM-EUSO Collaboration. Observation of extensive air showers in cloudy conditions by the JEM-EUSO Space Mission. *Adv.Space Res.*, 53:1536–1543, 2014.

[7] Wilkinson, C.R. The Application of High Precision Timing in the High Resolution Fly's Eye Cosmic Ray Detector. *PhD. Thesis, www.cosmic-ray.org/thesis/wilkinthesis.pdf*, 1998.

[8] Pierre Auger Collaboration. Pierre auger observatory webpage. *http://www.auger.org*, 2009.

[9] Muller, D. Direct observations of galactic cosmic rays. *Eur.Phys.J.*, H37:413–458, 2012.

[10] Biermann, P. L. and Sigl, G. Introduction to Cosmic Rays. In *Physics and Astrophysics of Ultra-High-Energy Cosmic Rays*, volume 576 of *Lecture Notes in Physics, Berlin Springer Verlag*, 2001.

[11] Watson, A. A. High-Energy Cosmic Rays and the Greisen-Zatsepin-Kuz'min effect. *Rept.Prog.Phys.*, 77:036901, 2014.

[12] Sigl, G. *Physics and Astrophysics of Ultra High Energy Cosmic Rays*. Lecture Notes in Physics. Springer, 2010.

[13] Waldenmaier, T. Spectral resolved Measurement of the Nitrogen Fluorescence Yield in Air induced by Electrons. *PhD. Thesis. bibliothek.fzk.de/zb/berichte/FZKA7209.pdf*, Universitat Karlsruhe, 2006.

[14] California Institute of Technology. Space Radiation Lab at California Institute of Technology webpage. *http://www.srl.caltech.edu/*, 2015.

[15] Ptuskin, V., Rogovaya, S. and Zirakashvili, V. On Ultra-High Energy Cosmic Rays: origin in AGN jets and transport in expanding Universe. *Adv.Space Res.*, 51:315–321, 2013.

[16] Bauleo, P. M. and Martino, J. R. The dawn of the particle astronomy era in Ultra-High-Energy Cosmic Rays. *Nature*, 458N7240:847–851, 2009.

[17] Gabici, S. Cosmic ray escape from supernova remnants. *Mem.Soc.Ast.It.*, 82:760. Arxiv:1108.4844, 2011.

[18] Kim, H. B. and Kim, J. Revisit of Correlation Analysis Between Active Galactic Nuclei and Ultra-High Energy Cosmic Rays. *International Journal of Modern Physics D*, 22:50045, July 2013.

[19] Kim, J. and Kim, H. B. Correlation between Ultra-High Energy Cosmic Rays and Active Galactic Nuclei from the Fermi large-area telescope. *Journal of Korean Physical Society*, 61:1911–1917, December 2012.

[20] A. M. Hillas. The Origin of Ultra-High-Energy Cosmic Rays. *Annual review of Astronomy and Astrophysics*, 22:425–444, 1984.

[21] Pugliese, G. and Falcke, H. and Biermann, P. L. A jet-disk symbiosis model for Gamma Ray Bursts: SS 433 the next? *Astronomy and Astrophysics*, 344:L37–L40, April 1999.

[22] Stanev, T. Ultra High Energy Cosmic Rays. In Z. Parsa, editor, *Intersections of Particle and Nuclear Physics*, volume 698 of *American Institute of Physics Conference Series*, pages 357–361, February 2004.

[23] Ros, G. Composition and energy determination in cosmic ray surface arrays: an application to the Pierre Auger Observatory. *PhD. Thesis at University of Alcalá. http://dspace.uah.es/dspace/handle/10017/6402*, 2009.

[24] Thea, A. Osservazione di radiazione cosmica di altissima energia dallo spazio. *PhD. Thesis*, Universitàt degli Studio di Genova. www.ge.infn.it/euso/docs/AThea_PhDThesis.pdf, 2006.

[25] Yoshida, S. and Teshima, M. Energy Spectrum of Ultra-High Energy Cosmic Rays with Extra-Galactic Origin. *Progress of Theoretical Physics*, 89:833–845, April 1993.

[26] Monasor, M. Energy calibration of the Pierre Auger Observatory. Measurement of the spectrum of Ultra-High Energy Cosmic Rays. *PhD. Thesis at Universidad de Alcalá. Internal Auger Note (GAP) 2008-167.*, 2008.

[27] Grojean, C. and Spiropulu, M. High-energy physics. Proceedings, 5th CERN-Latin-American School, Recinto Quirama, Colombia, March 15-28. 2010.

[28] Gaisser, T. K. and Stanev, T. and Tilav, S. Cosmic ray energy spectrum from measurements of air showers. *Frontiers of Physics*, 8:748–758, December 2013.

[29] Pesce, R. The detection of Ultra High Energy Cosmic Particles on the earth and from space. *PhD. Thesis. www.ge.infn.it/∼pesce/phd/PhDThesis.pdf*, Universitàt degli Studio di Genova, 2008.

[30] Nakamura, K. et al (Particle Data Group). Cosmic rays. *Journal of Physics G: Nuclear and Particle Physics*, 2010.

[31] Swinburne University. The SAO enciclopedy of Astronomy. *http://astronomy.swin.edu.au/cosmos/C/Cosmic+Ray+Energies*, 2014.

[32] Berezinsky, V. and Gazizov, A.Z. and Grigorieva, S.I. On astrophysical solution to ultrahigh-energy cosmic rays. *Phys.Rev.*, D74:043005, 2006.

[33] Abbasi, R.U. et al. First observation of the Greisen-Zatsepin-Kuzmin suppression. *Phys.Rev.Lett.*, 100:101101, 2008.

[34] Kampert, K.H. and Watson, A.A. Extensive Air Showers and Ultra High-Energy Cosmic Rays: A Historical Review. *Eur.Phys.J.*, H37:359–412, 2012.

[35] Abu-Zayyad, T. et al. A measurement of the average longitudinal development profile of cosmic ray air showers between 10^{17} and ^{18} eV. *Astroparticle Physics*, Volume 16:1–11, 2001.

[36] Watson, A.A. Extensive Air Showers and Ultra High Energy Cosmic Rays. *Lectures given at a Summer School in Mexico*, 2002.

[37] Matt Strassler. Conversations about science with theoretical physicist matt strassler. *http://profmattstrassler.com/articles-and-posts/particle-physics-basics/cerenkov-radiation/*, 2014.

[38] Abu-Zayyad, T. The energy spectrum of Ultra-High Energy Cosmic Rays. *PhD. www.telescopearray.org/media/papers/tareq_thesis.pdf*, University of Utah, 2000.

[39] Longair,M.S. *High energy astrophysics*. Cambridge Univ. Press, 1994.

[40] Rao, M.V.S. and Sreekantan, B.V. *Extensive Air Showers*. World Scientific, 1998.

[41] Giller, M. and Wiczorek, G. Similarity of the extensive air showers - an application to their reconstruction from a fluorescence light detector. *International Cosmic Ray Conference*, 7:199, 2005.

[42] Giller, M. and Kacperczyk, A. and Malinowski, J. and Tkaczyk, W. and Wieczorek, G. Similarity of extensive air showers with respect to the shower age. *J.Phys.*, G31:947–958, 2005.

[43] Semikoz, D. High-energy astroparticle physics. *CERN Yellow Report CERN-2010-001, 363-393. arXiv:1010.2647*, 2010.

[44] Matthews, J. A Heitler model of extensive air showers. *Astropart.Phys.*, 22:387–397, 2005.

[45] Anchordoqui, L., Paul, T. C., Reucroft, S. and Swain, J. Ultra High-Energy Cosmic Rays: The State of the art before the Auger Observatory. *Int.J.Mod.Phys.*, A18:2229–2366, 2003.

[46] Glushkov, A.V., Makarov, I.T., Pravdin, M.I., Sleptsov, I.E., Gorbunov, D.S. et al.. Muon content of ultrahigh-energy air showers: Yakutsk data versus simulations. *JETP Lett.*, 87:190–194, 2008.

[47] Zas, E. A New approach to mass measurements of UHECR: Horizontal Air Showers. *AIP Conf.Proc.*, 566:301–316, 2001.

[48] Kajita, T. Atmospheric neutrinos. *Adv.High Energy Phys.*, 2012:504715, 2012.

[49] Gaisser, T. K. Atmospheric Neutrinos. *AIP Conf.Proc.*, 944:140–142, 2007.

[50] Sinegovskaya, T.S., Ogorodnikova, E.V. and Sinegovsky, S.I. High-energy fluxes of atmospheric neutrinos. *33rd International Cosmic Ray Conference. ArXiv:1306.5907*, 2013.

[51] Bertaina, M. et al. Performance and air-shower reconstruction techniques for the JEM-EUSO mission. *Adv.Space Res.*, 53:1515–1535, 2014.

[52] Sokolsky, P. and Thomson, G.B. Highest Energy Cosmic Rays and results from the HiRes Experiment. *J.Phys.*, G34:R401, 2007.

[53] Institute for Cosmic Ray Research University of Tokyo, Japan. The Akeno Observatory webpage. *http://www-akeno.icrr.u-tokyo.ac.jp/AGASA/*, 2003.

[54] Bellido, J.A. and Clay, R.W. and Dawson, B.R. and Johnston-Hollitt, M. Southern hemisphere observations of a 10^{18} eV cosmic ray source near the direction of the galactic center. *Astropart.Phys.*, 15:167–175, 2001.

[55] Baltrusaitis, R., Cassiday, G. L., Cooper, R., Dawson, B. R., Elbert, J. W., Fick, B. E.,. Search for Deeply Penetrating Particles in Extensive Air Showers above 10^{17} eV. *Proc. of the 20th International Cosmic Ray Conference Moscow.*, 6:365–369, 1987.

[56] Sokolsky, P. and Thomson, G. B. TOPICAL REVIEW: Highest energy cosmic-rays and results from the HiRes experiment. *Journal of Physics G Nuclear Physics*, 34:401, November 2007.

[57] University of Utah. Ultra-high energy cosmic rays are from extremely far away, webpage. *http://www.sciencedaily.com/releases/2008/03/080321084612.htm*, 2008.

[58] Allen, M. G. Ultra High Energy Cosmic Ray Energy Spectrum and Composition using Hybrid Analysis with Telescope Array. *PhD Thesis. www.telescopearray.org/media/theses/mallen_thesis.pdf.*

[59] Allekotte, I. et al. The Surface Detector System of the Pierre Auger Observatory. *Nucl.Instrum.Meth.*, A586:409–420, 2008.

[60] Necesal, P. The Fluorescence Detector of the Pierre Auger Observatory (CALOR2010 Proceedings). *J.Phys.Conf.Ser.*, 293:012036, 2011.

[61] Kavli Institute for Cosmological Physics. Particles from space, webpage. *http://kicp.uchicago.edu/research/spaceparticles/*, 2014.

[62] T. Abu-Zayyad et al. Energy Spectrum of Ultra-High Energy Cosmic Rays Observed with the Telescope Array Using a Hybrid Technique. *Astropart.Phys.*, 61:93–101, 2015.

[63] The JEM-EUSO Collaboration. The JEM-EUSO Mission: Status and Prospects in 2011. *Proceedings of the 32nd International Cosmic Ray Conference, Beijing, China. ArXiv:1204.5065*, July 2011.

[64] National Aeronautics and Space Administration. International Space Station. *"https://earthkam.ucsd.edu/images/"*, 2014.

[65] European Space Agency. Space for Europe. *http://www.esa.int/ESA*, 2014.

[66] Skobeltsyn Institute of Nuclear Physics. Skobeltsyn Institute of Nuclear Physics webpage. *"http://uhecr.sinp.msu.ru/jem-euso/pathfinders"*, 2014.

[67] Italian JEM-EUSO Collaboration. Italian JEM-EUSO Collaboration webpage. *"http://jem-euso.roma2.infn.it/"*, 2014.

[68] SPace & AStroparticles Group. JEM-EUSO Spanish Collaboration webpage. *http://spas.uah.es/index.php/euso-balloon*, 2014.

[69] JEM-EUSO Naples Group. Napoli Web Site of the JEM EUSO Experiment. *http://www1.na.infn.it/wsubnucl/cosm/JemEuso/*, 2014.

[70] Rodríguez Frías, M. D. et al. for the JEM-EUSO Collaboration. The JEM-EUSO Space Mission: Frontier Astroparticle Physics at ZeV range from Space. *Homage to the Discovery of Cosmic Rays. Nova Science Publishers, New York, ISBN: 978-1-62618-998-0, Inc, Pg 201-212 (2013).*

[71] Rodríguez Frías, M. D. et al. for the JEM-EUSO Collaboration. The Atmospheric Monitoring System of the JEM-EUSO Space Mission. *Proc. International Symposium on Future Directions in UHECR Physics, The European Physical Journal*, 53:10005–pg1–7, 2013.

[72] The JEM-EUSO Collaboration (corresponding authors: Toscano, S., Morales de los Ríos, J. A., Neronov, A., Rodríguez Frías M. D., & Wada, S.). The Atmospheric Monitoring System of the JEM-EUSO instrument. *Experimental Astronomy*, 37, 2014.

[73] Sáez Cano, G., Morales de los Ríos, J. A., Shinozaki, K., Briz, S., Prieto, H., del Peral, L., Carretero, J. H., de Castro, A. J., Cortés, F., Lopez, F., Neromov, A., Wada, S., Rodríguez Frías, M. D. for the JEM-EUSO Collaboration. Observation of ultra-high energy cosmic rays in cloudy conditions by the space-based JEM-EUSO Observatory. *Journal of Physics Conference Series*, 375(5):052010, July 2012.

[74] Adams, J.H., Jr. and Christl, M.J. and Csorna, S.E. and Sarazin, F. and Wiencke, L.R. Calibration for Extensive Air Showers observed during the JEM-EUSO mission. *Adv.Space Res.*, 53:1506–1514, 2014.

[75] Adams, Jr, J. H. and Christl, M. J. and Csorna, S. E. and Sarazin, F. and Wiencke, L. R. Ground Truth calibration for the JEM-EUSO Mission. *ArXiv e-prints*, February 2013.

[76] Rodríguez Frías, M. D. et al. for the JEM-EUSO Collaboration. Towards the Preliminary Design Review of the Infrared Camera of the JEM-EUSO Space Mission. *Proc. of 33rd International Cosmic Ray Conference (ICRC), Rio de Janeiro, Brazil, ArXiv:1307.7071*, July 2013.

[77] Morales de los Ríos, J. A., Joven, E., del Peral, L., Reyes, M., Licandro, J., and Rodríguez Frías, M. D. The Infrared Camera Prototype Characterization for the JEM-EUSO Space Mission. *Nuclear Instruments and Methods NIMA*, 2014.

[78] Sáez-Cano, G. et al for the JEM-EUSO Collaboration. Observation of Ultra-High Energy Cosmic Rays in cloudy conditions by the JEM-EUSO Space Observatory. *Proceedings of the 32nd International Cosmic Ray Conference, Beijing, China. ArXiv:1204.5065*, July 2013.

[79] Abreu, P. et al. Description of Atmospheric Conditions at the Pierre Auger Observatory using the Global Data Assimilation System (GDAS). *Astropart.Phys.*, 35:591–607, 2012.

[80] Waldenmaier, T.,Blumer, J., Gonzalez, D.M. and Klages, H. Measurement of the air fluorescence yield with the AirLight experiment. *Nucl.Instrum.Meth.*, A597:67–74, 2008.

[81] SCHOTT consortium. SCHOTT webpage. *www.schott.com/advanced_optics/.*

[82] Keilhauer, B., Blumer, J., Klages, H.O. and Risse, M. Atmospheric effects on the development and the fluorescence detection of extensive air showers. *Proceedings of the 28th International Cosmic Ray Conference, Tsukuba, Japan*, pages 879–882, 2003.

[83] Watson, A. A. The Discovery of Cherenkov Radiation and its use in the detection of extensive air showers. *Nucl.Phys.Proc.Suppl.*, 212-213:13–19, 2011.

[84] SterreKundeKlub Hermanus Astronomy Center. Astronomy Center. *http://www.hermanusastronomy.co.za/*, 2014.

[85] Berat, C., Bottai, S., De Marco, D., Moreggia, S., Naumov, D. et al. ESAF: Full Simulation of Space-Based Extensive Air Showers Detectors. *Astropart.Phys.*, 33:221–247, 2010.

[86] Hoai, D. T., Diep, P. N., Darriulat, P., Anh, P. T., Dong, P. N. et al. Simulation of proton-induced and iron-induced extensive air showers at extreme energies. *Astropart.Phys.*, 36:137–145, 2012.

[87] Fenu, F. A simulation study of the JEMEUSO mission for the detection of ultrahigh energy Cosmic Rays. *PhD. Thesis*, 2013.

[88] The JEM-EUSO Collaboration (corresponding authors: Biktemerova, S., Guzmán, A., and Mernik, T.,). Performances of JEM-EUSO: angular reconstruction - The JEM-EUSO Collaboration. *Experimental Astronomy*, February 2014.

[89] Tucker, W. *Radiation processes in astrophysics*. Cambridge, Mass., MIT Press, 1975. 320 p., 1975.

[90] Collins, G. W. *The fundamentals of Stellar Astrophysics*. New York, W. H. Freeman and Co., 1989, 512 p., 1989.

[91] Robitaille, P.-M. A Critical Analysis of Universality and Kirchhoff's Law: A Return to Stewart's Law of Thermal Emission. *ArXiv:0805.1625*, May 2008.

[92] Robitaille, P.-M. Kirchhoff's law of thermal emission: 150 Years. *Progr.Phys.*, 4.

[93] Sportisse, B. *Fundamentals in Air Pollution: From Processes to Modelling*. Springer, 2009.

[94] Abu-Zayyad, T., Jui, C.C.H. and Loh, E.C. The effect of clouds on air showers observation from space. *Astropart.Phys.*, 21:163–182, 2004.

[95] University of Reading. Radiation Models. *http://www.met.reading.ac.uk*, 2014.

[96] NASA. Planetary Atmospheres Data Mode. *http://pds-atmospheres.nmsu.edu/education_and_outreach/encyclopedia/rayleigh_phase.htm*, 2014.

[97] Draine, B. T. Scattering by Interstellar Dust Grains. I. Optical and Ultraviolet. *The Astrophysical Journal*, 598:1017–1025, December 2003.

[98] Sáez-Cano, G., Morales de los Ríos, J. A., del Peral, L., Neronov, A.,Wada, S. and Rodríguez Frías, M. D. for the JEM-EUSO Collaboration. Thin and thick cloud top height retrieval algorithm with the Infrared Camera and LIDAR of the JEM-EUSO Space Mission. *Proceedings of the 2nd AtmoHEAD Conference, Padova (Italy) May 19-21, 2014, ArXiv:1501.04769*, January 2015.

[99] The JEM-EUSO Collaboration (corresponding authors: Guzmán, A., Sáez-Cano, G. and Shinozaki, K.). The JEM-EUSO observation in cloudy conditions. *Experimental Astronomy*, pages 1–18, 2014.

[100] Keilhauer, B., Bohacova, M., Fraga, M., Matthews, J., Sakaki, N., Tameda, Y., Tsunesada, Y. and Ulrich, A. . Nitrogen fluorescence in air for observing extensive air showers. volume 53 of *European Physical Journal Web of Conferences*, page 1010, June 2013.

[101] Morales de los Ríos, J.A., del Peral, L., Sáez-Cano, G., Prieto, H., H-Carretero, J., Sabau, M.D., Belenguer, T., González Alvarado, C., Sanz Palomino, M. Licandro, J., Joven, E., Reyes, M. and Rodríguez-Frías, M.D. for the JEM-EUSO Collaboration. An End to End Simulation code for the IR-Camera of the JEM-EUSO Space Observatory. *arXiv:1204.5065*, July 2013.

[102] Rybicki, G. and Lightman, A. *Radiative processes in astrophysics*. John Wiley and Sons, Inc., 382 p., 1979.